



HAL
open science

Rubidium vapors in high magnetic fields

Stefano Scotto

► **To cite this version:**

Stefano Scotto. Rubidium vapors in high magnetic fields. Atomic Physics [physics.atom-ph]. Université de Toulouse (Paul Sabatier); Università degli studi di Pisa, 2016. English. NNT: . tel-01482289v1

HAL Id: tel-01482289

<https://hal.science/tel-01482289v1>

Submitted on 3 Mar 2017 (v1), last revised 13 Nov 2017 (v2)

HAL is a multi-disciplinary open access archive for the deposit and dissemination of scientific research documents, whether they are published or not. The documents may come from teaching and research institutions in France or abroad, or from public or private research centers.

L'archive ouverte pluridisciplinaire **HAL**, est destinée au dépôt et à la diffusion de documents scientifiques de niveau recherche, publiés ou non, émanant des établissements d'enseignement et de recherche français ou étrangers, des laboratoires publics ou privés.



THÈSE

En vue de l'obtention du

DOCTORAT DE L'UNIVERSITÉ DE TOULOUSE

Délivré par : *l'Université Toulouse 3 Paul Sabatier (UT3 Paul Sabatier)*
Cotutelle internationale *Università di Pisa*

Présentée et soutenue le *13/12/2016* par :
Stefano SCOTTO

Rubidium vapors in high magnetic fields

JURY

DAVID GUÉRY-ODELIN
TICIJANA BAN
WOJCIECH GAWLIK
NICOLÓ BEVERINI
CLAUDE LEROY
FILIPPO LEVI
DONATELLA CIAMPINI
CARLO RIZZO

Président
Rapporteur
Rapporteur
Examinateur
Examinateur
Examinateur
Directeur de thèse
Directeur de thèse

École doctorale et spécialité :

SDM : Physique - COR 02

Unité de Recherche :

Laboratoire National des Champs Magnétiques Intenses (UPR 3228)

Directeur(s) de Thèse :

Carlo RIZZO et Donatella CIAMPINI

Rapporteurs :

Ticijana BAN et Wojciech GAWLIK

Acknowledgments

This work has been realised at the Laboratoire National des Champs Magnétiques Intenses de Toulouse (UPR 3228), in the framework of a joint PhD program between Université de Toulouse and Università di Pisa, with financial support of the Université Franco-Italienne. I want to express my gratitude to the director of LNCMI Geert Rikken and to the vice-director Oliver Portugall for giving me the opportunity to work in this laboratory.

I am grateful to the members of the committee, especially to the referees Prof. Wojciech Gawlik and Prof. Ticijana Ban, for having accepted to evaluate my thesis.

I want to thank my supervisors, Carlo Rizzo and Donatella Ciampini, for their support during the last three years; I also thank Prof. Ennio Arimondo for giving me the opportunity to work on his research project, in the framework of the *Chaire d'excellence Pierre de Fermat*.

I sincerely want to thank the technical staff of LNCMI for their support in the preparation of the experiments; in particular, I am very grateful to Nicolas and Sylvie for their precious collaboration during the preparation of high field experiments.

I am grateful to my family for supporting me in my choices.

Finally, I thank my young colleagues and friends, PhD students and post-docs, from France and from Italy, for the good time we had during the last years, making more enjoyable also the hardest periods of the thesis.



UNIVERSITÉ | UNIVERSITÀ
FRANCO ITALO
ITALIENNE | FRANCESE



UNIVERSITÀ DI PISA

Contents

1	Magnetic field metrology	5
1.1	Magnetic fields	6
1.2	Magnetic field measurements	7
1.2.1	Magnetic resonance techniques	8
	Principle	9
	Field measurement technique	10
	Performances	10
1.2.2	Induction fluxmeter	11
	Principle	11
	Performances	12
1.2.3	Hall effect probes	13
	Principle	13
	Field measurement	14
	Performances	14
1.2.4	Summary	15
1.3	A rubidium sensor for high magnetic fields	15
1.3.1	Principle	16
1.3.2	Field measurement technique	16
1.4	Plan of the thesis	17
2	Magnetic effects in alkali atom spectra	19
2.1	Level structure of rubidium	20
2.1.1	Kinetic and Coulombian term	21
2.1.2	Spin-orbit interaction	22
2.1.3	Hyperfine structure	23

2.2	Interaction between a magnetic field and an atomic manifold	25
2.2.1	The interaction Hamiltonian	27
2.3	Zeeman and Paschen-Back effects	29
2.3.1	Low field solution	30
2.3.2	High field solution	31
2.4	Complete solution	32
2.4.1	Energy levels	33
2.4.2	Optical dipole selection rules	36
2.4.3	Transition strengths	37
2.5	Higher order corrections	40
2.5.1	Diamagnetic shift	40
2.6	Conclusions	41
3	Experimental techniques: Laser spectroscopy tools	43
3.1	The spectroscopical investigation	44
3.2	Linear absorption in atomic vapors	45
3.3	Saturated absorption in two-level systems	48
3.3.1	Principle of saturated absorption spectroscopy	48
3.3.2	Frequency modulation spectroscopy	50
3.4	Multilevel effects in saturated absorption spectra	53
3.4.1	Two-level open system	53
3.4.2	V-type cross-over resonances	58
3.4.3	N and double-N crossover resonances	59
3.5	Conclusions	61
4	Experimental techniques: Magnetic field production	63
4.1	General remarks	64
4.2	Halbach cylinder	65
4.2.1	Properties of permanent magnets	67
4.2.2	Computational modeling	69
4.3	Pulsed magnetic fields at LNCMI-T	72
4.3.1	The LNCMI-T high-field facility	72
4.3.2	Pulsed magnets at LNCMI-T	74
4.4	Conclusions	75

5	Rubidium spectra in a static magnetic field	77
5.1	Experimental setup	78
5.1.1	Overview	78
5.1.2	Spectroscopy setup	81
5.1.3	Halbach magnet: realization and performances	84
5.2	Spectra	87
5.3	Magnetic field evaluation	89
5.3.1	Method	89
5.3.2	Error estimation	90
5.4	Line strengths and linewidths	92
5.4.1	Line intensities in open systems	92
5.4.2	Evolution of the transition probability	95
5.4.3	Linewidths	96
5.5	Conclusions	97
6	Pulsed magnetic field metrology with rubidium atoms	99
6.1	Overview of the method	100
6.2	Pulsed magnetic field coil	101
6.3	Probe design and realization	102
6.4	Pick-up coil calibration	107
6.5	Experimental Set-up	108
6.6	Results	110
6.7	Conclusion	115
7	Conclusions and perspectives	117
A	D_2 spectra in static fields	121
B	D_1 spectra in static fields	131
C	Résumé de la thèse en français	141
C.1	Métrieologie pour les champs magnétiques	142
C.2	Spectres des atomes alcalins sous champ magnétique	144
C.3	Techniques expérimentales: spectroscopie laser	146
C.4	Techniques expérimentales: production du champ magnétique	148

C.5 Spectres du rubidium sous champs magnétiques statiques . . .	150
C.6 Métrologie des champs magnétiques pulsés utilisant des atomes de rubidium	152

Chapter 1

Magnetic field metrology

Contents

1.1	Magnetic fields	6
1.2	Magnetic field measurements	7
1.3	A rubidium sensor for high magnetic fields	15
1.4	Plan of the thesis	17

This work has been realized at the *Laboratoire National des Champs Magnétiques Intenses* (LNCMI) in Toulouse, France in the framework of the *Chaire d'excellence Pierre de Fermat* attributed to Prof. Ennio Arimondo by the *Région Midi-Pyrénées*. The experimental activities we carried out, in collaboration with the BEC group of the University of Pisa - Italy, represent a completely new research field for the LNCMI. While technological research in the field of magnet design and fabrication is rapidly progressing, the measurement techniques need to follow these developments. Experiments in high magnetic fields becoming more and more precise, an accurate and precise knowledge of the magnetic field can be crucial. As instance, the project BMV (Magnetic Birefringence of Vacuum) [1] at LNCMI Toulouse is aimed to measure the magneto-optical properties of vacuum using pulsed magnetic fields; in order to test quantum electrodynamics in such kind of experimental studies, the accurate and precise knowledge of the magnetic field is fundamental. As we will discuss in the Conclusion of this manuscript, atomic physics can benefit of high magnetic field: for example bound state quantum electrodynamics could be tested measuring atomic gyromagnetic factors [2, 3] in strong magnetic fields. These fundamental physics applications demand an accurate and precise knowledge of the magnetic field.

The goal of this introductory chapter is to offer an overview of the main available techniques to measure a magnetic field and to introduce the subject of this thesis. In particular the focus will be on the techniques which allow to characterize magnetic fields within the 0.1 to some tens of teslas range, i.e. the techniques which rely on nuclear magnetic resonance, electromagnetic induction and Hall effect. In the second part of the chapter we will introduce the basic ideas behind our project, whose development within the manuscript is described in the final section of this chapter.

1.1 Magnetic fields

Magnetic fields are generated by moving electric charges and by magnetic materials. The unit of magnetic field in International System is the tesla (T), equal to one weber per square meter. The weber is the magnetic flux which, linking a circuit of one turn, would produce in it an electromotive

force of one volt if it were reduced to zero at a uniform rate in one second [4]. One tesla corresponds to the magnetic field which produces a force of 1 newton on an electric charge of 1 coulomb traveling at a speed of 1 meter per second. Nowadays it is still used the older unit of the c.g.s. system, the Gauss (G), $1 \text{ G} = 10^{-4} \text{ T}$. In nature, a wide range of magnetic field strengths is observed, from some picotesla produced by human brain up to some tens of megatesla generated by a neutron star. Typical magnetic field strengths are summarized in Table 1.1.

Table 1.1: Orders of magnitude of the magnetic fields produced by various source.

Magnitude	Typical values	Source
10^{-12}	100 fT - 1 pT	human brain
10^{-9}	100 pT - 10 nT	heliosphere
10^{-6}	$24 \mu\text{T}$	magnetic tape
10^{-5}	$60 \mu\text{T}$	earth's magnetic field
10^{-3}	5 mT	fridge magnets
10^0	1 T	strong rare earth magnet
10^1	45 T	strongest DC laboratory magnet
10^2	50 - 100 T	non-destructive pulsed magnets
10^3	2.8 kT	strongest destructive laboratory magnet
10^6	1 - 100 MT	neutron stars

Different techniques and instruments have been developed to measure such a wide range of magnetic field strengths, each technique being specifically suited for a particular class of magnetic field characteristics. Our attention is focused on the techniques which are suitable to measure rapidly varying magnetic fields in the 0.1-100 T range.

1.2 Magnetic field measurements

Several methods are available for the measurement of the magnetic field [5]. The best technique for a given application has to be selected balancing different requirements. In particular one has to consider the performances of the instrument in term of

- field measurement range
- resolution
- reproducibility and accuracy
- time bandwidth
- measurement volume

Usually, according to the field measurement range, one distinguishes two classes of instruments: magnetometers are employed to measure weak magnetic fields up to about 1 mT while gaussmeters and teslameters are suited for the measurement of stronger magnetic fields. In the first class we find Superconducting QUantum Interference Device (SQUID) and several typologies of optical and atomic devices. Our interest is mainly focused on the high field instruments so we are not going to discuss the characteristics of low-field instruments; a detailed treatment of these topics can be found in [6]. The second class of instruments (gaussmeter and teslameter) includes nuclear magnetic resonance (NMR) probes, Hall effect devices and induction fluxmeters. An overview of the available technique to measure magnetic fields is given in Figure 1.1, where the measurement ranges and the accuracies are reported. We are particularly interested to the high field region, from about 0.1 T to some tenths of teslas. In the following paragraphs we will present the main techniques which are commonly used to measure magnetic fields larger than 0.1 T. The subjects will be treated following a decreasing accuracy order: we will present as first the magnetic resonance technique, then the fluxmeters and finally Hall effect sensors.

1.2.1 Magnetic resonance techniques

The nuclear magnetic resonance technique (NMR) [8] is considered as the primary standard for calibration. It provides today the most reliable standard for measurement of a homogeneous magnetic field, achieving accuracy of 0.1 ppm in controlled conditions. Commercially available NMR instruments provides a measurement range from 0.01 T to 20 T with an accuracy of about 5 ppm [9].

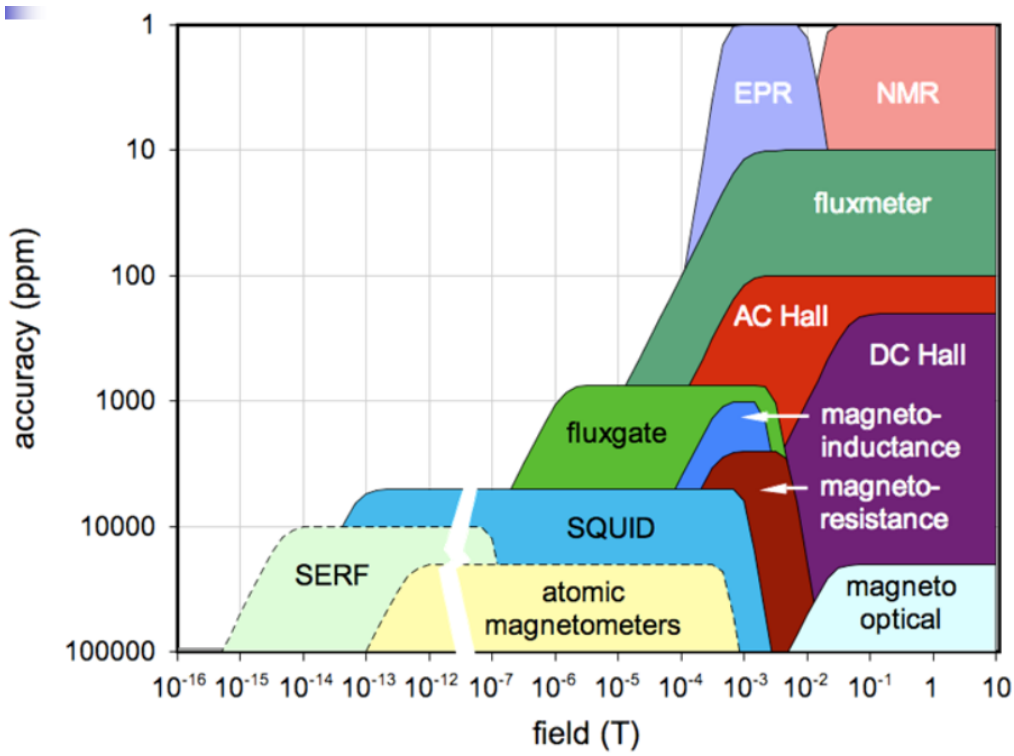


Figure 1.1: Overview of the available techniques to measure magnetic fields and their performances in term of accuracy and measurement range. (From a presentation of Luca Bottura - CERN [7])

Principle

A charged particle which possesses a non-zero angular momentum \mathbf{I} has an associated magnetic moment $\boldsymbol{\mu}$ given by

$$\boldsymbol{\mu} = g \frac{Q}{2Mc} \mathbf{I} = \gamma \mathbf{I} \quad (1.1)$$

where Q and M are the charge and the mass of the considered particle. The Landé factor g and the gyromagnetic ratio γ are the constants which link the angular momentum with the magnetic moment. This last is a property of the particle. If the particle is placed in an external magnetic field \mathbf{B}_0 , the angular momentum vector precesses around the direction of the magnetic field with an orientation such that its component along the field assumes the values equal to $m\hbar/2\pi$. The integral number m can only take values equal

to or between $\pm I$. So there are $2I + 1$ energy levels corresponding to Zeeman splitting of the levels in a magnetic field. The difference between the Larmor frequencies of two adjacent levels is

$$\nu = \frac{\gamma}{2\pi} B \quad (1.2)$$

In the case of the proton $I = 1/2$, so there are only two possible levels whose associated resonance frequencies are separated by $\gamma B/2\pi$. The value of the gyromagnetic ratio is influenced by the chemical environment; the gyromagnetic ratio for proton in water is usually denoted with γ'_p . The measurement of γ'_p for the proton in water has been first performed at 34.7°C by Phillips, Cooke and Kleppner [10] in 1977 at a field of about 0.35 T with respect to the electron magnetic moment. The recommended value of γ'_p given in CODATA2014 [11] is such that $\gamma'_p/2\pi = 42.57638507(53)$ MHz/T (water, sphere, 25°C). This value is taken as a standard reference for nuclear magnetic resonance technique and it guarantees the accuracy of the method.

Field measurement technique

The measurement of the field is based on the detection and measurement of the precession frequency ν of the protons contained in the sample placed inside an excitation coil powered by a radio-frequency oscillator. Usually a sample of water is used. The field value is then evaluated using the relation Eq. 1.2. The measurement of a frequency can be performed with high accuracy, leading to the high accuracy of the method to measure magnetic fields. In practice, there are several experimental techniques to detect the precession signal. Basically, they all rely on integrating the sample in a tuned circuit whose impedance undergoes a change when the resonance condition occurs. We do not enter in further details of the actual realizations of such experimental arrangements, which can be found in specialized literature.

Performances

The range of measurable magnetic fields mainly depends on the practical frequency range of the electronics associated to the instrument. Using com-

mon radio-frequency equipment it is possible to work approximately in the 1-500 MHz range. The minimum and maximum measurable magnetic field is determined by the material which is used for the probe. Choosing electrons as probe (EPR) magnetic fields down to 0.5 mT are measurable, while with a deuterium probe the measure of magnetic fields of about 20 T is affordable [12, 9], because of its larger gyromagnetic ratio. The accuracy of NMR field measurements depends mostly on the method used to detect the Larmor frequency; in general fast measurements are affected by a larger uncertainty. Continuous wave measurements can reach 5 ppm absolute accuracy in a measurement time of 1 s [9]. The measurement time limits the bandwidth of NMR techniques to some tens of hertz, making these instruments unsuitable for application in rapidly varying magnetic fields. In the case of pulsed fields, i.e. fields varying on a timescale shorter than a second, pulsed NMR technique has been developed recently to be used as a probe of matter properties (see [13] and refs therein), but not yet for metrological purposes; in fact pulsed NMR has been performed on solid state samples which do not assure accuracy and reproducibility.

The typical volume of a NMR probe is of the order of 10 to 100 mm³. The size is a compromise between the signal-to-noise requirements and the necessity to have a homogeneous field within the probe. The effect of a field gradient through the sample is to broaden and lower the resonance peak. The limit on the field gradient for a typical probe with linear dimensions of a few mm is between 10 and 100 ppm/mm [12, 9].

1.2.2 Induction fluxmeter

Principle

The principle of the fluxmeter is based in the induction law. Considering a coil whose enclosed surface is denoted as S , the linked flux ϕ is given by

$$\phi = \int_S \mathbf{B} d\mathbf{S} \quad (1.3)$$

where \mathbf{B} is the applied magnetic field and $d\mathbf{S}$ is perpendicular to the surface. A variation in time of the flux linked by the coil induces a voltage proportional

to the rate of change:

$$V = -\frac{d\phi}{dt} \quad (1.4)$$

The detection of this voltage allows the measure of the variation of the enclosed flux, which is then used to deduce the magnetic field. A voltage can be induced either by a variation in time of the magnetic field itself or by a change in the orientation of the coil. In the case of a magnetic field variation in time the coil is usually kept static, and the fluxmeter provides a measurement of the flux change between two given instants. In the case of static fields a movement of the coil is usually employed. In this case the field measurement depends, among others, on the precision of the movement. Several techniques for static and pulsed fields [14] makes the fluxmeter one of the most versatile instruments to measure magnetic fields.

Performances

An induction coil is a linear device, whose sensitivity can be designed to fit the field to be measured. Hence the this method can potentially cover a very broad range of magnetic field strengths. Its main limitation comes from thermal and environmental noise, electronic drifts and the quality of the mechanics in the case of moving or rotating coils. In practice the application of the induction method is limited to minimum field levels above 0.1 μT , with no fundamental limitation at the upper end. The main error source in a fluxmeter is the calibration of the coil sensitivity, which has to be performed in a known magnetic field, using for example an independent NMR measurement. Coil sensitivity to a uniform field, i.e. the effective surface, can be calibrated to typical accuracy ranging from 10 to 100 ppm, depending on the size and shape of the coil. The other source of error comes from the integration of the induced voltage to deduce the magnetic field. Analog, digital or numerical integrator can be used to reach a typical accuracy of 100 ppm [12].

1.2.3 Hall effect probes

In 1879, Hall discovered that when a strip of metal, which was carrying an electric current, was placed in a magnetic field, a voltage was generated across the strip. Hall effect sensors provide a cheap and compact method to measure magnetic fields. This kind of instruments are faster than NMR techniques and easier to operate, at the price of a lower accuracy.

Principle

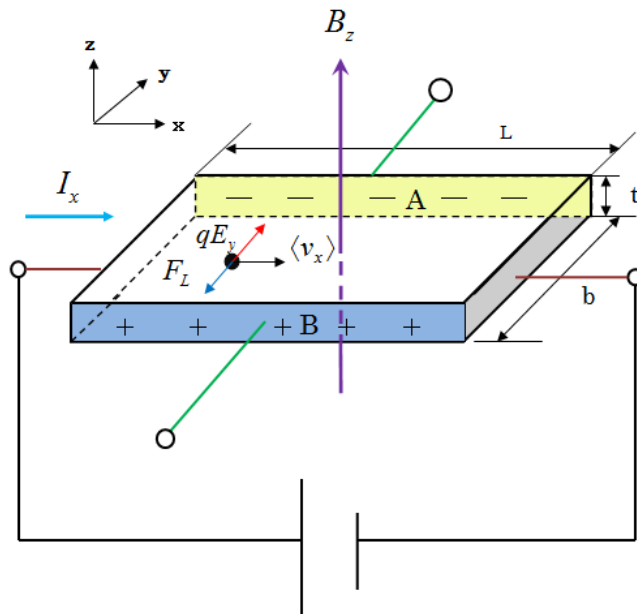


Figure 1.2: Hall effect: a current I_x is flowing through a slab of material in presence of a transverse magnetic field B_z . Carriers are deviated by Lorentz force and the charge accumulation on the edges of the sample build up a Hall voltage V_H .

Hall effect sensors exploit the effects of the magnetic field on motion of free charge carriers in conductors and semiconductors [15]. Considering the thin slab of material represented in Figure 1.2, the component of the magnetic field B_z orthogonal to the face of the slab generates a Lorentz force acting

on the charge carriers moving at velocity v

$$F = qvB_z \quad (1.5)$$

where q is the charge of the carriers. This force tends to curve the path of the charge carriers and causes the polarization of the material in the direction of \mathbf{F} . Consequently an electric field is generated which balances the effect of the Lorentz force. The associated Hall voltage V_H is given by

$$V_H = GR_H I_x B_z \quad (1.6)$$

where the factor R_H is the Hall coefficient characterizing the material, and G is a geometric factor depending on the size and shape of the device and I_x is the control current flowing in the device. The current I_x is usually provided by a stable generator, while the other parameters in Eq. 1.6 have to be measured by a calibration procedure using typically an independent NMR measurement.

Field measurement

The Hall sensor is a four terminal device. The control current is usually supplied by a stable source, while the Hall voltage is measured by a high impedance voltmeter. The voltage measurement is then converted to a magnetic field value using a calibration function. This calibration function needs to be determined by an independent measurement in a known field. Eq. 1.6 displays a linear relation between the Hall voltage and the applied magnetic field. In general there are other effects that make the response of the material deviate from the linear behavior. In particular for precision measurements one has to take in account the fact that the Hall coefficient is temperature dependent.

Performances

The range of magnetic field strengths that can be measured is related to the voltage measurement capability and the sensitivity of the Hall device. The sensitivity depends on the material, the thickness of the device and

the size of the active area. Commercially available Hall sensors have typical sensitivities in the range of 10 mV/T to 1 V/T. Typically, the minimum measurable field for these devices is above 1 mT. Accurate voltage measurement is possible below the μV level using precision voltmeters, thus giving a field resolution better than $0.1 \mu\text{T}$. The absolute accuracy of the measurement is mostly limited by the non-linearity and its temperature dependence and the alignment errors. Commercial equipment has typical accuracy 1000 ppm of reading [16]. The size of the probed volume is determined by the active area of the sensor. Typical volumes are in the range of 0.01 mm^3 to 0.1 mm^3 . Time resolutions for Hall generators are below 1 ns but in general the main measurement bandwidth is limited by the precision voltmeter. Commercial devices have maximum bandwidth extending up to 500 Hz.

1.2.4 Summary

In the previous sections, we presented several methods to measure magnetic field in the tesla range. We outlined the main characteristics of some of them pointing out in particular the accuracy, the bandwidth and the probed volume of these techniques. Nuclear magnetic resonance instruments present the best accuracy, this method relying on the comparison with the γ'_p constant, which is known with great precision, so that the instrument does not need a calibration. All the other techniques are less accurate, due to the necessity of a calibration. At present, none of the presented techniques is perfectly suitable to perform experiments in pulsed high magnetic fields where an accurate knowledge of the magnetic field is a requirement.

1.3 A rubidium sensor for high magnetic fields

Within our project we developed a method to measure magnetic fields with a rubidium vapor, looking for accuracy, high bandwidth and high spatial resolution. This thesis presents the work and shows some atomic physics measurements which we performed or that we will perform using rubidium as a magnetic field sensor. This Section is devoted to the presentation and discussion of the main ideas behind the project.

1.3.1 Principle

The method relies on the correspondence between the magnetic field strength and the resonance frequencies of rubidium. The general principle is similar to that of magnetic resonance: an atomic magnetic moment placed in an external magnetic field interacts with it giving rise to some resonances; the frequency of these resonances depend on the magnetic field strength in a predictable way. In particular, the resonances we consider are in the optical domain, being the resonances corresponding to D transitions of rubidium between the ground and the first excited state of rubidium. The behavior of atomic rubidium in external magnetic field is presented in detail in Chapter 2. Here we want to point out that a single optical measurement gives the value of the field univocally and the conversion between frequency and magnetic field is made via some constants whose value is independent of the external environment.

Rubidium vapor is already used to measure very low magnetic fields because the behavior of the rubidium ground state in a magnetic field is known very accurately. We want to extend the measurement capability of rubidium gas by measuring frequency of transitions between the ground state and first excited states. As in the case of NMR, the transition frequency between well chosen quantum levels depends linearly on the applied magnetic field.

1.3.2 Field measurement technique

We developed an instrument based on laser inducing transitions at about 780 nm (D_2 line) in a rubidium gas contained in a mini-cell of 3 mm x 3 mm cross section. The resonances have to be detected and their frequencies be measured. We used a commercial wavelength meter to measure the frequencies. The design of our sensor follows the pioneering work initiated at NIST, Boulder USA, around 2004 in order to develop miniaturized atomic clocks [17] and that is presented in details in ref. [6]. In a static field we can look for the resonances by scanning the laser frequency while in the case of varying magnetic fields the laser frequency is kept locked and the resonances are scanned by the field variation itself. The detailed description of the techniques is presented in Chapter 6.

1.4 Plan of the thesis

The goal of this work is to develop a system to accurately measure high magnetic fields. The measurement range has to be large, up to some tens of teslas. The system has also to be fast in order to deal with pulsed magnetic fields. The accuracy and reproducibility are guaranteed by the fact that the results of the measurement depend on a physical constant and not on the particular realization of the instrument. All these aspects will be discussed along the thesis.

In Chapter 2 we present the theoretical description of the behavior of rubidium atoms exposed to a magnetic field. This treatment allows the quantitative analysis of the collected spectral data; the comparison between theory and experimental observations is crucial to get a measure of the magnetic field from the spectra. The limits on the indetermination of the measure of the magnetic field imposed by the knowledge of the atomic constants are also discussed.

Chapter 3 is devoted to the presentation of the theoretical background behind the methods of atomic laser spectroscopy. Doppler limited spectroscopy and saturation absorption spectroscopy are discussed. In particular, a detailed description of saturated absorption in multi-level systems is proposed, propaedeutic to the interpretation of the experimental data.

In Chapter 4 we present the sources of magnetic field we used: Halbach cylinders made of permanent magnets provides static fields while peculiar resistive coils produces pulsed high magnetic fields.

In Chapter 5 we propose the experimental data obtained in static magnetic fields using saturated absorption spectroscopy; the strength of the field is obtained comparing the data with the theoretical description of the spectra. The spectral features are analyzed, in particular the structures due to multi-level effects.

Chapter 6 describes the experimental investigations performed in pulsed magnetic field: we present the design and realization of a miniaturized spectroscopy setup in order to satisfy the constraints of high magnetic field experiment. Experimental spectra of rubidium vapors up to about 58 T are included in this chapter.

Chapter 2

Magnetic effects in alkali atom spectra

Contents

2.1	Level structure of rubidium	20
2.2	Interaction between a magnetic field and an atomic manifold	25
2.3	Zeeman and Paschen-Back effects	29
2.4	Complete solution	32
2.5	Higher order corrections	40
2.6	Conclusions	41

This chapter is devoted to the description of the interaction between a simple one-electron-like atom and a static magnetic field. In particular, the case of rubidium will be presented in detail. A precise understanding of the behavior of rubidium atoms in presence of a magnetic field is crucial for the conception of a method to measure magnetic fields using rubidium. In the first part of this chapter, the structure of the energy levels of rubidium is analyzed. The limits of very low and very strong magnetic field will be discussed, showing that a simple perturbative treatment can describe the main feature of the system in these extreme situations. A more general treatment of the problem, involving the diagonalization of the interaction Hamiltonian is necessary to get quantitative insight in a wide range of magnetic field strengths; in particular this approach is fundamental to study the response of rubidium the magnetic field range which is explored in Chapter 5 and to analyze the data presented there. In the final section some higher order corrections to the standard treatment will be discussed.

2.1 Level structure of rubidium

Rubidium is an alkali metal atom with atomic number $Z = 37$. Its electronic configuration in ground state is $[\text{Kr}]5s^1$ and its chemical and spectroscopical properties are mainly determined by the outer electron. Two natural isotopes exist, ^{85}Rb with abundance 78.2% and ^{87}Rb with a natural abundance of about 27.8%. The structure of the energy levels is described by a Hamiltonian operator which includes:

- kinetic energy of the electrons \mathcal{H}_k
- electrostatic interaction between the electrons and the nucleus and electron-electron interaction \mathcal{H}_{es}
- relativistic corrections giving rise to spin-orbit coupling \mathcal{H}_{fs}
- magnetic interaction between the nucleus and the electrons \mathcal{H}_{hfs}

Next subsections present the role of each term of the Hamiltonian in the formation of the spectrum, with a particular attention on the $5S$ ground

state and $5P$ excited state, which are the states we are going to work with in the following of this thesis. The proposed treatment follows the presentation of [18].

2.1.1 Kinetic and Coulombian term

The non-relativistic Hamiltonian for a system of N electrons in the Coulomb potential of a nucleus of charge $+Ze$ is

$$\mathcal{H}_k + \mathcal{H}_{es} = \sum_{i=1}^N \left[-\frac{\hbar^2}{2m} \nabla^2 - \frac{1}{4\pi\epsilon_0} \frac{Ze^2}{r_i} + \sum_{j>1}^N \frac{e^2}{r_{ij}} \right] \quad (2.1)$$

The first two terms are the kinetic energy and potential energy for each electron in the Coulomb field of a nucleus of charge Z . The term with $r_{ij} = |\mathbf{r}_i - \mathbf{r}_j|$ in the denominator is the electrostatic repulsion between the two electrons at \mathbf{r}_i and \mathbf{r}_j . This electrostatic repulsion is too large to be treated as a perturbation; indeed, at large distances the repulsion cancels out most of the attraction to the nucleus. In the usual treatment one assumes that a large part of the mutual repulsion between the electrons can be treated as a central potential $S(r)$. In this central-field approximation the Hamiltonian 2.1 becomes

$$\mathcal{H}_{CF} = \sum_{i=1}^N \left[-\frac{\hbar^2}{2m} \nabla^2 + V_{CF}(r_i) \right] = \sum_{i=1}^N \left[-\frac{\hbar^2}{2m} \nabla^2 - \frac{1}{4\pi\epsilon_0} \frac{Ze^2}{r_i} + S(r_i) \right] \quad (2.2)$$

In this form the Schroedinger equation can be separated in N one-electron equations. In addition, the Schroedinger equations for each electron can be separated in a radial and an angular part. Angular momentum is conserved in a central field and the angular equation gives the standard orbital angular momentum wavefunctions, as in hydrogen. The central potential V_{CF} can be determined in a self-consistent way using the computed wavefunction to calculate the charge density like in the classic Hartee-Fock method [19, 20]. In the rest of this thesis we will be interested only in transitions involving the excitation of the outer electron from the $5s$ orbital to the $5p$ orbital.

2.1.2 Spin-orbit interaction

Relativistic treatment of the atomic system using Dirac equation gives rise to a coupling between the spin \mathbf{s} of the electron and its orbital angular momentum \mathbf{l} . The spin-orbit Hamiltonian takes the form

$$\mathcal{H}_{\text{fs}} = \beta \mathbf{s} \cdot \mathbf{l} \quad (2.3)$$

From commutation relation one gets that a good set of quantum number to describe a system with spin-orbit coupling is $|l, s, j, m_j\rangle$

$$[\mathbf{s} \cdot \mathbf{l}, \mathbf{s}^2] = [\mathbf{s} \cdot \mathbf{l}, \mathbf{l}^2] = [\mathbf{s} \cdot \mathbf{l}, \mathbf{j}^2] = [\mathbf{s} \cdot \mathbf{l}, j_z] = 0 \quad (2.4)$$

The interaction 2.3 gives rise to the fine structure of the atomic spectrum. Levels with the same values of l and s but different j are split by

$$\begin{aligned} \Delta E_{\text{fs}} &= \beta \langle l, s, j, m_j | \mathbf{s} \cdot \mathbf{l} | l, s, j, m_j \rangle \\ &= \frac{\beta}{2} \langle l, s, j, m_j | \mathbf{j}^2 - \mathbf{l}^2 - \mathbf{s}^2 | l, s, j, m_j \rangle \\ &= \frac{\beta}{2} [j(j+1) - l(l+1) - s(s+1)] \end{aligned} \quad (2.5)$$

The ground state of rubidium, in spectroscopic notation, is $5^2S_{1/2}$. The first excited state, which is obtained by promoting the outer electron to the $5p$ orbital, has an orbital angular momentum $L = 1$. The spin-orbit coupling between the orbital angular momentum $L = 1$ and the spin $S = 1/2$ gives rise to the fine structure of the $5P$ manifold. For the ground state the only possible eigenvalue is $J = 1/2$ so there is no fine structure. For the excited state, with $L = 1$, there are two possible values of J i.e. $J = 1/2$ and $J = 3/2$. The transition linking the ground state $L = 0$ to the first excited state $L = 1$ is split into two components, the D_1 line ($5^2S_{1/2} \rightarrow 5^2P_{1/2}$) at about 795 nm and the D_2 line ($5^2S_{1/2} \rightarrow 5^2P_{3/2}$) at about 780 nm. The difference in wavelength usually allows to treat the two fine components separately, but in a very strong external magnetic field (~ 100 T) a comprehensive treatment is needed. In the rest of this Chapter the D_1 and D_2 transitions will generally be treated independently.

2.1.3 Hyperfine structure

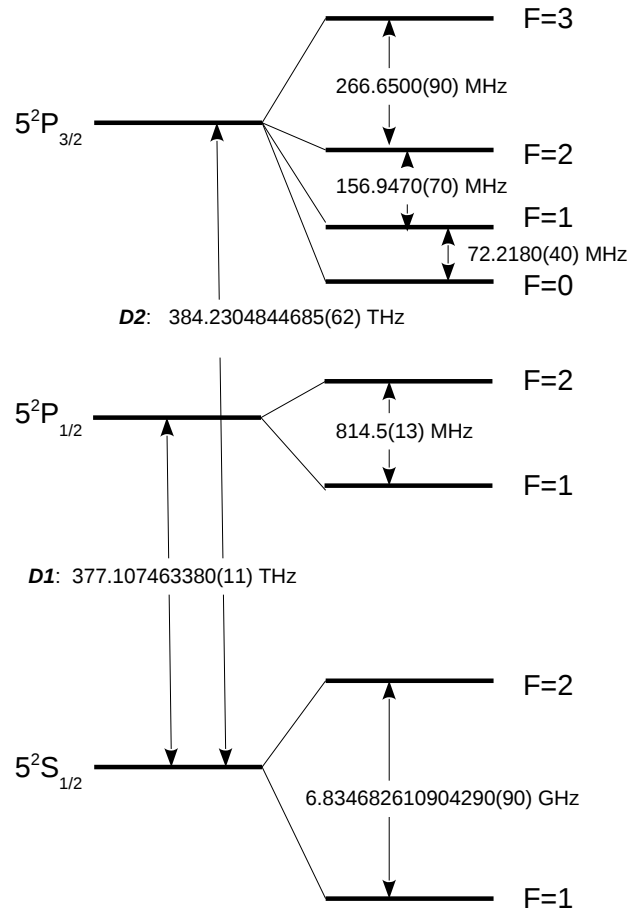


Figure 2.1: Level structure of D lines of ^{87}Rb . On the right fine structure levels $5^2S_{1/2}$, $5^2P_{1/2}$ and $5^2P_{3/2}$. On the right the hyperfine states classified according to their total angular momentum F .

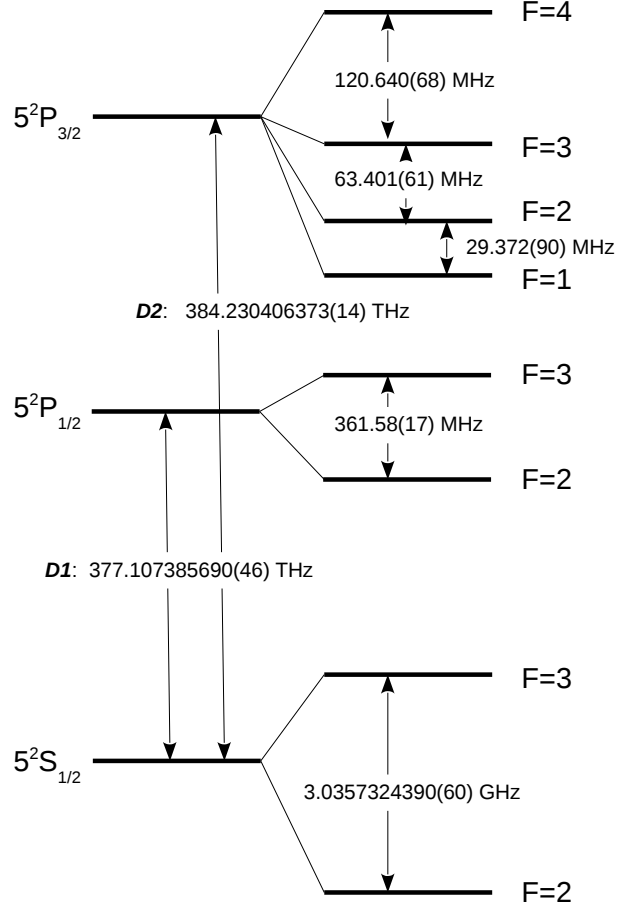


Figure 2.2: Level structure of D lines of ^{85}Rb . On the right fine structure levels $5^2S_{1/2}$, $5^2P_{1/2}$ and $5^2P_{3/2}$. On the right the hyperfine states classified according to their total angular momentum F .

Within each fine structure component, the magnetic and quadrupolar interactions between the electron and the nucleus give rise to the hyperfine structure of the spectrum. The Hamiltonian describing this interaction for each of the D -line components is written as

$$\mathcal{H}_{\text{hfs}} = A_{\text{hfs}} \mathbf{I} \cdot \mathbf{J} + B_{\text{hfs}} \frac{3(\mathbf{I} \cdot \mathbf{J})^2 + \frac{3}{2} \mathbf{I} \cdot \mathbf{J} - I(I+1)J(J+1)}{2I(2I-1)J(2J-1)} \quad (2.6)$$

Like in the case of spin-orbit coupling, a new angular momentum basis is useful to characterize the autostates of the hyperfine interaction of Eq. 2.6.

A set of good quantum numbers is $|L, S, J, F, m_F\rangle$, so the hyperfine levels within a fine-structure component are labeled by the total atomic angular momentum \mathbf{F} given by

$$\mathbf{F} = \mathbf{J} + \mathbf{I}$$

For the ground state of ^{85}Rb , $J = 1/2$ and $I = 5/2$, so $F = 2$ or $F = 3$. For the $5^2P_{3/2}$ state F can assume the value 1,2,3 or 4. In ^{85}Rb the nuclear angular momentum is $I = 3/2$ so the ground state is described by two hyperfine state $F = 1$ and $F = 2$, while for the $5^2P_{3/2}$ state F can take any of the values 0,1,2 or 3. The hyperfine energy shift is given by

$$\Delta E_{hf} = \frac{1}{2}A_{hfs}K + B_{hfs}\frac{3/2K(K+1) - 2I(I+1)J(J+1)}{2I(2I-1)2J(2J-1)}$$

where

$$K = F(F+1) - I(I+1) - J(J+1)$$

and A_{hfs} is the magnetic dipole constant and B_{hfs} is the electric quadrupole constant. All these constants have been measured with high precision. Table 2.1 lists the available experimental values of the magnetic dipole and electric quadrupole constants for the ground $5S$ and the $5P$ excited states. We will need these experimental values to perform calculations about the atomic response to magnetic fields. Figure 2.1 and 2.2 offer a global scheme of the level structure of the two isotopes of rubidium, including fine and hyperfine structure, restricted to the ground state and the $5P$ excited state, which are the states we are interested to.

2.2 Interaction between a magnetic field and an atomic manifold

When a magnetic field is applied to a material, the characteristics of the interaction between the material and the light are modified. These subjects have been extensively studied since the second half of the XIX century, when the electromagnetic theory was established and the understanding of the structural properties of the matter was at the beginning. The earliest stud-

Table 2.1: Hyperfine constants of rubidium.

$A_{5S_{1/2}}^{87\text{Rb}}$	$h \times 3.41734130545315(15)$ GHz [21]
$A_{5P_{1/2}}^{87\text{Rb}}$	$h \times 408.328(15)$ MHz [22]
$A_{5P_{3/2}}^{87\text{Rb}}$	$h \times 84.7185(20)$ MHz [23]
$B_{5P_{3/2}}^{87\text{Rb}}$	$h \times 12.4965(37)$ MHz [23]
$A_{5S_{1/2}}^{85\text{Rb}}$	$h \times 1.0119108130(20)$ GHz [22]
$A_{5P_{1/2}}^{85\text{Rb}}$	$h \times 120.527(56)$ MHz [24]
$A_{5P_{3/2}}^{85\text{Rb}}$	$h \times 25.0020(99)$ MHz [24]
$B_{5P_{3/2}}^{85\text{Rb}}$	$h \times 25.790(93)$ MHz [24]

ies about the interaction between light and matter in presence of a magnetic field were performed by Faraday, with the discovery of the rotation of the polarization of light passing through a medium immersed in a magnetic field [25]. After this first discovery he tried to observe if there was any change in the light emitted from a substance when exposed to a magnetic field. He did not succeed to detect the phenomenon so, some years later (in 1896), the dutch physicist Pieter Zeeman decided to repeat the experiment using a new powerful spectroscopic tool, the diffraction grating. He observed that, when the magnetic field was switched on, the sodium emission lines were broadened [26]. Hendrik Antoon Lorentz developed a model, based on harmonic oscillations of bound charged particles, and he pointed out that, according to his model, the detected broadening is the result of not resolved splittings of the emission lines, grouped in doublets and triplets. The theory developed by Lorentz predicted also that the edges of the non-resolved absorption lines should be circularly polarized, as actually observed by Zeeman. The splitting in doublets and triplets was then detected the following year in cadmium [27]. Magneto-optical experiments by Zeeman together with the Lorentz's model were the first indications of the existence of a new charged particle, later known as the electron. The theory of Lorentz worked well in some cases but failed to explain some details of the observed spectral features (anomalous Zeeman effect) [28]. Some decades later, the phenomenon was brilliantly explained by quantum mechanics.

2.2.1 The interaction Hamiltonian

In the framework of quantum theory, an alkali atom in an external magnetic field \mathbf{B} is well described by the Hamiltonian operator

$$\mathcal{H} = \mathcal{H}_k + \mathcal{H}_{es} + \mathcal{H}_{fs} + \mathcal{H}_{hfs} + \boldsymbol{\mu} \cdot \mathbf{B} = \mathcal{H}_0 + \boldsymbol{\mu} \cdot \mathbf{B} \quad (2.7)$$

where an interaction term between the atom and the magnetic field has been added to the zero-field Hamiltonian. This term is expressed as the interaction between the atomic magnetic moment $\boldsymbol{\mu}$ and the external magnetic field \mathbf{B} :

$$\mathcal{H}_{int} = \boldsymbol{\mu} \cdot \mathbf{B} \quad (2.8)$$

As anticipated in Chapter 1, the magnetic moment $\boldsymbol{\mu}$ is linked to the angular momentum of the atomic quantum states through the Landé g-factors; three g-factors are needed, one for each angular momentum type i.e. one for orbital angular momentum \mathbf{L} , one for electronic spin \mathbf{S} and one for the nuclear spin \mathbf{I} . The interaction Hamiltonian takes the explicit form

$$\mathcal{H}_{int} = \mu_B (g_L \mathbf{L} + g_e \mathbf{S} + g_I \mathbf{I}) \cdot \mathbf{B} \quad (2.9)$$

where μ_B is the Bohr magneton. The Hamiltonian Eq.2.9 can be simplified under the hypothesis that the energy shifts caused by the magnetic field are small compared to the fine structure separation. In this case it is useful to restrict the analysis to only one fine structure component which has a fixed value of the total angular momentum \mathbf{J} . In this case it is useful to recast the Hamiltonian (2.9) in a different form introducing the g_J Landé factor. The Hamiltonian in its simplified form is

$$\mathcal{H}_{int}^J = \mu_B (g_J \mathbf{J} + g_I \mathbf{I}) \cdot \mathbf{B} \quad (2.10)$$

where atomic theory gives

$$g_J = g_L \frac{J(J+1) - S(S+1) + L(L+1)}{2J(J+1)} + g_S \frac{J(J+1) + S(S+1) - L(L+1)}{2J(J+1)} \quad (2.11)$$

Table 2.2 resumes the available experimental values of g factors for rubidium; for the ground state there are very precise measures, while for the $5P$ state there is a measure only for the $5^2P_{3/2}$. The value of the electron-orbital g_L factor is approximately 1, but a correction due to the finite nuclear mass M_{nuc} ,

$$g_L = 1 - \frac{m_e}{M_{nuc}} \quad (2.12)$$

The electron spin g-factor g_S is approximately equal to the free electron spin g-factor $|g_e| = 2.00231930436153(53)$ [29]. The difference between g_e and g_S is due to quantum electrodynamics corrections, due to the fact that the electron is in a bound state (see e.g. [3]). Using Eq. (2.11), one obtains for the ground state $g_J^g = g_S$. As reported in [24], g_J^g for ^{87}Rb has been first measured in 1972 by Tiedeman and Robinson with respect to the free electron value g_e . Authors reported in 1977 [30] a value of the ratio between the g-factor of the ground state of rubidium and the free electron g-factor measured at 5 mT equal to

$$r_{\text{Rb}} = g_J^g/g_e = 1.000005876(13) \quad (2.13)$$

Since isotopic effects on rubidium g-factor has been found to be less than 1 ppb [24], this ratio also apply to ^{85}Rb within the errors. One finally gets for the Landé factor of the ground state of rubidium

$$g_J^g = r_{\text{Rb}}g_e = 2.002331070(26) \quad (2.14)$$

This number differs from the one given in [24], because we used a more recent value of g_e and we used the measured value of the ratio r_{Rb} reported in [30], a reference that was not available to the authors of [24]. For the first excited states, $5^2P_{1/2}$ and $5^2P_{3/2}$, there are less data in literature. No experimental

value exists for $g_J(5^2P_{1/2})$, as far as we know, so we reported in Table 2.2 the value calculated using Eq. (2.11). For the Landé factor of the $J = 3/2$ state, the experimental value reported in [24] is $g_J(5^2P_{1/2}) = 1.3362(13)$ (this is also the value reported in the well-known web review by D. A. Steck [31]); the value reported in Table 2.2 differs from that one. The value reported in [24] comes from the level crossing measurements reported in [32]. In fact the value of the Landé factor can be inferred from the values of the magnetic field at which two energy levels cross; the result also depends on the hyperfine separations at $B = 0$. We considered the level crossing data of [32] and we combined them with a more recent measurement of the hyperfine structure of $5^2P_{3/2}$ reported in [23]. These measurements were not available to the authors of [32] and [24]. The result is the value we quoted in Table 2.2, which is in agreement with the prediction of standard Russell-Saunders treatment expressed by Eq. (2.11). A correction of the order of $10^{-5} - 10^{-6}$ on this value is expected due to bound-state quantum electrodynamics [3]. Table 2.2 collects values of the Landé constants, for ground and excited states, we use in the following for numerical computation of the spectra and for the comparison between experimental observation and theory.

The following sections will assume the simplified Hamiltonian (2.10); the more general expression (2.9) will be used only when explicitly stated. In fact, within the magnetic field range of our investigations, we will assume that the D_1 and D_2 lines can be treated separately. If very high magnetic field ($B \approx 300$ T) were applied, this assumption could be not valid.

2.3 Zeeman and Paschen-Back effects

According to the ratio between the energy shift induced by the magnetic field and the unperturbed energy separations, one can identify different interaction regimes. In the low field regime the magnetic energy splitting is much smaller than the hyperfine separation, so the total angular momentum F and its projections m_F are good quantum numbers to describe the system. This is called *Zeeman* regime. If the energy shift due to magnetic field is larger than the hyperfine separation, the system enters in the *hyperfine Paschen-Back* regime where nuclear and electronic degrees of freedom are decoupled and

Table 2.2: Available data for the Landé g -factors of the ground state and $5P$ states for the two isotopes of rubidium.

g_S	2.00231930436153(53) [29]
$g_L(^{87}\text{Rb})$	0.99999369
$g_L(^{85}\text{Rb})$	0.99999354
$g_I(^{87}\text{Rb})$	-0.0009951414(10) [24]
$g_I(^{85}\text{Rb})$	-0.00029364000(60) [24]
$g_J(5^2S_{1/2})$	2.002331070(26) [29, 30]
$g_J(5^2P_{3/2})$	1.3341(2) [32, 23]
$g_J(5^2P_{1/2})$	0.6659

one needs to label atomic states by using the electronic angular momentum J , its projections m_J and the projections of nuclear spin m_I . Increasing the magnetic field strength leads to the *fine Paschen-Back* effect, where magnetic energy shift is larger than the fine structure separation.

2.3.1 Low field solution

A simple approximate expression of the energy eigenvalues can be found in the case that the shift due to magnetic field is small compared to the hyperfine splitting i.e. when the condition $\mu_B B \ll A_{hfs}$ is fulfilled. The interaction Hamiltonian can be expressed by

$$\mathcal{H}_p = \mu_B g_F F_z B_z \quad (2.15)$$

where the hyperfine Landé g -factor has been introduced:

$$g_F = g_J \frac{F(F+1) - I(I+1) + J(J+1)}{2F(F+1)} + g_I \frac{F(F+1) + I(I+1) - J(J+1)}{2F(F+1)} \quad (2.16)$$

As shown in Figure 2.3, to lowest order the energy levels experience a linear shift given by

$$\Delta E_{|F, m_F\rangle} = \mu_B g_F m_F B \quad (2.17)$$

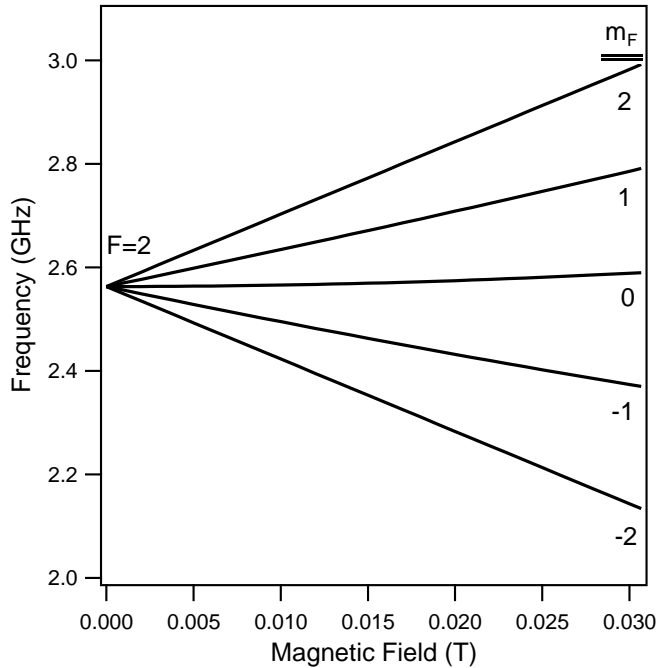


Figure 2.3: Zeeman splitting of $5S_{1/2} F = 2$ level of ^{87}Rb as a function of the magnetic field. Different level of the given F manifold are labeled by the projection of total angular momentum m_F .

2.3.2 High field solution

When the energy splitting caused by the magnetic field is larger than another kind of atomic interaction, the system enters in the so called Paschen-Back regime. Two kinds of Paschen-Back regimes can be identified: the hyperfine Paschen-Back effect is realized when the magnetic interaction is greater than the hyperfine structure separation, $\mu_B B \gg A_{hfs}$, while in the fine Paschen-Back effect the magnetic interaction is larger than the spin-orbit coupling. Under one of these conditions a simple approximated solution can be found. In the first case (*hyperfine Paschen-Back*), one can consider the hyperfine Hamiltonian as a perturbation to the strong-field eigenstates

$|L, S, J, I, m_J, m_I\rangle$. To lowest order one gets

$$E = A_{hfs}m_Jm_I + B_{hfs}\frac{3m_J^2m_I^2 + 3/2m_Jm_I - I(I+1)J(J+1)}{2J(J+1)I(2I+1)} + \mu_B(g_Jm_J + g_I m_I)B_z \quad (2.18)$$

This regime has been recently studied in rubidium by research groups in Durham (UK) [33], Ashtarak (Armenia) and Dijon (France) [34] showing a good agreement between experimental observations, the formula (2.18) and exact diagonalization of the Hamiltonian.

For stronger fields, the system enters in the *fine structure Paschen-Back* regime where the interaction with the magnetic field produces an energy shift larger than the fine structure separation. In these conditions the angular momenta are completely decoupled and energy states need to be labeled by $|L, S, I, m_L, m_S, m_I\rangle$. To first order the effects on energy levels are given by

$$\Delta E = \mu_B B(g_L m_L + g_S m_S + g_I m_I) \quad (2.19)$$

As can be seen in Figure 2.4, to reach this regime with Rubidium very strong magnetic fields are needed, which are hardly available in a physics laboratory; nevertheless lighter alkali atoms have a smaller fine structure separation, making the task easier. Fine Paschen-Back effect has been observed in sodium in a 50 T pulsed magnetic field by Hori *et al.* in 1981 [35].

2.4 Complete solution

To study the behavior of the energy levels in the intermediate regime the full diagonalization of the Hamiltonian is needed. In general a numerical procedure has to be implemented. The solution of the problem in the intermediate regime is crucial for our work; in fact the experimental observations reported in Chapter 5 have been collected in this regime. In addition the complete solution gives correction to the approximate solutions presented in the previous section which are generally not negligible. So we developed a numerical

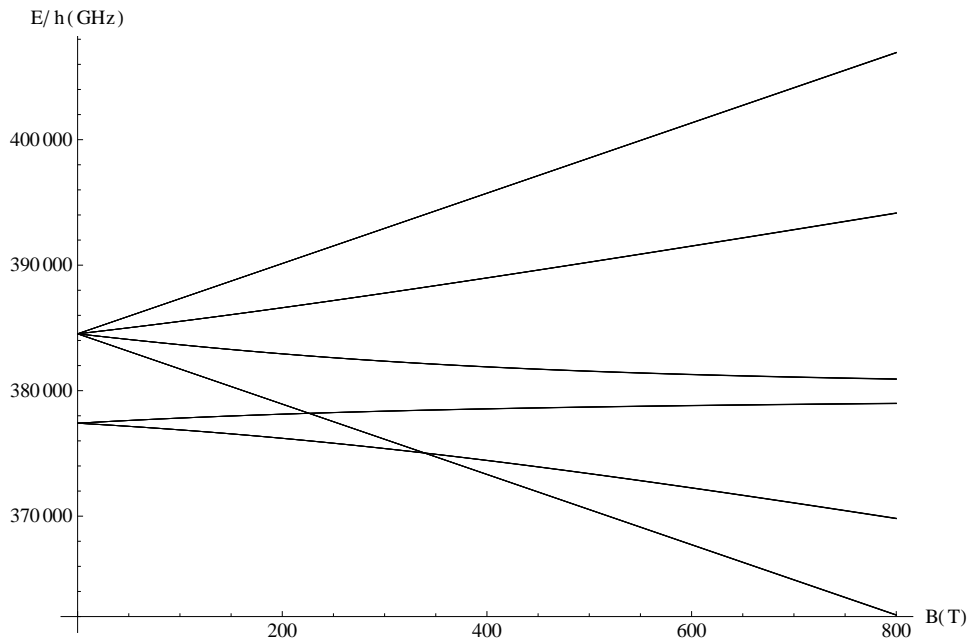


Figure 2.4: Energy level diagram showing the fine Paschen-Back effect for the P state of ^{87}Rb . The behavior for a magnetic field ranging from zero to 800 T has been calculated by our numerical code, which will be described in Section 2.4. The linear behavior at very high magnetic fields is well described by the approximate formula Eq. (2.19).

code to diagonalize the Hamiltonian of a rubidium atom interacting with a magnetic field. From this kind of calculation we get the eigenvalues of the Hamiltonian i.e. the resonance frequency which we observe in the experimental spectra of Chapter 5 and 6. We also obtain the eigenstates which allow us to compute the transition strengths of each resonance and to compare them with the experimental observations, as shown in Chapter 5.

2.4.1 Energy levels

The Hamiltonian is composed by a field-independent part \mathcal{H}_0 which is diagonal in the basis $\{|F, m_F\rangle\}$ and by the magnetic interaction $\mathcal{H}_{\text{int}}(B)$ which is diagonal when expressed in the basis $\{|m_J, m_I\rangle\}$. The resulting energy eigenstates in general will not be simultaneous eigenstates of angular momentum,

so they will be a superposition of angular momentum states:

$$|E\rangle = \sum_{m_J, m_I} a_{m_J, m_I} |m_J, m_I\rangle = \sum_{F, m_F} b_{F, m_F} |F, m_F\rangle$$

In the case of $J = 1/2$, like the ground state of alkali metals or the $P_{1/2}$ excited states, an analytic solution exists, the Breit-Rabi formula

$$E = -\frac{\Delta E_{\text{hfs}}}{2(2I+1)} + g_I \mu_B (m_I \pm m_J) B \pm \frac{\Delta E_{\text{hfs}}}{2} \sqrt{1 + \frac{4(m_I \pm m_J)x}{2I+1} + x^2} \quad (2.20)$$

where ΔE_{hfs} is the hyperfine splitting and

$$x = \frac{(g_J - g_I) \mu_B B}{\Delta E_{\text{hfs}}}$$

This formula is valid for any magnetic field strength. Figure 2.5 show the behavior of the energy level of the ground state of ^{87}Rb as a function of magnetic field; the linear behavior at low and high magnetic fields can be seen, while in the intermediate regime in between the energy levels are curved.

In the general case ($J \neq 1/2$) one has to perform a numerical diagonalization of the Hamiltonian. The calculation will be shown for the state $5^2P_{3/2}$ of ^{87}Rb ; the other cases are treated following, *mutatis mutandis*, the same scheme. First of all, one has to choose two ordered set of angular momentum states to built the basis $\{|F, m_F\rangle\}$ and $\{|m_J, m_I\rangle\}$; for instance a possible choice is

$$\{|F, m_F\rangle\} = \{|3, 3\rangle, |3, 2\rangle, |3, 1\rangle, \dots, |3, -3\rangle, |2, 2\rangle, |2, 1\rangle, \dots, |0, 0\rangle, \} \quad (2.21)$$

and

$$\{|m_J, m_I\rangle\} = \left\{ \left| \frac{3}{2}, \frac{3}{2} \right\rangle, \left| \frac{1}{2}, \frac{3}{2} \right\rangle, \left| -\frac{1}{2}, \frac{3}{2} \right\rangle, \left| -\frac{3}{2}, \frac{3}{2} \right\rangle, \left| \frac{3}{2}, \frac{1}{2} \right\rangle, \left| \frac{1}{2}, \frac{1}{2} \right\rangle, \dots, \left| -\frac{3}{2}, -\frac{3}{2} \right\rangle \right\} \quad (2.22)$$

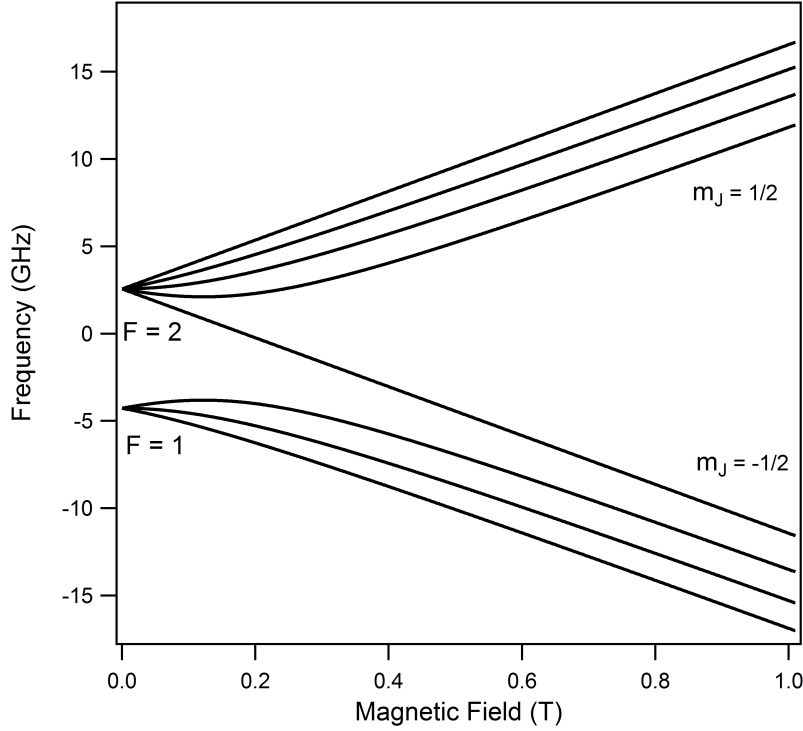


Figure 2.5: Energy level diagram of the ground state of ^{87}Rb as a function of magnetic field strength as calculated from Breit-Rabi formula (Eq. 2.20).

In the basis (2.21), \mathcal{H}_0 is represented by a 16×16 diagonal matrix H_0 whose elements are the zero-field energies of ^{87}Rb ; the magnetic interaction, in the basis (2.22) is represented by a matrix $H_{\text{int}}(B)$ whose diagonal elements are

$$H_{\text{int}}^{qq}(B) = \mu_B B (g_J m_J^q + g_I m_I^q) \quad (2.23)$$

Choosing to express the total Hamiltonian in the basis (2.22), the matrix to be diagonalized is

$$H = U^{-1} H_0 U + H_{\text{int}}(B) \quad (2.24)$$

where U is a unitary matrix made of opportune Clebsch-Gordan coefficients:

$$U^{pq} = C_{J=3/2, m_J^p, I=3/2, m_I^q}^{F^q, m_F^q} \quad (2.25)$$

The numerical codes developed for the diagonalization of the matrix (2.24) give eigenvalues and eigenvectors as a function of magnetic field, so that a

energy levels diagram as a function of magnetic field is traced (Fig. 2.6) and the properties of optical transitions between ground and excited state can be computed.

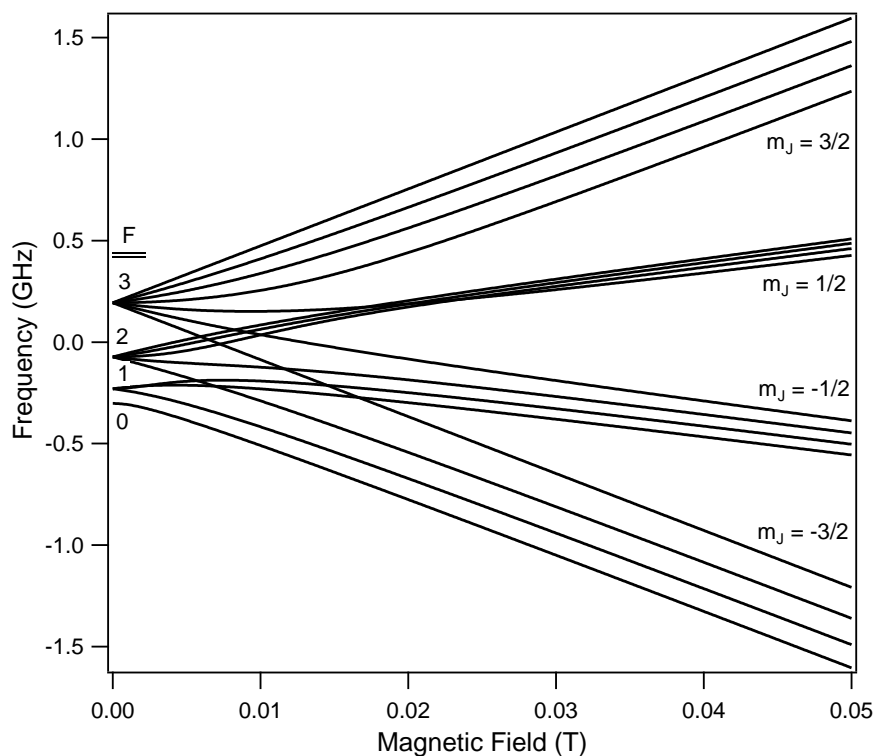


Figure 2.6: Calculated energy level diagram showing the evolution from the Zeeman regime at weak magnetic fields towards the hyperfine Paschen-Back effect at higher magnetic field strengths for the $5^2P_{3/2}$ state of ^{87}Rb

2.4.2 Optical dipole selection rules

To probe the energy level structure of an atom, a monochromatic beam of light can be sent on the specimen to look for resonances in the absorption or emission spectra. In presence of a magnetic field, the spectrum could be crowded, because several transitions generally appear. A set of selection rules determining the allowed and forbidden optical transitions is extremely useful in this situation. In the extreme cases where energy eigenstates are simultaneous eigenstate of angular momentum (Zeeman and Paschen-Back

regimes) a set of selection rules can be stated. In Zeeman regime the pair F, m_F is a good set of quantum number and the relative selection rules are

$$\Delta F = 0, \pm 1$$

$$\Delta m_F = 0, \pm 1$$

$$\Delta F = 0 \Rightarrow \Delta m_F \neq 0$$

In the hyperfine Paschen-Back regime the selection rules are

$$\Delta m_I = 0$$

$$\Delta m_J = 0, \pm 1$$

This set of selection rules will be useful for our investigations at high magnetic fields presented in Chapter 6. In the intermediate regime, which is experimentally explored and presented in Chapter 5, no selection rules can be rigorously used, but typically in this regime a transition is allowed if it is allowed by one set of selection rules, on F or on m_J . A finer treatment is needed in that case, that is the subject of next paragraph. For completeness we also mention the selection rules applying in the very strong field limit (fine Paschen-Back regime), where some conditions on m_S , m_I and m_L have to be considered:

$$\Delta m_S = 0$$

$$\Delta m_I = 0$$

$$\Delta m_L = 0, \pm 1$$

2.4.3 Transition strengths

The decomposition of the energy eigenstates on a basis set of pure angular momentum states is important for the determination of dipole transition strengths between the ground state and the excited states. While in the low-field and high-field regimes the energy eigenstates are, in good approximation, also eigenstate of angular momentum, in the intermediate regime no selection rule can be invoked for a quantitative understanding of allowed and forbidden

transitions. Our numerical code, already described in the part concerning the energy levels, can calculate the transition strengths of the allowed transitions in arbitrary magnetic fields. A direct comparison with our experimental observations is proposed in Chapter 5. Here we describe the procedure to compute the line strengths.

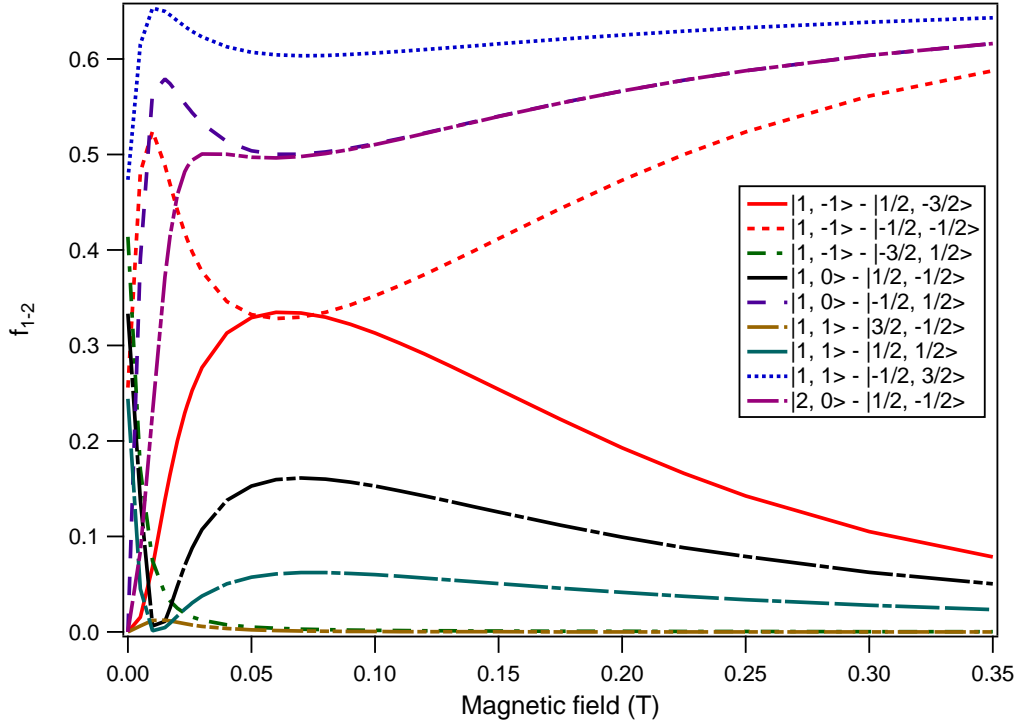


Figure 2.7: Computed relative line strengths as a function of the magnetic field for some ^{87}Rb transition. In legend the involved transitions are identified: the notation $|F, m_F\rangle$ is used for the ground state while the notation $|m_J, m_I\rangle$ is used to identify the excited states. For our work we are interested to magnetic field strengths larger than 0.05 T.

Selected an initial state i and a final state f the strength of the transition to compute is

$$\mathcal{D} = |\langle f|d|i\rangle|^2$$

where d is electrical dipole operator. The initial and final state projected in a basis of angular momentum states, as obtained following the procedure

described in the previous paragraph, are expressed by

$$|i\rangle = \sum_{m_J, m_I} a_{m_J, m_I} |J, m_J, m_I\rangle$$

$$|f\rangle = \sum_{m'_J, m'_I} b_{m'_J, m'_I} |J, m'_J, m'_I\rangle$$

So, noting that the electric dipole operator does not act on the nuclear degrees of freedom, the transition strength becomes

$$\mathcal{D} = \left| \sum_{m_J, m_I} \sum_{m'_J, m'_I} a_{m_J, m_I} b_{m'_J, m'_I} \langle J', m'_J | d | J, m_J \rangle \langle m'_I | m_I \rangle \right|^2 \quad (2.26)$$

Then it is useful to introduce the reduced dipole matrix element $\langle J' || d || J \rangle$, whose numerical value is tabulated in literature, and the matrix element in the expression (2.26) can be transformed in

$$\langle J', m'_j | d | J, m_j \rangle = \frac{\langle J' || d || J \rangle}{\sqrt{2J+1}} C_{Jm, 1q}^{J', m'} \quad (2.27)$$

where $C_{Jm, 1q}^{J', m'}$ denotes a Clebsch-Gordan coefficient and q is zero for π polarization while is ± 1 for σ polarization. Thus the expression (2.26) can be recast in the form

$$|\langle f | d | i \rangle|^2 = \frac{|\langle J' || r || J \rangle|^2}{2J+1} \left| \sum_{m_j, m_I} \sum_{m'_j, m'_I} a_{m_j, m_I} b_{m'_j, m'_I} C_{Jm, 1q}^{J', m'} \right|^2 \quad (2.28)$$

$$= \frac{|\langle J' || r || J \rangle|^2}{2J+1} f_{i-f} \quad (2.29)$$

where we introduced the relative line strength f_{i-f} (an alternative definition is proposed in Chapter 3). For computational convenience a rectangular matrix M made of the opportune Clebsch-Gordan coefficients can be built and the strength expressed in a matrix formulation:

$$\mathcal{D} = |I^+ M F|^2$$

where I and F here denote the column vectors containing the coefficients a_{m_J, m_I} and $b_{m'_J, m'_I}$. As shown in Figure 2.7 the relative line strengths can experience huge variations from zero towards high magnetic field values. In particular at low field the selection rules on F and m_F are valid while at high field (Paschen-Back regime) selection rules on m_J and m_I apply. In these extreme situations the spectra appear simple and show a certain regularity. In the intermediate region a lot of transitions are allowed and the spectra show a complex structure, as will be shown in Chapter 5.

2.5 Higher order corrections

2.5.1 Diamagnetic shift

The Hamiltonian we used in the previous Sections was built by simply adding an interaction term to the zero-field Hamiltonian. A different, and a bit more systematic approach, consists in the transformation of the unperturbed Hamiltonian following the procedure known as minimal coupling. Rigorously, in presence of an electromagnetic field, the kinetic energy of the electrons transforms according to

$$\frac{p^2}{2m} \rightarrow \frac{1}{2m} \left(\mathbf{p} - \frac{e}{c} \mathbf{A} \right)^2$$

where \mathbf{A} is the vector potential, e is the electron charge and c is the speed of light. The linear terms give rise to the interaction $\mathbf{L} \cdot \mathbf{B}$ already discussed and a quadratic term, not considered till now, is found

$$\mathcal{H}_q = \frac{e^2}{2mc^2} A^2 = \frac{e^2}{4mc^2} (\mathbf{r} \times \mathbf{B})^2 \quad (2.30)$$

This quadratic contribution is often negligible but it has to be taken in account in the case of strong magnetic fields or highly excited atomic states (Rydberg states). It can be evaluated by perturbation theory, in the picture of hydrogen-like alkali atoms considering the quantum defect δ . This simple

treatment results in the expression [36]

$$\langle l, m_l, m_s | \mathcal{H}_q | l, m_l, m_s \rangle = -\frac{1}{2} \xi(n^*, l) B^2 3 \frac{l(l+1) + m_l^2 - 1}{(2l-1)(2l+3)} \quad (2.31)$$

where

$$\xi(n^*, l) = 3.308 n^{*2} (15n^{*2} - 9l^2 - 9l + 3) \text{ kHz/T}^2$$

and n^* is the principal quantum number n corrected by the quantum defect. The first experiments aimed to observe a diamagnetic frequency shift in the spectra of alkali-metal atoms were performed in 1939 by Jenkins and Segré [36]. They studied absorption of the Rydberg P series in Sodium and Potassium vapor in a field of 2.7 T, showing a good agreement with the expression 2.31. Diamagnetic effects in many alkali-metal atoms have been measured for several low-lying S and D states by means of Doppler-free two-photon spectroscopy [37, 38]. This scheme allows to select some particular transitions in which linear effects of magnetic field cancel out and frequency shifts are only due to the diamagnetic term in the Hamiltonian. Good agreement was found with a hydrogen-like model with inclusion of quantum defects.

2.6 Conclusions

In this chapter the basic phenomenology of the behavior of an alkali metal atom in a static magnetic field has been reviewed. The topics introduced will be useful for the interpretation of experimental observations presented in Chapter 5 and Chapter 6. The numerical code we developed, whose basic features are outlined in section 1.4, will be used all over the thesis for the quantitative analysis of spectral data.

Chapter 3

Experimental techniques: Laser spectroscopy tools

Contents

3.1	The spectroscopical investigation	44
3.2	Linear absorption in atomic vapors	45
3.3	Saturated absorption in two-level systems	48
3.4	Multilevel effects in saturated absorption spectra	53
3.5	Conclusions	61

In this chapter the main techniques of laser spectroscopy used during this thesis work will be presented. The starting point is the presentation is the description of linear absorption and emission of light. The simplicity of this technique is precious for the applications in high magnetic field presented in Chapter 6, but its resolution limits become relevant in the intermediate regime explored in Chapter 5. Sub-Doppler saturated absorption spectroscopy is necessary in this case. After the presentation of saturation spectroscopy in a two-level scheme, we discuss the more realistic case of a multilevel atom. This more advanced topic is crucial for the interpretation of the experimental spectra presented in Chapter 5. Modification of the saturated absorption signal due to the incoherent redistribution of the atomic populations in three- and four-level systems will be discussed in detail.

3.1 The spectroscopical investigation

Since the beginning of interest in the study of matter and its microscopical structure and properties, optical spectroscopy is one of the most precise tools of investigation [39]. A typical spectroscopy experiment consists in general in the analysis of the transmitted or emitted light by a substance after illumination by a source whose properties are known. Two main basic phases can be distinguished: first of all a measurable signal has to be produced and recorded, then the spectral properties of the source must be analyzed. For example varying the frequency of a laser, the absorption of a sample as a function of the frequency can be observed; to get quantitative insights the frequency of the laser needs to be measured. The nature of the information that one can get are both concerning the sample itself, if the surrounding environment is well known and controlled, and concerning its environment, if the knowledge of the interactions of the system with the environment are already well characterized.

The interaction of a coherent light source, like a laser, with an atomic medium, modeled as a set of two-level systems, is described by the optical Bloch equations [40]. Solving them, one finds that the time-scale of the

atomic excitation is set by the Rabi frequency:

$$\Omega_R = \frac{dE}{\hbar} \quad (3.1)$$

with d being the electrical dipole of the transition between the two considered levels and E the electric field of the light beam. It is more suitable, in an experimental context, to express the the Rabi frequency in term of the light intensity, which is easier to measure

$$\frac{I}{I_{\text{sat}}} = \frac{2\Omega_R^2}{\Gamma^2} \quad (3.2)$$

with Γ being the linewidth of the transition. The saturation intensity I_{sat} sets a light intensity scale which is characteristic of the given transition. From optical Bloch equations one gets that the ratio between the laser intensity and the saturation intensity is the parameter which determines the distribution of the populations N_1 of the ground state and N_2 of the excited state in the steady state with respect to the number of atoms N :

$$N_1 - N_2 = \frac{N}{1 + I/I_{\text{sat}}} \quad (3.3)$$

3.2 Linear absorption in atomic vapors

The absorption of a beam of monochromatic radiation of frequency ν , which propagates along the z axis through an atomic vapor, is described by the Beer-Lambert law [41]:

$$I(z) = I_0 \exp[-\alpha(\nu, T)z] \quad (3.4)$$

where $I(z)$ is the beam intensity at the position z inside the medium with an absorption coefficient $\alpha(\nu, T)$ and I_0 is the intensity of light at $z = 0$, at the entrance of the atomic medium. In general the absorption coefficient is a function of the frequency ν , of the temperature T and of the light intensity. If the beam intensity is sufficiently weak, one can assume that the absorption coefficient is independent of light intensity. The fraction of transmitted light

\mathcal{T} , after that the beam has traversed a medium of length L is defined as

$$\mathcal{T} = \frac{I(z=L)}{I_0} = \exp(-\alpha L) \quad (3.5)$$

The absorption coefficient can be expressed via the imaginary part of the electric susceptibility χ as [42]

$$\alpha(\nu, T) = k\Im[\chi(\nu, T)] \quad (3.6)$$

where k is the wavenumber.

If one focus on a single transition $i \rightarrow f$ between two energy levels separated by an energy $\hbar\omega_0$, the detuning of the impinging light at angular frequency ω_L is defined as $\Delta = \omega_L - \omega_0$. For a medium composed of atoms at rest the complex susceptibility is given by

$$\chi(\Delta) = \mathcal{D}_{if}\mathcal{N}\frac{1}{\hbar\epsilon_0}f_{\Gamma}(\Delta) \quad (3.7)$$

where \mathcal{D}_{if} is the transition strength as defined in Eq. 2.26, \mathcal{N} is the number density of atoms in the level i and $f_{\Gamma}(\Delta)$ is a lineshape function derived from the steady state solution of optical Bloch equations [40]

$$f_{\Gamma}(\Delta) = \frac{i}{\Gamma/2} \left[1 - i \left(\frac{\Delta}{\Gamma/2} \right) \right]^{-1} \quad (3.8)$$

The real part of the expression 3.8 has a characteristic dispersion profile while the imaginary part describes a Lorentzian absorption profile as expected for a homogeneously broadened system. The thermal motion of the atoms along the axis of the beam causes the Doppler broadening of the resonance. The thermal velocity v of the atoms is described by the Maxwell-Boltzmann distribution

$$W(v) = \frac{1}{\sqrt{\pi}u} \exp \left[- \left(\frac{v}{u} \right)^2 \right] \quad (3.9)$$

where the $1/e$ width u depends of the temperature T and of the mass of the atoms M according to the relation $u(T) = \sqrt{2k_{\text{B}}T/M}$. To find the absorption profile of a gas of atoms in thermal motion, the convolution between the homogeneous lineshape function $f_{\Gamma}(\Delta)$ and the Gaussian velocity distribu-

tion has to be performed, obtaining the Doppler broadened lineshape:

$$g_D(\Delta) = \int_{-\infty}^{+\infty} f_{\Gamma}(\Delta - kv) \times W(v) dv \quad (3.10)$$

The analytic solution of the convolution integral involves special functions; the imaginary part of the function $g_D(\Delta)$ is the well-known Voigt profile. Combining Eq. 3.6, 3.7 and 3.10 the absorption coefficient for a single atomic transition is expressed by

$$\alpha(\Delta, T) = k\mathcal{D}_{if}\mathcal{N}(T)\frac{1}{\hbar\epsilon_0}\Im[g_D(\Delta)] \quad (3.11)$$

The temperature dependence comes from two contribution: the width of the Doppler profile, which is proportional to the square root of the temperature and the number density of atoms, which is a strong function of temperature [43]. For rubidium, considering the D_1 and D_2 transitions, the Doppler width at room temperature is about $\Delta_D \simeq 500\text{MHz}$. At zero magnetic field, as shown in Figure 3.1 (red curve), the Doppler width prevents to resolve the hyperfine structure of the excited 5P states; in presence of a moderate magnetic field in the sub-tesla range, absorption profiles becomes more and more broadened due to the splitting of magnetic quantum states (see blue and green curves in Figure 3.1). This situation is not suitable to extract precise spectroscopic information, because the underlying structure are hidden in a very large absorption profile in frequency domain. To explore these feature Doppler-free spectroscopy is needed. Nevertheless, in stronger magnetic fields ($B \gtrsim 1\text{ T}$), the frequency separation between two adjacent absorption lines of ^{87}Rb is about 1.5 GHz so that linear Doppler-limited spectroscopy can be exploited to resolve them. In particular, due to the required complexity of the setup in a high magnetic field experiment, the possibility to get spectral information with a simple technique like Doppler-limited spectroscopy is crucial, as will be evident in Chapter 6.

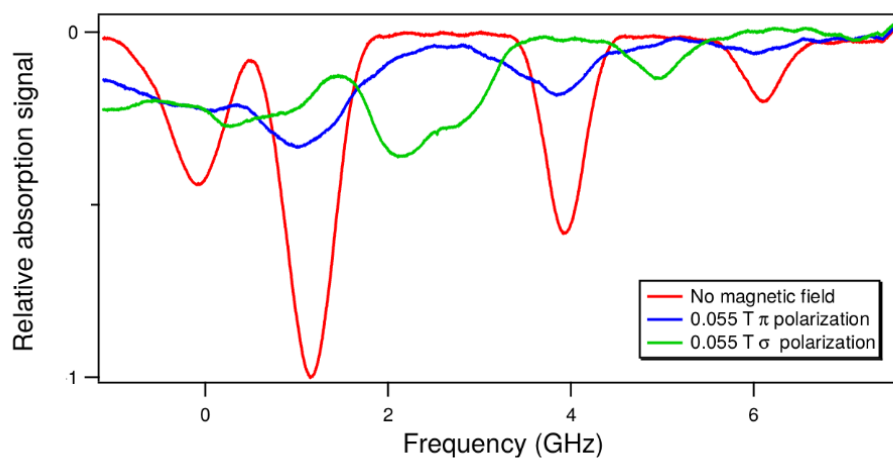


Figure 3.1: Linear Doppler-limited relative absorption of rubidium without magnetic field (red curve) and in presence of a magnetic field of about 0.055 T (blue and green).

3.3 Saturated absorption in two-level systems

Saturated absorption is the most widely employed technique to eliminate the Doppler broadening in spectroscopy of atomic and molecular samples. In a situation where many atomic transitions are close to each other it is fundamental to eliminate the Doppler broadening to resolve all the resonances. In Chapter 5 we will present the results of our investigations about rubidium spectra in magnetic field in the 0.05-0.2 T range; in this magnetic field range rubidium is in an intermediate regime between Zeeman and Paschen-Back regimes (see Chapter 2) where many absorption lines are present, so the use of Doppler-free techniques is useful to get information from the spectra.

3.3.1 Principle of saturated absorption spectroscopy

In saturation spectroscopy, a laser beam is split into two beams which are sent to the atomic sample so that they are counter-propagating (Figure 3.2). The stronger beam (control beam or pump beam) saturates the transition and burns a hole in the Doppler profile while the weaker beam (probe beam) is sent into a detector to measure the absorption signal as a function of

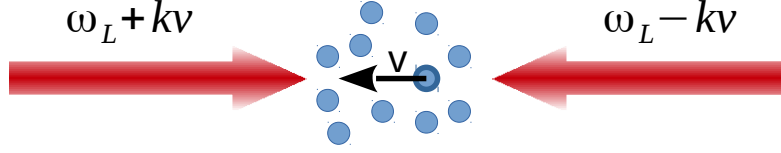


Figure 3.2: Sketch of a saturated absorption experiment: two beams at angular frequency ω_L are counterpropagating; an atom moving at velocity v on the axis of the beams “sees” two different frequencies for the two beams, due to Doppler effect. The atom has a resonance at frequency ω_0 close to ω_L . The atom is resonant with both the beams only if its velocity on the direction of the beams is zero.

frequency [44]. Denoting with ω_L the angular frequency of the laser and ω_0 the frequency of the atomic resonance, the control beam interacts with atoms that have velocity $v = (\omega_L - \omega_0)/k$ and excites many of them in the upper level. The probe beam interacts with atoms that have velocity $v = (\omega_0 - \omega_L)/k$. The two beams only interact with the same velocity class if the velocity is zero along the wavevector \mathbf{k} . In this case the absorption of the probe beam versus laser frequency will show a dip on the broad Doppler background, because there are less available atoms in the lower state. The absorption coefficient for the probe beam is calculated taking in account the modification of the ground state population caused by the control beam; for a closed transition between two atomic levels $i \rightarrow f$ the absorption coefficient of the probe beam is given by [18]

$$\alpha_{\text{sa}}(\Delta) \propto \alpha(\Delta) \times \left[1 - \frac{I}{2I_s} \frac{\Gamma_{\text{pb}}^2/4}{\Delta^2 + \Gamma_{\text{pb}}^2/4} \right] \quad (3.12)$$

where $\alpha(\Delta)$ is the Doppler absorption profile as expressed in Eq. 3.11, I is the intensity of the pump beam, I_s is the saturation intensity and Γ_{pb} is

the homogeneous power broadened linewidth of the considered transition:

$$\Gamma_{\text{pb}} = \frac{\Gamma}{2} \left(1 + \sqrt{1 + \frac{I}{I_{\text{sat}}}} \right) \quad (3.13)$$

with Γ being the natural linewidth of the transition.

Eq. 3.12 shows that the shape of the saturated absorption signal is a narrow Lorentzian function lying on a broader Doppler background (see Figure 3.3). The amplitude of the signal for a closed two level system is directly proportional to the strength of the considered transition S_{if} , this factor being in the Doppler background $\alpha(\Delta)$. As will be shown in Section 3.4, this is not always the case for a more general multilevel system.

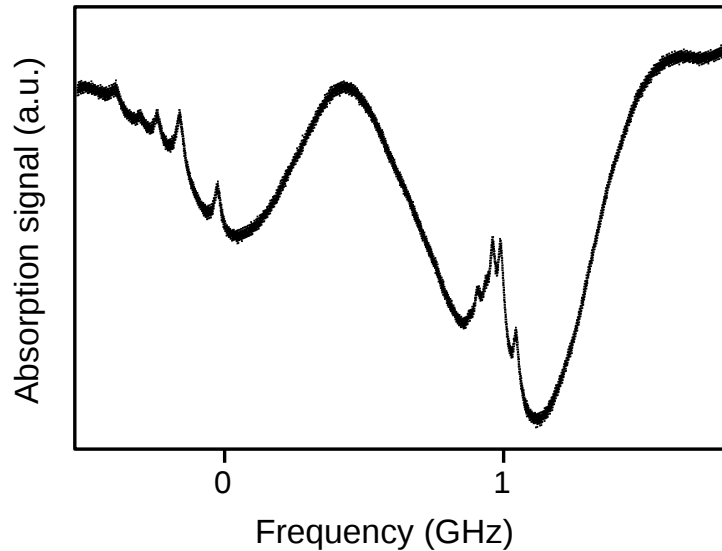


Figure 3.3: Saturated absorption spectra of the $D2$ line of rubidium. Narrow peaks corresponding to the hyperfine transitions $F = 2 \rightarrow F' = 1, 2, 3$ of ^{87}Rb (peaks at left) and $F = 3 \rightarrow F' = 2, 3, 4$ of ^{85}Rb (at right) are visible on a broad Doppler background.

3.3.2 Frequency modulation spectroscopy

Frequency modulation techniques [45] are often employed in order to increase the signal to noise ratio of a saturated absorption spectrum. Typically the

frequency modulation of the laser frequency is implemented with an electro-optical modulator or an acousto-optical modulator and then the signal is recovered using synchronous detection. The electric field of a frequency modulated light beam has the form

$$E = E_0 \sin[\omega_C t + \delta \sin \omega_m t] \quad (3.14)$$

where ω_C is the carrier frequency, close to the atomic resonance frequency ω_0 , ω_m is the modulation frequency and δ is the modulation index, which represents the frequency excursion around the carrier. Eq. 3.14 can be expanded in term of the Bessel functions $J_n(\delta)$:

$$E = E_0 \left[\sum_{n=0}^{\infty} J_n(\delta) \sin(\omega_C + n\omega_m)t + \sum_{n=1}^{\infty} (-1)^n J_n(\delta) \sin(\omega_C - n\omega_m)t \right] \quad (3.15)$$

After passing through the atomic sample the probe beams beats with its sidebands on the detector, generating an electric signal oscillating at the modulation frequency ω_m . Considering only the first sidebands, the signal S is proportional to [46]

$$S \propto J_0(\delta)J_1(\delta) \times [(L_{-1} - L_{-1/2} + L_{1/2} - L_1) \cos(\omega_m t + \phi) + (D_1 - D_{1/2} - D_{-1/2} + D_{-1}) \sin(\omega_m t + \phi)] \quad (3.16)$$

where

$$L_n = \frac{\Gamma^2}{\Gamma^2 + (\Delta - n\omega_m)^2}$$

and

$$D_n = \frac{\Gamma(\Delta - n\omega_m)}{\Gamma^2 + (\Delta - n\omega_m)^2}$$

Using a phase sensitive detection, the term proportional to the sine or the cosine is selected. The obtained signal is an odd function of the detuning between the laser frequency and the resonance frequency; if the modulation frequency and the the modulation index multiplied by the modulation frequency are smaller than the linewidth, the shape of the signal is approximately the derivative of a Lorentzian function (Figure 3.4). We exploited

the dispersive nature of the modulation spectroscopy signal to lock the lasers on the atomic reference.

In practical realizations of modulation spectroscopy, the frequency modulation is impressed on the probe beam using an acousto-optic or an electro-optic modulator. A different approach is to modulate the control beam: the modulation is then transferred to the probe beam via four-wave mixing inside the atomic medium. This latter technique, called modulation transfer spectroscopy [47, 48], has the advantage to eliminate the broad Doppler background, producing a flat signal with dispersion-like features corresponding to Doppler-free resonances whose zero-crossing point corresponds to the center of the resonance. For the investigation of rubidium spectra in intermediate-strength magnetic fields (Chapter 5) we adopted the modulation of the control beam using an acousto-optic modulator with modulation frequency $\omega_m = 50$ kHz and modulation index $\delta \approx 30$.

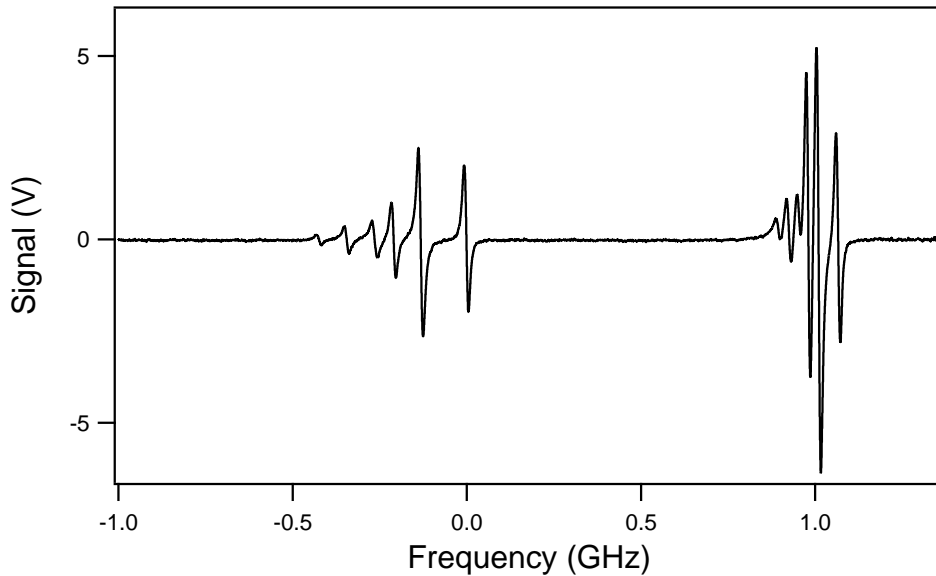


Figure 3.4: Modulation transfer signal of the saturated absorption spectrum of $D2$ line of rubidium. The signal has been obtained with a 50 kHz frequency modulation of the control beam. Dispersive signals on a flat background corresponding to the hyperfine transitions $F = 2 \rightarrow F' = 1, 2, 3$ of ^{87}Rb (peaks at left) and $F = 3 \rightarrow F' = 2, 3, 4$ of ^{85}Rb (at right) are visible.

3.4 Multilevel effects in saturated absorption spectra

In a realistic situation an atom has more than two levels connected by radiative coupling. New resonances, called crossover, appear midway between two two-level resonances in a three- or four-level system. Moreover, optical pumping plays an important role in the formation of saturated absorption signals, altering the magnitude and the sign of saturation resonances [49, 50]. The simplest way to treat an atomic system involving more than two levels is to consider a two-level system where the atoms can decay towards other not specified states. This model can catch some features of the multilevel system, in particular gives predictions for the amplitudes and the linewidths of the transitions, which will be experimentally investigated in Chapter 5. A treatment which considers the detailed dynamics of three- and four-level systems is needed to analyze crossover resonances.

3.4.1 Two-level open system

A two-level open system can be defined as a two-level system where the atoms excited from a lower state to an upper state can decay to a lower state different from the initial lower state. Figure 3.5 shows the relevant quantities to analyze the system. Two atomic levels $|1\rangle$ and $|2\rangle$ are coupled by the control and the probe beam. The atoms excited to the $|2\rangle$ level can decay to the state $|1\rangle$ with a branching ratio Π_{21} or to any other allowed state with a branching ratio $1 - \Pi_{21}$. In order to compare the saturation absorption signals associated with a variety of optical transitions, for each given two-level system $|i\rangle \rightarrow |f\rangle$ a theoretical relative line strength f_{i-f} can be defined as the square of the dipole moment \mathcal{D}_{if} matrix element between the initial and final states, normalized to the optical dipole moment of the closed cycling transition. Thus, as instance, for the D_2 transition of ^{87}Rb the considered quantity is

$$f_{i-f} = \frac{\mathcal{D}_{if}}{|\langle 5^2S_{1/2}, F=2, m_F=2 | d | 5^2P_{3/2}, F'=3, m'_F=3 \rangle|^2}$$

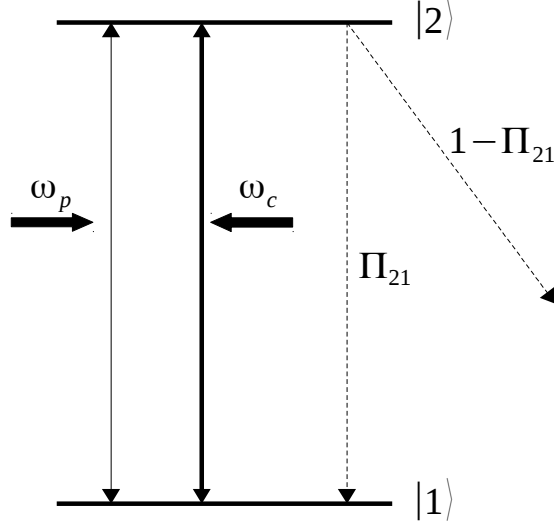


Figure 3.5: Scheme for a two-level open system: atoms are excited by the strong control laser at frequency ω_c and by the weak probe laser at frequency ω_p from the state $|1\rangle$ to the state $|2\rangle$; they can decay again into the state $|1\rangle$ with a branching ratio Π_{21} or towards other lower states with a branching ratio $1 - \Pi_{21}$.

For a quantitative analysis we have solved the rate equations for the atomic populations in presence of the strong control laser beam and then use that solution to calculate the absorption of the probe beam.

For a given atomic velocity v , the atomic population density N_1 and N_2 within the levels $|1\rangle$ and $|2\rangle$ respectively are given by [51]

$$\frac{\partial N_1}{\partial t} = \Gamma_c(N_2 - N_1) + \Gamma\Pi_{21}N_2 - \gamma(N_1 - N_1^0) \quad (3.17)$$

$$\frac{\partial N_2}{\partial t} = -\Gamma_c(N_2 - N_1) - \Gamma N_2 \quad (3.18)$$

with Γ being the excited state spontaneous decay rate, N_1^0 being the population density of level $|1\rangle$ in absence of light given by the Maxwell-Boltzmann distribution

$$N_1^0 = W(v) = \frac{1}{\sqrt{\pi}u} \exp\left[-\left(\frac{kv}{\Delta_D}\right)^2\right] \quad (3.19)$$

$W(v)$ is the Gaussian atomic velocity distribution, with $\Delta_D = ku$ being the Doppler width, $u = (2k_B T/M)^{1/2}$ being the most probable velocity, where T is the temperature, k_B is the Boltzmann constant, and M is the atomic mass, like in Eq. (3.9). The parameter γ is the rate at which atoms are destroyed in the ground state $|1\rangle$. The parameter γ can be considered as an effective lifetime of the ground state atoms mainly due to transit time across the laser beam. Γ_c is the control laser pumping rate, given by

$$\Gamma_c = f_{1-2} \frac{I}{2I_{\text{sat}}} \frac{\Gamma}{1 + 4\Delta_c^2/\Gamma^2} \quad (3.20)$$

where Δ_c is the laser detuning for the driven transition. The steady state solution of Bloch equations for the atomic populations are

$$N_1 = N_1^0 \left[1 - \frac{I_c}{I_c + I_{\text{op}}} \times \frac{1 + \frac{\Gamma(1 - \Pi_{21})}{2\gamma}}{2 + \frac{\Gamma(1 - \Pi_{21})}{2\gamma}} L(\Delta_c - kv) \right] \quad (3.21)$$

$$N_2 = N_2^0 \frac{I_c}{I_c + I_{\text{op}}} \times \frac{1}{2 + \frac{\Gamma(1 - \Pi_{21})}{2\gamma}} L(\Delta_c - kv) \quad (3.22)$$

where $L(x)$ is a power-broadened Lorentzian lineshape function and I_{op} is the optical pumping saturation intensity. The saturation intensity in this open system undergoes an effective reduction with respect to the value of a closed cycling transition due to optical pumping towards other states. The expression of the effective optical pumping saturation intensity is given by [51, 52]

$$I_{\text{op}} = \frac{I_{\text{sat}}}{f_{1-2}} \frac{1 + \frac{\gamma}{\Gamma}}{1 + \frac{\Gamma(1 - \Pi_{21})}{2\gamma}} \quad (3.23)$$

In the case of D lines of alkali atoms, the first excited P states can only decay to the ground S state, so the branching ratio Π_{21} is equal by definition to the adimensional factor f_{1-2} . In this case the effective saturation intensity I_{op} can be rewritten as a function of f_{1-2} ; I_{op} tends toward I_{sat} (corrected by the term $1 + \gamma/\Gamma$ to take in account the finite interaction time with the

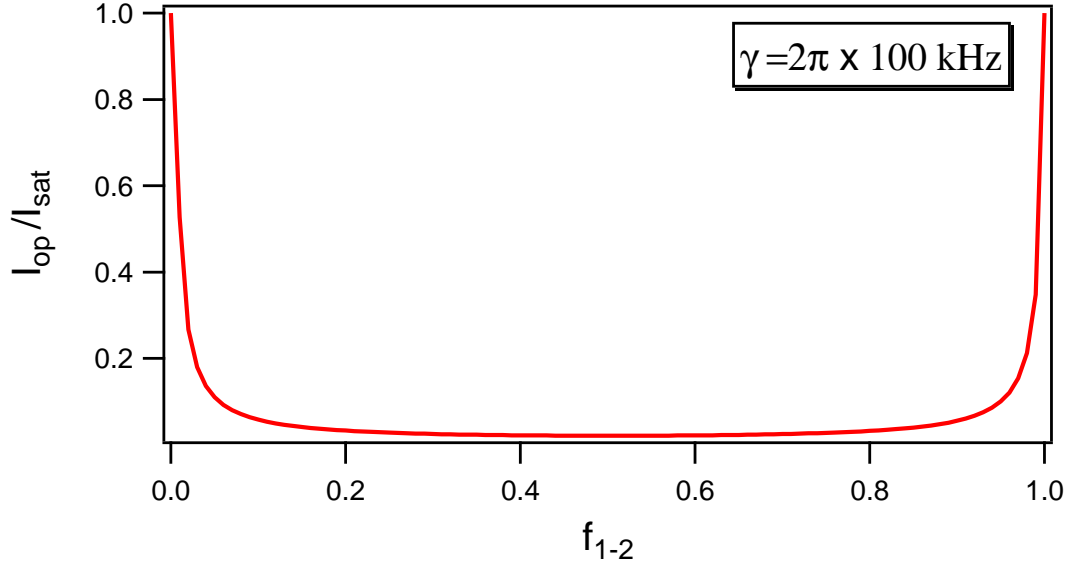


Figure 3.6: Behavior of the effective saturation intensity in presence of optical pumping I_{op} (Equation 3.23) as a function of the relative line strength f_{1-2} with a “ground state lifetime” $\gamma/2\pi = 100$ kHz.

light) for values of f_{1-2} close to one, while it diverges to infinity for values of f_{1-2} close to zero. For the values in between, I_{op} is always lower than I_{sat} (Figure 3.6). In presence of optical pumping driven by the control beam, the expression of the absorption coefficient for the probe beam as a function of its detuning Δ from the atomic resonance is given by:

$$\alpha_{op} \propto \alpha(\Delta) \left(1 - s \frac{\Gamma_{op}^2/4}{\Delta^2 + \Gamma_{op}^2/4} \right) \quad (3.24)$$

where s is the saturation factor describing the depth of the resonance

$$s = \frac{I/I_{op}}{(1 + \sqrt{1 + I/I_{op}})\sqrt{1 + I/I_{op}}} \quad (3.25)$$

and the width of the Lorentzian resonance is

$$\Gamma_{op} = \frac{\Gamma}{2} \left[1 + \sqrt{1 + \frac{I}{I_{op}}} \right] \quad (3.26)$$

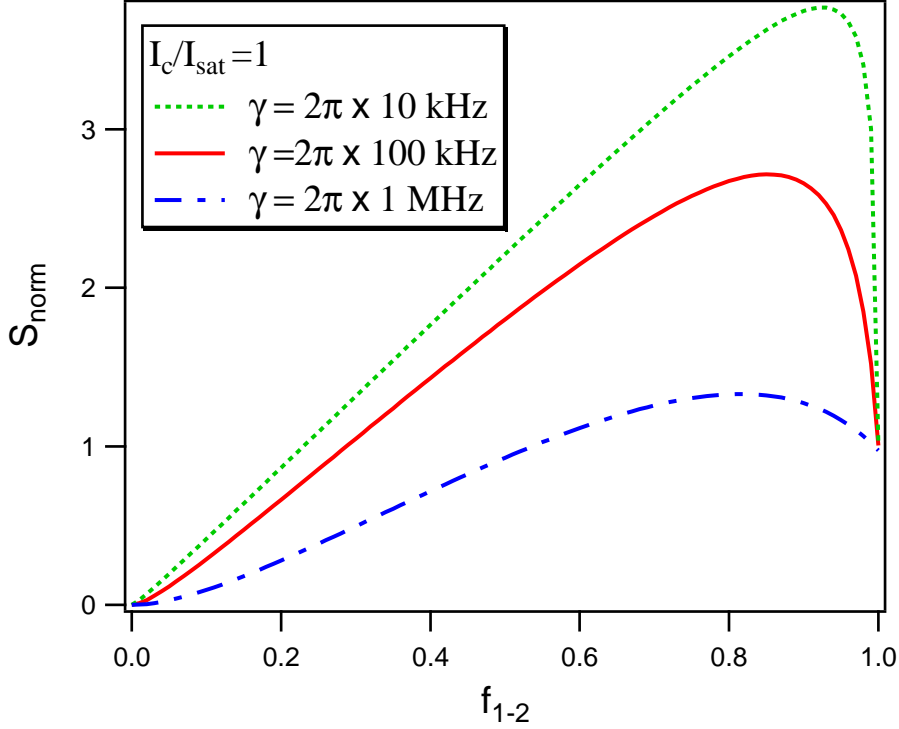


Figure 3.7: Amplitude of the saturated absorption signal in presence of optical pumping as a function of the relative line strength f_{1-2} . The intensity of the control laser is taken equal to the saturation intensity while three different values of γ are considered. The curves are normalized such that the amplitude of the closed cycling transitions ($f_{1-2} = 1$) is one.

The shape of the absorption signal is the same as in the case of a closed two-level system (see Eq. (3.12)), with narrow Lorentzian peaks on a broad Doppler background, but the amplitude and the width of the sub-Doppler resonances are influenced by optical pumping. One of the observable we will analyze in Chapter 5 is the amplitude S of the Lorentzian functions corresponding to the sub-Doppler signals. Using Eq. (3.24) we express the amplitude S as

$$S = \alpha(0)s \quad (3.27)$$

In the experimental investigation proposed in Chapter 5 we do not perform absolute measurements of the amplitude S so it is convenient to normalize S to the amplitude of the closed cycling transition with $f_{1-2} = 1$.

The plot in Figure 3.7 shows the normalized amplitude S_{norm} of the sub-Doppler resonance calculated from Eq. (3.27) (with the discussed normalization) as a function of the relative line strength f_{1-2} . The normalized amplitude S_{norm} displays a maximum for a certain value of f_{1-2} intermediate between zero and one. The presence of a maximum can be understood considering the interplay between the increasing line strength f_{1-2} and the decreasing of the factor I/I_{op} .

3.4.2 V-type cross-over resonances

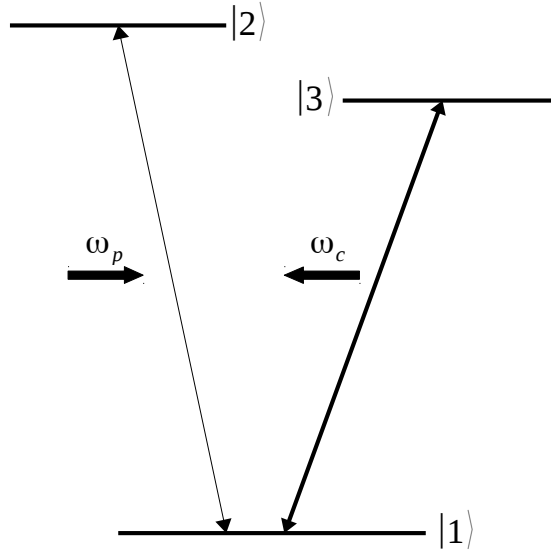


Figure 3.8: Scheme for the sub-Doppler saturation spectroscopy of a V three-level system. Strong control laser at angular frequency ω_c and weak probe laser at angular frequency ω_p traveling in opposite directions excite the atomic levels. Lasers are depicted as resonant.

In a V-three level system the probe laser acts on the $|1\rangle \rightarrow |2\rangle$ transition and the control laser acts on the $|3\rangle \rightarrow |4\rangle$ one. Atoms excited to level $|3\rangle$ decay towards level $|1\rangle$ with a branching ratio Π_{31} and towards other states with a branching ratio $1 - \Pi_{31}$; we neglect the decay of the state $|2\rangle$ towards other levels because this level is weakly populated by the probe beam. When two transitions share a common lower level (Figure 3.8) and their frequencies are separated less than the Doppler width, a new peak located midway

between the two transitions appears [39, 18]. In the situation sketched in Figure 3.8 the control beam burns two holes in the velocity distribution; these holes give rise to two peaks corresponding to the two-level transitions $|1\rangle \rightarrow |2\rangle$ and $|1\rangle \rightarrow |3\rangle$. In addition, another peak appears when the hole burnt by one transition reduces the absorption for the other transition. The amplitude f^{VTL} of the V-type crossover is derived by including an additional upper level to the analysis of Sect. 3.4.1. Extending that analysis to the probe laser acting on the $|1\rangle \rightarrow |2\rangle$ transition and the control laser acting on the $|1\rangle \rightarrow |3\rangle$ transition, we obtain for the resonant steady state the f^{VTL} amplitude [53]:

$$f^{\text{VTL}} = -\frac{W(v)}{W(0)} f_{12} \frac{\left[1 + \frac{\Gamma}{\gamma}(1 - \Pi_{31})\right] f_{13} I_c}{(1 + \gamma/\Gamma) I_{\text{sat}} + \left(1 + \frac{\Gamma}{\gamma} \frac{1 - \Pi_{31}}{2}\right) f_{13} I_c} \quad (3.28)$$

with the Gaussian $W(v)$ probability calculated at the atomic velocity v given by

$$v = \frac{1}{2k} [(\omega_{31} - \omega_c) - (\omega_{21} - \omega_p)] \quad (3.29)$$

and the resonance condition

$$\omega_c + \omega_p = \omega_{21} + \omega_{31} \quad (3.30)$$

The $W(v)/W(0)$ fraction in Eq. 3.28 describes the strength reduction owing to the reduced number of absorbing atoms at velocity v . The minus sign indicates that the saturated V-type crossover produces a decreased absorption, like a simple two-level resonance. Within a three-level system the role of control and probe lasers may be reversed [49, 50]. Therefore two different velocity classes, given by Eq. 3.29 and its opposite, determine the total signal amplitude.

3.4.3 N and double-N crossover resonances

In a single \mathcal{N} -scheme the probe laser acts on the $|1\rangle \rightarrow |2\rangle$ transition and the control laser acts on the $|3\rangle \rightarrow |4\rangle$ one with one-way coupling $\Pi_{41} \neq 0$

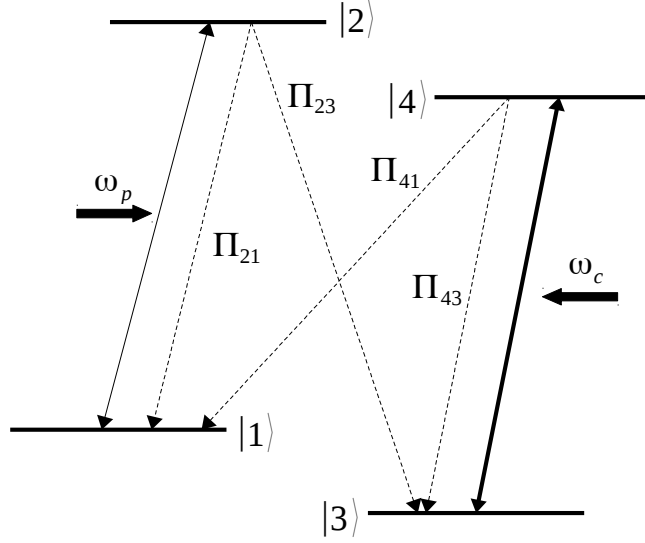


Figure 3.9: Scheme for the sub-Doppler saturation spectroscopy of a \mathcal{N} four-level system. Strong control laser at angular frequency ω_c and weak probe laser at angular frequency ω_p traveling in opposite directions excite the atomic levels. Spontaneous emission coupling between levels $i \rightarrow j$ is described by the branching ratio Π_{ij} .

and $\Pi_{23} = 0$ (see Figure 3.9). The resonant f^N amplitude of the crossover is given by

$$f^N = \frac{W(v)}{W(0)} f_{12} \frac{\Pi_{41} f_{34} I_c}{\frac{\gamma}{\Gamma} (1 + \frac{\gamma}{\Gamma}) I_{\text{sat}} + (\frac{1 - \Pi_{43}}{2} + \frac{\gamma}{\Gamma}) f_{34} I_c} \quad (3.31)$$

with $W(v)$ corresponding to the resonant atomic velocity

$$v = \frac{1}{2k} [(\omega_{43} - \omega_c) - (\omega_{21} - \omega_p)] \quad (3.32)$$

and the resonance condition

$$\omega_p + \omega_c = \omega_{21} + \omega_{43} \quad (3.33)$$

Again the $W(v)/W(0)$ fraction describes the strength reduction due to the reduced number of absorbing atoms at velocity v . The positive sign indicates that the \mathcal{N} saturation signal corresponds to an increased absorption. Within the single \mathcal{N} scheme the role of the control and probe lasers cannot be re-

versed and only one velocity class contributes to the signal. The double- \mathcal{N} crossovers are associated with a four level structure where spontaneous emission decays are present in both directions, i.e., both Π_{23} and Π_{41} are different from zero. Thus the overall level structure is equivalent to two separate \mathcal{N} schemes, where the roles of the control and probe beams are reversed. Two different velocity classes at v given by Eq. 3.32 and its opposite contribute to the absorption signals. No coherences are created between the two \mathcal{N} -scheme in a double- \mathcal{N} scheme because the connection between the levels $|2\rangle - |3\rangle$ and $|4\rangle - |1\rangle$ is made by spontaneous emission. So, the amplitude of the double- \mathcal{N} crossovers is obtained by summing up the f^N amplitudes of each \mathcal{N} configuration.

3.5 Conclusions

In this chapter we presented the basic atomic spectroscopy techniques which have been used to perform the experimental work presented in the next Chapters. Doppler-limited techniques have been exploited, thanks to their simplicity, for the high field experiment, where the experimental setup is already complicated by the typical constraints of a high magnetic field facility (Chapter 6). The detailed description of the saturated absorption spectra is helpful for the interpretation of the spectra in intermediate magnetic field (Chapter 5), in a regime where atomic lines are too close to be resolved using Doppler-limited techniques.

Chapter 4

Experimental techniques: Magnetic field production

Contents

4.1	General remarks	64
4.2	Halbach cylinder	65
4.3	Pulsed magnetic fields at LNCMI-T	72
4.4	Conclusions	75

This chapter is devoted to the description of the techniques we used to generate a magnetic field. In particular the focus will be on the production of static magnetic fields in the 0.05- 0.2 T range and on the techniques for the generation of high magnetic fields up to 100 T at the LNCMI-Toulouse. According to the characterization of the response of rubidium atoms to magnetic fields presented in Chapter 2, these two methods allow to generate static magnetic fields in the intermediate region between Zeeman and hyperfine Paschen-Back regimes and pulsed fields to investigate the hyperfine Paschen-Back regime. The experiments in static fields are a crucial step of our work; in fact they allow to test our method to measure the magnetic field using rubidium atoms performing at the same time atomic physics measurements in a simple and always available apparatus, while the utilization of the high field facility must respect a precise schedule with a limited run-time. The experiments performed in static fields will be presented in detail in Chapter 5. The results presented in Chapter 6 have been obtained using pulsed magnetic fields. In this chapter we propose a general overview of the characteristics of the available magnets at LNCMI-Toulouse and the technique employed to generate the magnetic field.

4.1 General remarks

It is well known from classical electrodynamics that an electric current produces a magnetic field. The magnetic field at the spatial position indicated by the vector \mathbf{r} generated by a current density $\mathbf{J}(\mathbf{r}')$ is described by the Biot-Savart law [54]

$$\mathbf{B}(\mathbf{r}) = \frac{\mu_0}{4\pi} \int_V \frac{\mathbf{J}(\mathbf{r}') \times (\mathbf{r} - \mathbf{r}')}{|\mathbf{r} - \mathbf{r}'|^3} d^3r' \quad (4.1)$$

where μ_0 is the vacuum permeability. Most of the techniques used to produce a magnetic field for scientific or technological applications use an electric current in various configurations depending on the desired characteristics of the field.

Another source of magnetic field are ferromagnetic materials. Ferromagnetic materials present a non-zero magnetic polarization \mathbf{M} even in absence

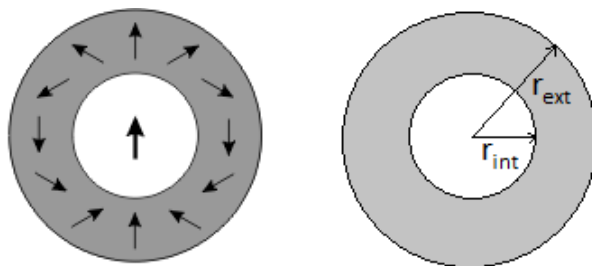


Figure 4.1: Rotation of the magnetic polarization needed to achieve a homogeneous field inside the cylinder: the magnetization vector must accomplish a complete rotation of 2π passing from a point on the cylinder shell to its diametrically opposed point.

of an applied magnetic field. The advantage of a system based on permanent magnets is that no electrical power and cooling are required while on the other side the drawbacks are mainly linked to the impossibility to modify the field strength and the fact that the produced field strength can hardly exceed a few Tesla.

We exploited the advantages of permanent magnets in order to study rubidium response in an intermediate magnetic field range, the results being presented in Chapter 5. For this we realized a particular arrangement of permanent magnets, called Halbach array, which is presented in the next Section 4.2.

4.2 Halbach cylinder

A Halbach array is a peculiar arrangement of permanent magnets whose magnetization vector follows a regular and periodic rotation along the array. Several schemes and geometries are used to obtain particular configurations of the magnetic field. Planar, cylindrical and spherical geometries are often used, depending on the symmetry properties of the desired magnetic field. This kind of structures were described by Klaus Halbach in the framework of particle accelerator technology [55] and then found application in other fields like in magnetic resonance investigations [56].

In our case we need a uniform magnetic field inside the cylindrical volume occupied by a typical rubidium vapor cell with a diameter of about 2 cm and

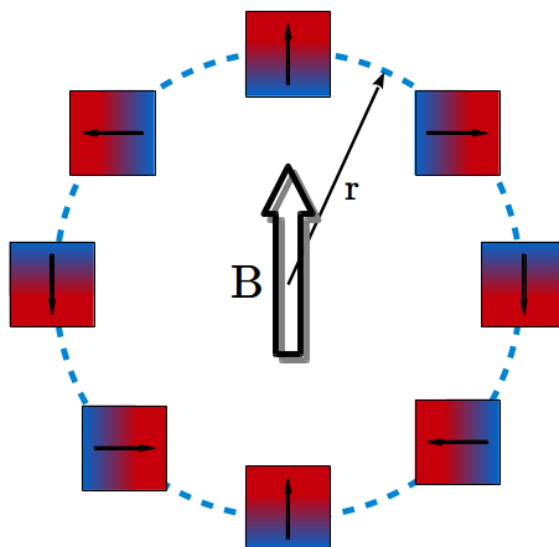


Figure 4.2: Scheme of a Halbach cylinder realized with 8 magnetic bars. The centers of the square lies on a circle whose radius is r . Arrows inside the squares indicate the orientation of the magnetization vector of the magnets.

a length of about 3 cm, so we adopted a cylindrical shape for our Halbach array. Varying the spatial periodicity of the rotation of the magnetization on the cylinder, different multipolar magnetic field configurations can be obtained. Figure 4.1 shows the periodicity needed for a uniform magnetic field: the magnetization vector must accomplish a complete rotation of 2π passing from a point on the cylinder shell to its diametrically opposed point.

For a first estimation of the magnetic field strength that one can obtain with given geometrical dimensions of the cylinder we consider the ideal case of a continuously varying magnetization on an infinitely long cylindrical shell. The magnetic field strength inside the cylinder depends only on the outer r_{ext} and inner r_{int} radius of the cylindrical shell (as shown in Figure 4.1) and on the magnetic remanence B_r of the ferromagnetic material [57]:

$$B = B_r \log \left(\frac{r_{ext}}{r_{int}} \right) \quad (4.2)$$

Practically, a Halbach cylinder is realized with a discrete number of per-

manent magnet bar, whose magnetization is oriented following the same scheme of the continuous case. During this thesis work, several Halbach cylinders were realized using 8 magnet bars; the arrangement of the bars is shown in Figure 4.2. The fact to use single magnets instead of a continuously varying magnetization, limits the performances of the assembly in term of uniformity and strength of the magnetic field. The effects due to the finite length and the finite number of the bars can be calculated [58], so that the best achievable performance of a given assembly are known. We developed a code to calculate the magnetic field generated inside a Halbach cylinder made of 8 bars to optimize the realization of the assembly. The details of the calculation are presented in Section 4.2.2. Another limitation to the quality of the Halbach cylinder is due to the variation of the magnetic remanence in the set of magnets because, due to the quality of the fabrication process, the magnets could be not enough similar to each other. This aspect is discussed and experimentally investigated in Chapter 5.

4.2.1 Properties of permanent magnets

Ferromagnetic materials exhibit a residual magnetization even without an applied external magnetic field. In fact, as shown in Figure 4.3, the degree of magnetization of a ferromagnetic material immersed in an external magnetic field traces a closed hysteresis loop when the external magnetic field H is varied. The intersection point of the hysteresis curve with the vertical axis of Figure 4.3 gives the value of the residual magnetization of the material when the external field is switched off. This property is characterized by the magnetic remanence. The remanence is defined as the residual magnetization M_r of a material after having been exposed to a strong external magnetic field H . The external field should be strong enough to reach the saturation of the material. For our purposes (in particular for the results exposed in Chapter 5) it is important to dispose of magnetic materials with a large remanence in order to obtain magnetic field strengths around 0.1 T inside the volume of the rubidium cell. Nowadays, the strongest available magnetic materials are made of rare earth alloys. In particular two types of material are commonly used, samarium-cobalt (SmCo_5) and neodymium ($\text{Nd}_2\text{Fe}_{14}\text{B}$)

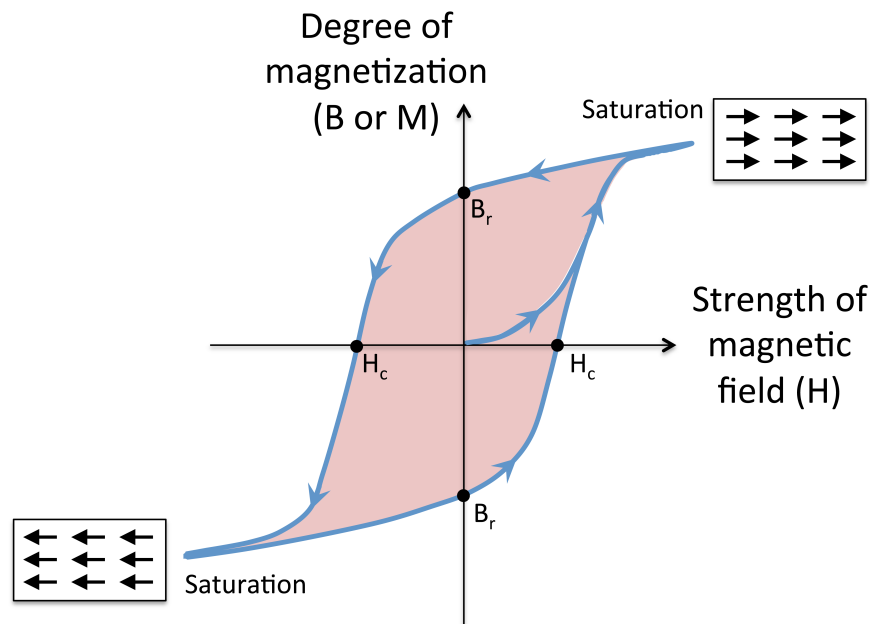


Figure 4.3: Hysteresis cycle of a ferromagnetic material with magnetic remanence and coercive field pointed out (from https://commons.wikimedia.org/wiki/File:Magnetic_hysteresis.png).

[59]. Different magnetic materials are manufactured with these compounds, which are classified by their grade. Rare earth magnets are graded according to their maximum energy product, which relates to the magnetic flux output per unit volume. Higher values indicate stronger magnets and range from N35 up to N52. Letters following the grade indicate maximum operating temperatures (often the Curie temperature), which range from M (up to 100 degrees Celsius) to EH (200 degrees Celsius) [60]. Another characteristic, which can be important when an arrangement of several permanent magnets is built, is the resistance that the material can oppose to the change of its internal magnetization when an external magnetic field is applied. This property is measured by the coercivity (or coercive field) which is defined as the intensity H_c of the external magnetic field required to reduce the magnetization of that material to zero. The coercive field is represented on the hysteresis diagram (Figure 4.3) by the intersection point between the hysteresis curve and the horizontal axis. These properties are slightly temperature-dependents, for instance for neodymium the variation of the

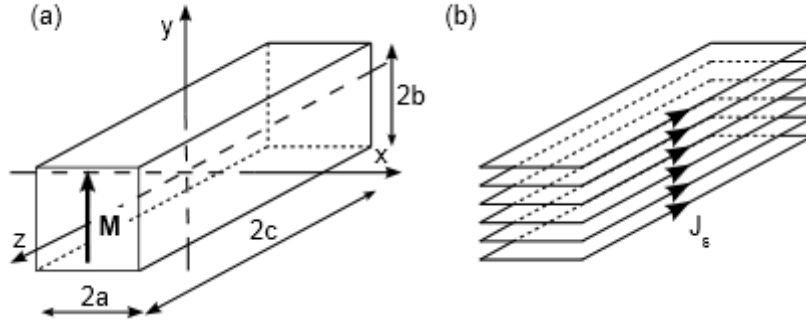


Figure 4.4: (a) A magnetic bar whose geometrical dimensions are denoted as a, b, c with magnetization M can be treated as a rectangular solenoid (b) where a density current J_s is circulating. (From [58]).

residual magnetization experiences a typical variation of -0.12% per degree Celsius while the coercivity decreases of 0.7% per degree.

Hard magnetic materials, like neodymium magnets, have a large hysteresis loop, i.e. a large coercivity; this fact allows us to neglect the effects of the reciprocal interaction between different magnets in the Halbach cylinder so that the calculation presented in next Section 4.2.2 is made simpler.

4.2.2 Computational modeling

The exact calculation of the magnetic field produced inside a Halbach cylinder is important in order to evaluate the characteristics of the field which one can expect for a given choice of the geometrical size of the assembly. In particular we used this kind of calculation to select the material and the size of the magnet bars among the commercially available items and to choose the radius of the cylinder to obtain the desired values of magnetic field strength. In addition the calculation gives the limits of the best achievable field homogeneity for a given geometry.

The magnetic field produced by a Halbach cylinder in the whole space is computed as the vector sum of the magnetic field produced by the eight magnet bars which compose the the assembly. As anticipated, we neglect the effect of the mutual interaction of the magnets, considering the coercivity being infinite. The expression of the magnetic field generated by a single

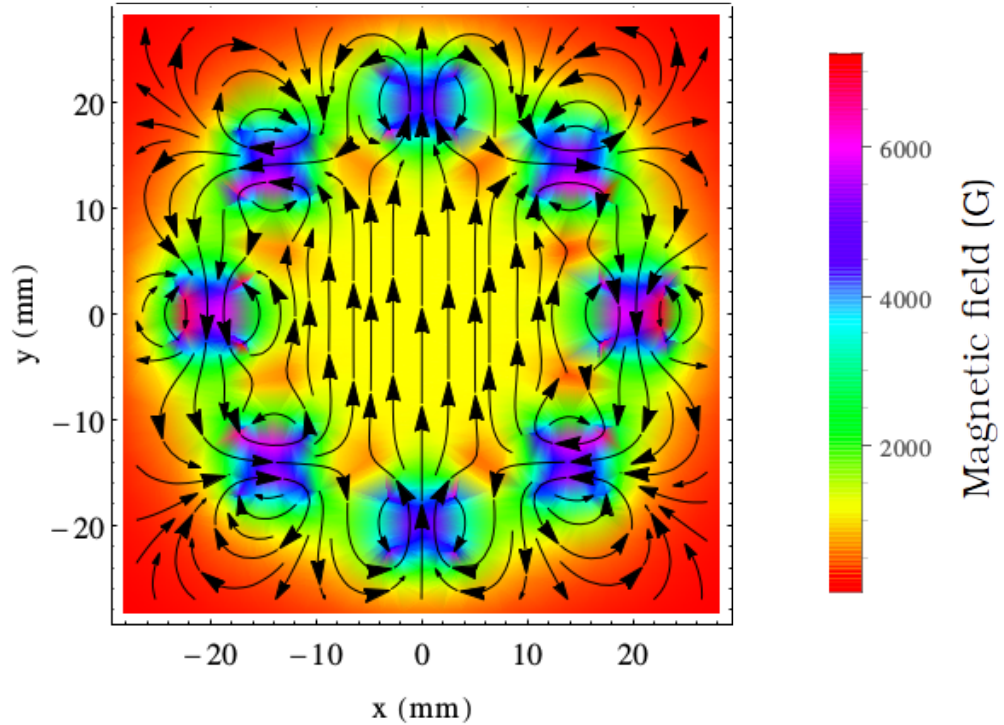


Figure 4.5: Calculated density plot of magnetic field strength the magnetic in a transverse section in center of the cylinder. The radius of the cylinder is 20 mm and its length is 148 mm. Field lines are also plotted.

bar is analytic. It is obtained considering the schematization proposed in Figure 4.4: a bar, whose geometrical dimensions are $2a$, $2b$ and $2c$, has a magnetic polarization \mathbf{M} ; magnetization \mathbf{M} can be equivalently considered as a surface current density $J_s = M$ turning around the bar surface. Analytic expression for the magnetic field produced by a rectangular solenoid are quite involved and are not reported here, but can be found in literature [61]. Then an opportune rotation and translation are applied to the vector field of each magnet bar in order to reproduce the scheme depicted in Figure 4.2.

Figures 4.5, 4.6 and 4.7 shows the results of our calculations in the case of one of the Halbach cylinder we realized (practical realization is discussed in Chapter 5). The magnets bars used for these calculations have a squared

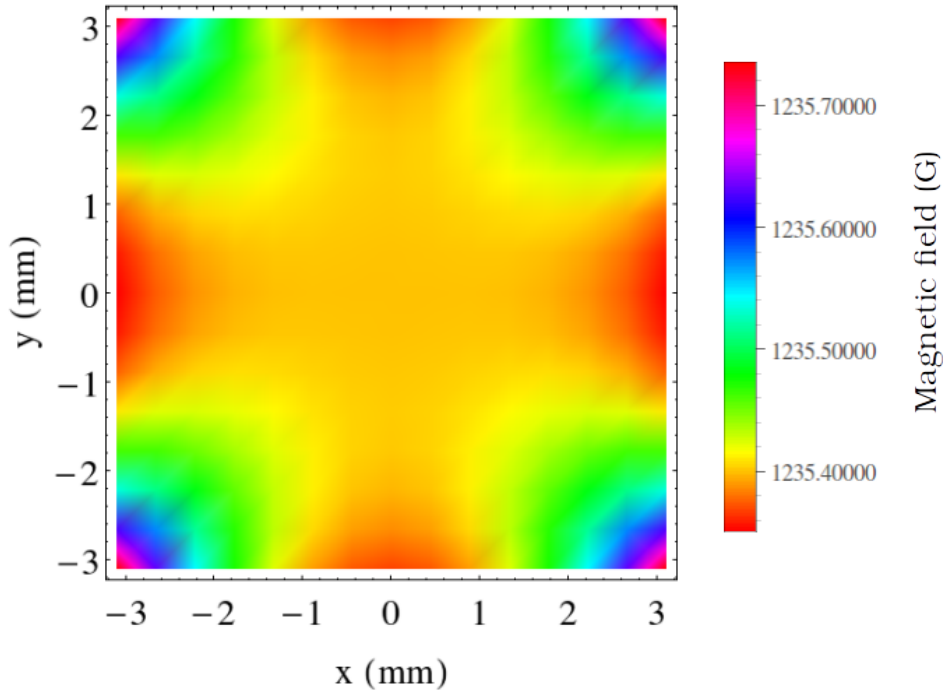


Figure 4.6: Zoom of the central region of the density plot of Figure 4.5.

section with sides of 6 mm and their length is 148 mm; they lie on a circle of radius 20 mm and they are made of 30SH neodymium alloy. Figure 4.5 proposes a map of the magnetic field strength in a transversal section at mid-length of the cylinder; also field lines are reported. As shown, the use of a finite number of discrete bars, instead of a continuously varying magnetization, causes the field to be strongly inhomogeneous near the magnets and the field lines to bend near the bars. In the central region, represented in Figure 4.6, the field is more uniform and the field lines are straight: a variation of about 0.5 Gauss is found inside a square whose side is 6 mm, to be compared with a magnetic field of about 1235 G, i.e. an inhomogeneity of about 0.04%. The result of the calculation of the longitudinal field strength profile along the axis of the cylinder is shown in Figure 4.7: the magnetic field strength as function of longitudinal coordinate (measured from the geometrical center of the cylinder), is approximately flat in a re-

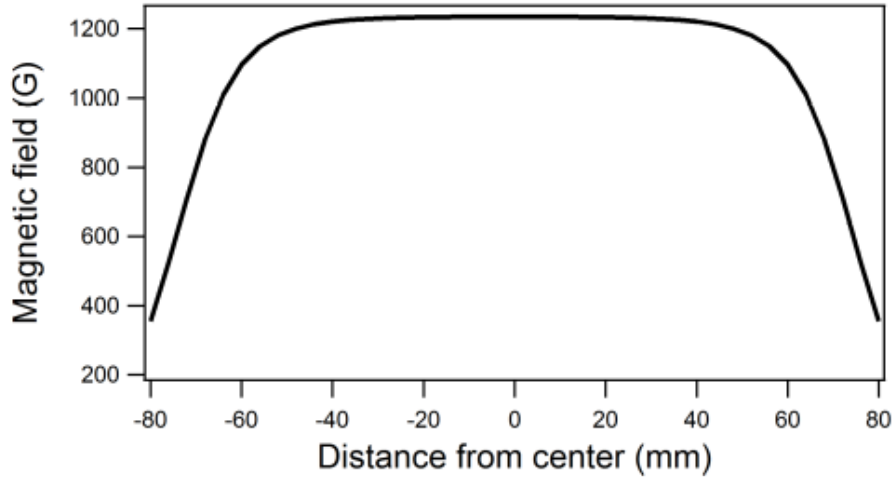


Figure 4.7: Magnetic field variation in the longitudinal direction.

gion of about 10 cm long. The variation of the magnetic field in a smaller region of 3 cm (corresponding to the length occupied by the rubidium cell for the spectroscopic observations reported in Chapter 5) is less than 2 G, i.e. about 0.2% of the strength of the magnetic field. A better uniformity of the magnetic field could be obtained using longer magnet bars.

4.3 Pulsed magnetic fields at LNCMI-T

The Laboratoire National des Champs Magnétiques Intenses in Toulouse (LNCMI-T) is a facility aimed to the production and exploitation of strong pulsed magnetic field. Magnetic fields up to about 90 T, generated by non-destructive coils, are available on the Toulouse site [62].

4.3.1 The LNCMI-T high-field facility

The generation of a strong magnetic field requires a strong current to circulate in the coil; heating due to Joule effect in a resistive conductor is proportional to I^2 . Pulsed magnetic fields allow to reach peak value of up to 90 T at LNCMI-T in a reproducible and non-destructive way because the

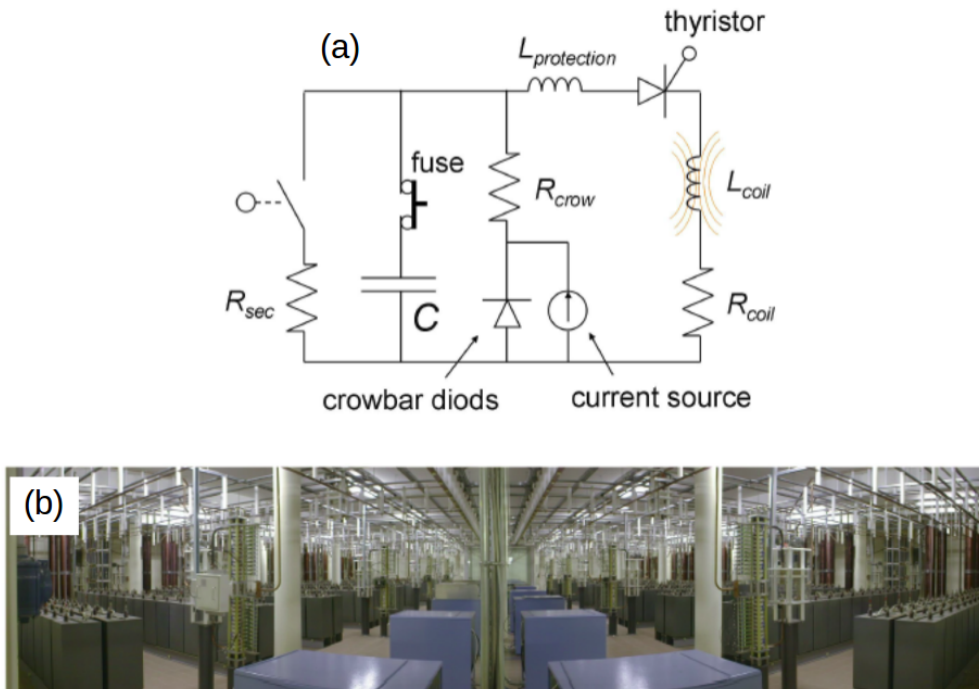


Figure 4.8: (a) Electric circuit of the generator. (b)View of the capacitor banks.

current flow is stopped before the magnets becomes overheated. The pulses have a duration of several tenth to hundreds of milliseconds, depending on the coil design. The high amount of electric energy which is needed to generate a strong magnetic field has to be delivered in a very short time duration. The adopted technical solution is to store energy in a capacitor bank. The capacitor banks of the main generator of LNCMI-T (Figure 4.8(b)) have a total capacity of 48 mF and can store energy up to 14 MJ, with a maximal voltage of 24 kV. The generator is located in the basement of the laboratory and controlled by programmable logic controller placed in the experimental room. The generator circuit is shown in Figure 4.8(a). Computer-controlled optical thyristor are used as a fast trigger for the magnet pulse. The duration of the magnet pulse can be approximated as the period of the oscillation $T = 2\pi\sqrt{LC}$, where L is the inductance of the coil and C is the capacity

of the capacitor bank. The shape of a magnet pulse (Figure 4.10) can be approximated as a damped oscillation. The rise time of a pulse is approximately $T/4 = 0.5\pi\sqrt{LC}$, then the field decreases exponentially with a time constant $\tau = L/R$, where R is the serial resistance of the crow-bar diodes and the magnet coil.

Experiments with pulsed magnetic fields are performed inside armored boxes. The typical setup inside a box consists of a magnet, high-voltage (24 kV) and high-current (65 kA) cables, cryogenics and a rack containing the electronic instruments needed for the measurement. The control of the instruments inside the box and of the generator is made via optical fibers from the experimental hall, in order to avoid electric connection between the inside and the outside of the box.

4.3.2 Pulsed magnets at LNCMI-T

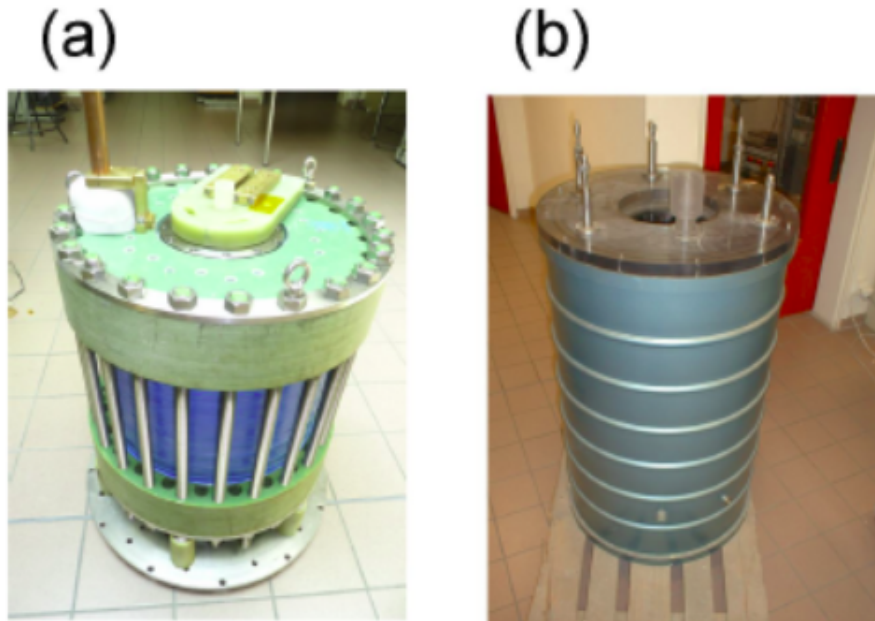


Figure 4.9: (a) Magnet coil. (b) Nitrogen cryostat containing the coil. (c) Electric circuit of the generator. (d) View of the capacitor banks.

Several different coils (Figure 4.9(a)) for pulsed magnetic fields are available at the Laboratoire National des Champs Magnétiques Intenses of Toulouse.

The magnets are resistive conductor coils, which are immersed in a nitrogen bath in an outer cryostat (Figure 4.9(b)). The coils are made of copper alloys, such as Cu+Ag or Cu+Al₂O₃, and are mechanically reinforced by layers of Zylon fiber wound around every layer of copper wire. The magnetic pressure in the magnet during the pulse is compensated by the mechanical resistance of the coil and its reinforcement. A shot at the maximum field increases the coil temperature from 77 K (boiling temperature of nitrogen) to about 300 K due to Joule effect. Temperatures higher than 300 K reduce the mechanical resistance of the materials and increase the electrical resistance of the coil with risk of damage. After a pulse the nitrogen bath cools down the magnet to reach the desired values of temperature and resistance. The cooling can take longer than one hour. Figure 4.10 offers an overview of the temporal profile of the available magnets and reports also the energy required to obtain the maximal magnetic field and the diameter of the inner bore. The diameter is reduced if an additional inner cryostat is needed to perform experiments at a temperature different from that of liquid nitrogen; in our experiment with rubidium vapors is crucial to work at room temperature in order to have a sufficient atomic vapor density to observe a signal.

The access to the pulsed field facility is regulated by the scientific committee of the European Magnetic Field Laboratory (EMFL). A proposal has to be submitted in order to use the facility for a few weeks; a requirement for acceptance is the test of the experiment in a weak field.

4.4 Conclusions

Two methods to generate a magnetic field have been described. The static field produced by permanent magnets in Halbach configuration has the advantage to be always available and can be integrated in a compact experimental setup. The intermediate regime between Zeeman and Paschen-Back effect has been studied in this condition and the results will be presented in Chapter 5. Pulsed fields have been exploited for the experiments presented in Chapter 6, where a more detailed description of the setup is proposed.

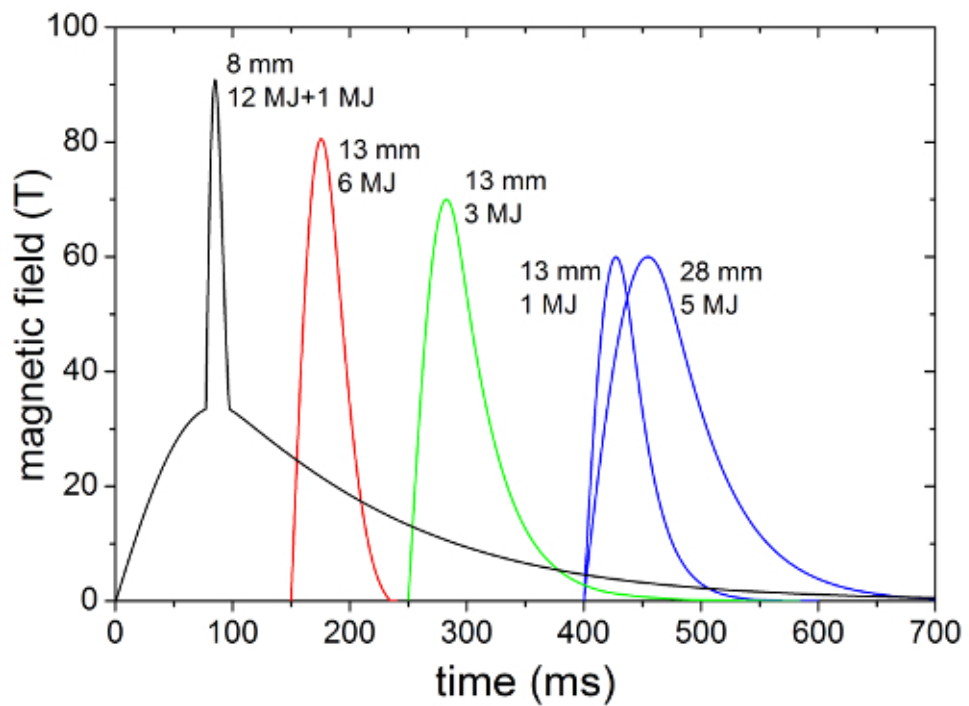


Figure 4.10: Overview of the available magnets at LNCMI-T. Temporal field profiles are plotted, the required energy and the inner bore diameter are also reported. Red, green and blue curves refer to single coil systems, while the black trace refers to a double coil system to generate a higher magnetic field.

Chapter 5

Rubidium spectra in a static magnetic field

Contents

5.1	Experimental setup	78
5.2	Spectra	87
5.3	Magnetic field evaluation	89
5.4	Line strengths and linewidths	92
5.5	Conclusions	97

Static magnetic fields produced by Halbach cylinders offer a table-top solution to perform preliminary tests of our methods. The main points to be proved are the accurate measurement of the magnetic field strength and the possibility to study atomic physics phenomena which depend on the magnetic field. We performed saturated absorption spectroscopy on the D_1 and D_2 lines for room temperature rubidium atoms immersed in magnetic fields within the 0.05-0.13 T range. At those medium-high field values the hyperfine structure in the excited state is broken by the Zeeman effect, while in the ground-state hyperfine structure and Zeeman shifts are comparable. After a brief description of the experimental setup, the analysis of the D_1 and D_2 spectra in a static magnetic field will be presented. The observed spectra are composed by a large number of absorption lines. We identified them as saturated absorptions on two-level systems, on three-level systems in a V configuration and on four-level systems in an N or double-N configuration. The analysis includes the study of the intensity of all those transitions and the comparison of their properties with the theory of saturated absorption outlined in Chapter 3. A value of the magnetic field strength is then inferred from each spectrum which shows the consistency of the method.

5.1 Experimental setup

In the framework of this thesis we assembled an experimental apparatus to perform saturated absorption spectroscopy of room temperature rubidium in a static magnetic field. This kind of physics measurements has never been performed at LNCMI-T and we had to install for the very beginning a new laboratory; so the conception and the realization of the experimental setup have been an important part of the thesis work.

5.1.1 Overview

The experimental apparatus is organized in three basic blocks as illustrated in Figure 5.1. One laser (Laser 1 in Figure 5.1) is used to perform sub-Doppler spectroscopy of rubidium in static magnetic field. It is frequency scanned to observe the resonances of rubidium. A part of the light is injected in

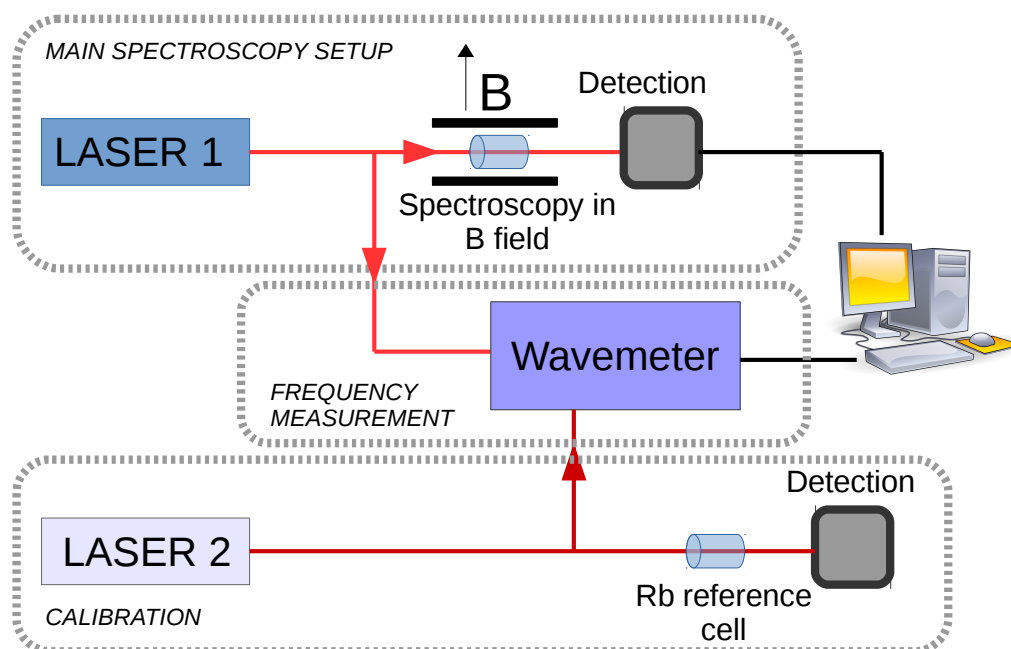


Figure 5.1: Overview of the experimental setup: three blocks corresponding to spectroscopy in magnetic field, wavemeter calibration and frequency calibration, are pointed out.

a single mode optical fiber to send it into a commercial wavelength meter (HighFinesse WS7). The frequency of the laser light is measured in real time with a sample rate of about 300 Hz while the laser frequency is scanned with typical scanning rate of 0.1 Hz. The atomic signal is sent to an acquisition card to be recorded by a computer while the wavelength meter is connected to the computer by the USB port. A Python program acquires and records the two signals. A second laser (Laser 2 in Figure 5.1) is kept locked on the saturated absorption signal of the line $F = 2 \rightarrow F' = 3$ of ^{87}Rb and is used as a reference for the calibration of the wavemeter. The wavelength meter has an absolute nominal accuracy of 60 MHz. For the experiments reported in this chapter only the knowledge of the separation between close-by absorption lines is required. Therefore, we tested its performances in term of reproducibility and accuracy in measuring the relative difference between two close frequencies. We tested the reproducibility by measuring the same frequency differences in different days and we found a reproducibility of about

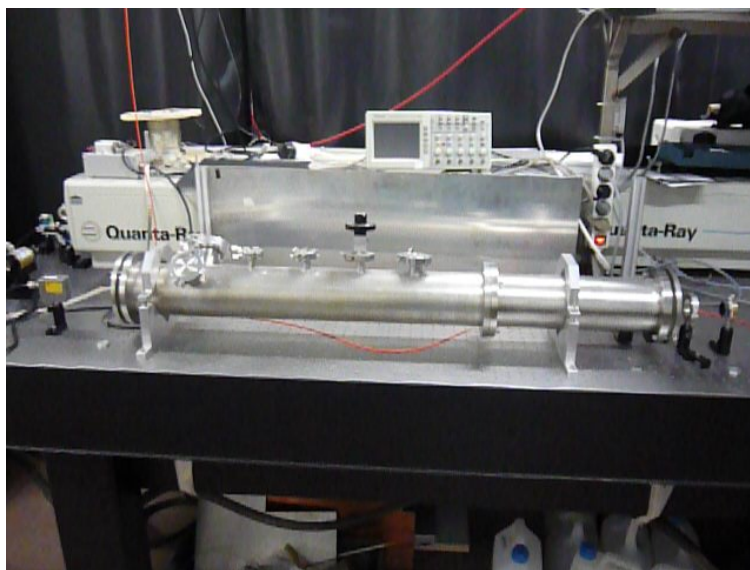


Figure 5.2: Photo of the chamber containing the Fabry-Pérot cavity.

3.5 MHz. We check then the accuracy of the wavemeter when two close frequencies are measured quasi-simultaneously, comparing the reading of the wavemeter with beat note measurements. Two lasers were used: one of them was locked on a $B = 0$ line and the other one was locked on several lines of the π spectrum in presence of a magnetic field. The explored region of spectrum is limited by the 1 GHz bandwidth of the photodetector (New Focus 1611FS-AC), nevertheless there are a quite large number of lines inside that region. The beat frequencies were measured by a spectrum analyzer (Rohde Schwarz FSC3). The two frequencies were measured by the wavemeter quasi-simultaneously (by means of a fast fiber switch). We found a standard deviation of the discrepancies between the beat measurements and the wavemeter reading of 3.3 MHz. At first, before we got the wavemeter, we realized a Fabry-Pérot cavity (Figure 5.2) in order to have a relative frequency reference to measure frequency differences. The cavity was realized using two concave mirrors with radius $R = 1$ m in confocal configuration, so the mode-spacing was about 75 MHz; the cavity was placed inside a closed chamber. Figure 5.3 shows the signals on the oscilloscope: atomic signal at $B = 0$ and in magnetic field with the Fabry-Pérot transmission signal are displayed. The analysis of the data consists in counting the Fabry-Pérot peaks between

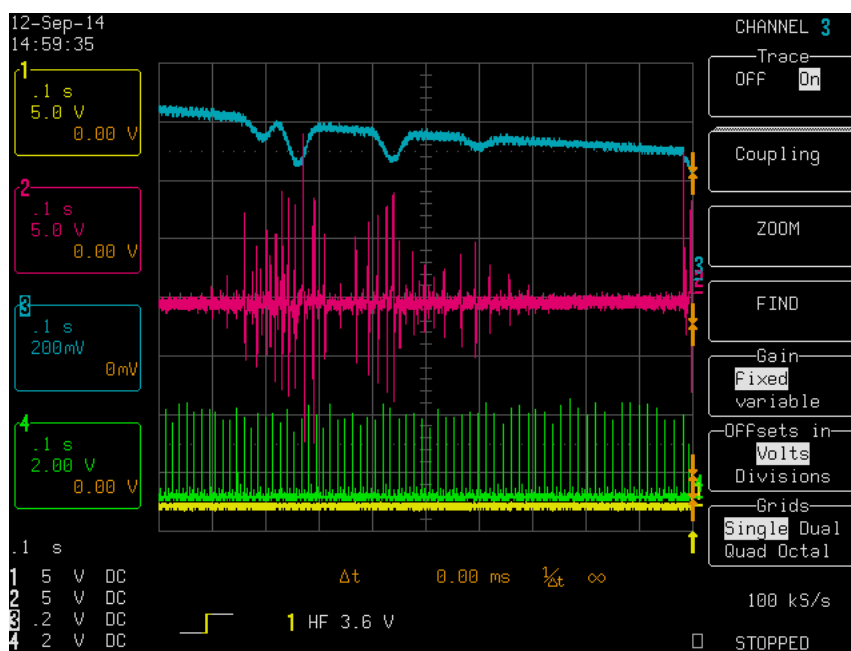


Figure 5.3: Traces on the oscilloscope: in blue the $B = 0$ Doppler limited absorption signal of rubidium, in violet the Doppler-free signal of rubidium in magnetic field and in green the Fabry-Pérot transmission signal.

the atomic resonances in order to get the frequency difference between two atomic lines. This task takes quite a long time; moreover the uncertainty on the value of the mode-spacing is propagated so that the frequency difference between two far atomic lines is typically measured with a large uncertainty. For these reasons the work on the Fabry-Pérot cavity has been abandoned once we got the commercial wavelength meter.

5.1.2 Spectroscopy setup

Laser 1 is a commercial external cavity diode laser operating in the Littrow configuration (Toptica DLX110 for spectroscopy $D2$ lines and Toptica DL100 for the $D1$ lines). The laser diode, stabilized in temperature, has a typical 1-MHz free-running linewidth and an output power up to 500 mW for the DLX110 and up to 100 mW for the DL100; the lasers beams are injected into single-mode optical fibers in order to clean the mode, so that a TEM_{00} beam is used for spectroscopy. Only a fraction of the total available power, less than

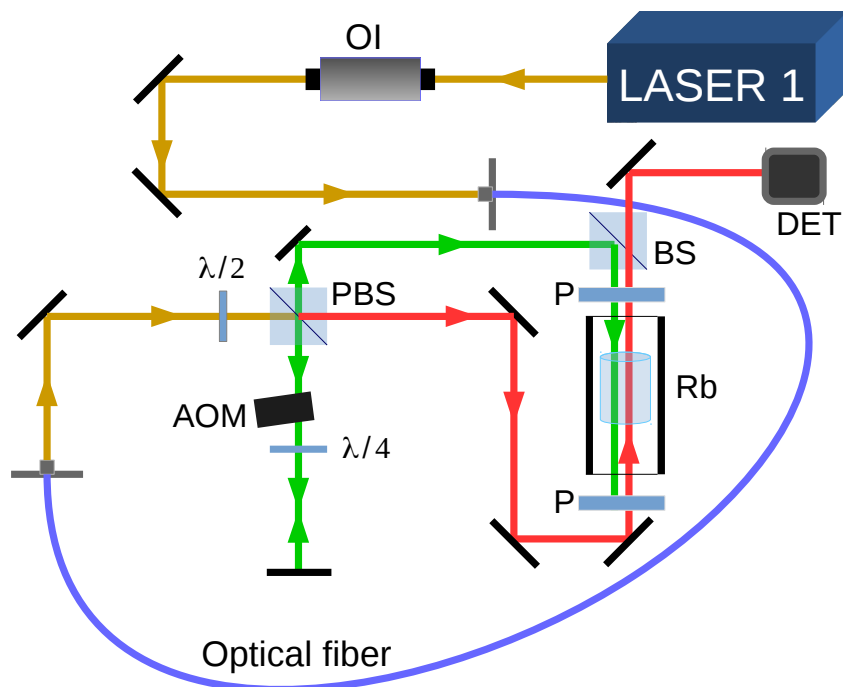


Figure 5.4: Scheme of the main elements of the saturated absorption spectroscopy setup. Red lines represent the probe beam while green lines represent the control beam. Superposition of control and probe beams inside the rubidium cell is not reproduced in the scheme for clarity. Component symbols: OI optical isolator, BS beam splitter, PBS polarizing beam splitter, AOM acousto-optical modulator, DET detector, P polarizer, $\lambda/2$ and $\lambda/4$ waveplate.

5 mW, is used for spectroscopy. Through the optimization of laser parameters we get a mode-hop free scanning range of about 15 GHz. The laser power is injected into a saturated absorption setup containing a rubidium filled glass cell placed within a Halbach cylinder. The rubidium vapor cell contains ^{85}Rb and ^{87}Rb in natural abundance. The control beam is frequency modulated by passing through an acousto-optic modulator (Crystal Technology 3110) in double passage; the probe transmitted light is monitored by a photodiode (Thorlabs FDS100) equipped with homemade transimpedance amplifier and its signal is sent to a lock-in amplifier (SR830) working at the 50-kHz modulation

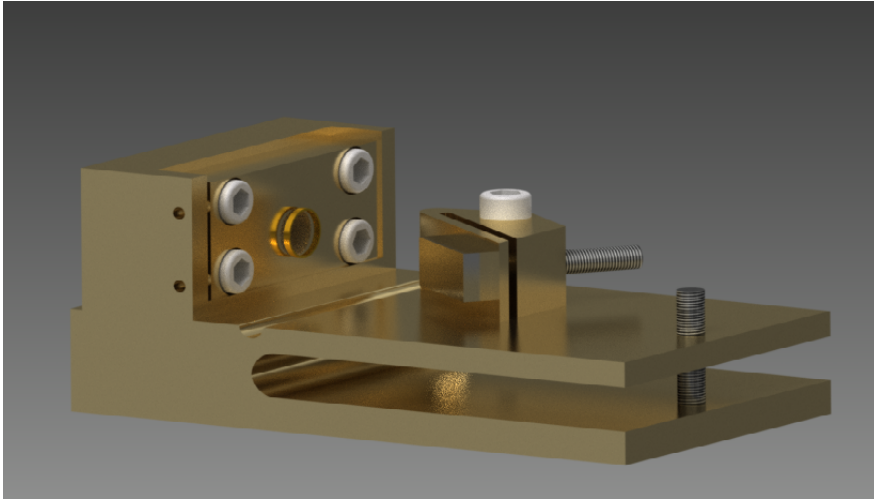


Figure 5.5: Three-dimensional view of an external cavity diode laser in Littrow configuration: maser light is collimated by an aspheric lens and then impinges on the diffraction grating; part of the light is reflected back into the diode while part of the light is sent out. The angle of the diffraction grating can be changed by a piezoelectric element mounted behind the grating or manually with a screw for wider movements.

frequency. The control and the probe laser propagations within the cell are collinear and perpendicular to the magnetic field direction. Two polarizers in front of the two entrances of the Halbach cylinder allow to select the light polarization of both beams, parallel or perpendicular to the magnetic field direction.

Laser 2 is a homemade external cavity diode laser in Littrow configuration (Figure 5.5) with a diode Axcel Photonics M9-785-0150-S50. The saturated absorption apparatus is analogous to the one described for Laser 1. Control beam is modulated by an acousto-optical modulator (Crystal Technology 3080) in double passage; the probe transmitted beam is detected by a photodiode and demodulated by a lock-in amplifier. The rubidium cell is immersed in the earth's magnetic field. The dispersion-like signal obtained from modulation spectroscopy (example of the signal in Figure 3.4) is used as error signal for the servo loop to lock the laser. A part of the laser light is sent to the wavelength meter for calibration via a single mode fiber.

5.1.3 Halbach magnet: realization and performances

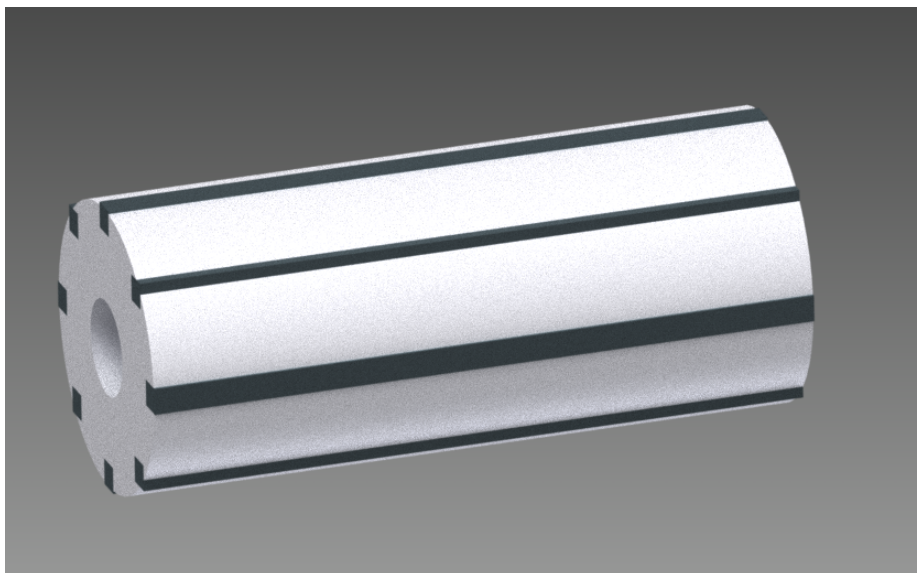


Figure 5.6: Three-dimensional view of the Halbach cylinder. The cylinder is hollow to place the rubidium cell inside. Black bars regularly placed on the surface of the cylinder represent the permanent magnets.

Several Halbach cylinder were realized with eight magnetic bars made of NdFeB (HKCM 9964-2212). The bars have dimensions $148\text{ mm} \times 6\text{ mm} \times 6\text{ mm}$ and have a nominal remanence $B_r = 1.08\text{ T}$. The bars have been mounted on a PVC cylinder with eight grooves, as shown in Figure 5.6, following the scheme sketched in Figure 4.2.

The radial dimensions of each Halbach cylinder have been determined with the help of our computational model described in Chapter 4 in order to produce the desired magnetic field strength.

As anticipated in Chapter 4, the production process of the magnets does not guarantee that all the bars are identical in term of residual magnetization [63]. This fact could negatively affect the uniformity of the magnetic field inside the Halbach cylinder, especially in the transversal plane. We performed a set of measurements on a quite large set of magnets in order to investigate the variability of their properties and to optimize the realization of the Halbach cylinders. A set of 50 magnets has been tested in order to select the 8 most similar magnets in term of magnetic remanence. We measured

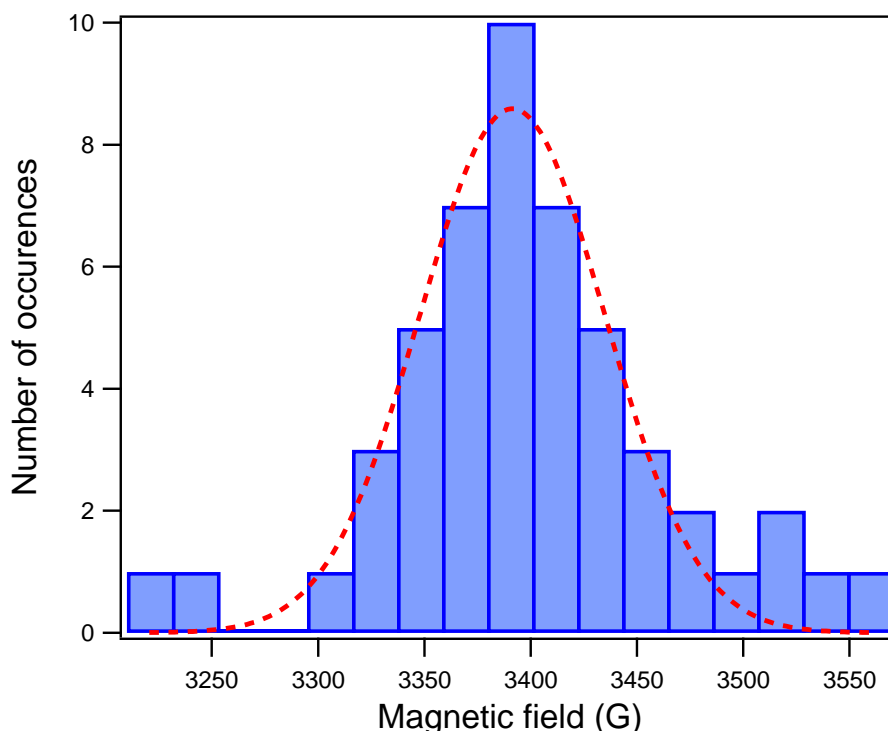


Figure 5.7: Histogram of the measured magnetic field close to surface of each of the 50 tested magnets. Red curve is a Gaussian function to guide the eye.

the magnetic field produced by each bar with a Hall effect gaussmeter. To do this we put the bar on a fixed support and we also fixed the gaussmeter so that the distance between the bar and the gaussmeter is always the same when we change the bar. The fixed distance between the gaussmeter and the surface of the magnet bar was about 1 mm. As shown in Figure 5.7 a standard deviation of about 65 G of is observed in the measured observable, that is about 2% of the mean magnetic field produced by each bar. For a better uniformity of the magnetic field inside the Halbach cylinder, eight of the bars in the central bin of the histogram in Figure 5.7 have been chosen, where the variability of the measured magnetic field is reduced to about 0.5%.

Being the magnetic field near a magnetic bar strongly dependent on the distance from the bar, the measure, to be reliable, demands a good geometrical stability. We tested our procedure by measuring each bar twice in two different positions. The two position are chosen about one centimeter on the

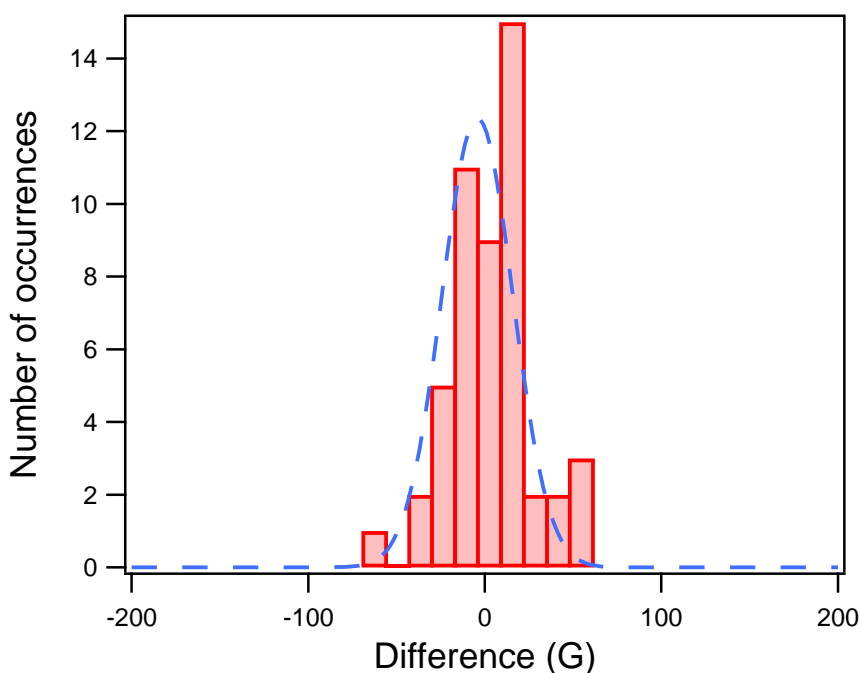


Figure 5.8: Histogram of the difference between the magnetic fields measured in two different points close to surface of each of the 50 tested magnets. Blue curve is a Gaussian function to guide the eye.

left and on the right of the center of the bar. Figure 5.8 shows that the distribution of the difference of the magnetic fields measured in these two points has a standard deviation of about 25 G, i.e. about 0.7% of the mean magnetic field. If we suppose that the value of the magnetic field measured in two points close together should be the same, we can assume this value as the indetermination of our measure procedure. Therefore, a real variation in the statistical sample of 50 magnets has been observed, not due to the measurement process itself and the selection of a subset of eight magnets makes sense.

To check the performances of the Halbach magnet, the magnetic field variation in longitudinal direction has been measured (see Figure 5.9). The cylinder has been mounted on an optical rail and its position relative to a fixed Hall effect gaussmeter was varied. The central plateau in Figure 5.9, where the field variation is less than 5%, has an extension of about 10 cm, in agreement with the provisions of the computational investigation (Figure

4.7) and the inhomogeneity in the region occupied by the rubidium cell (3 cm in length) is estimated about 4 G, i.e. about 0.3% of the strength of the field.

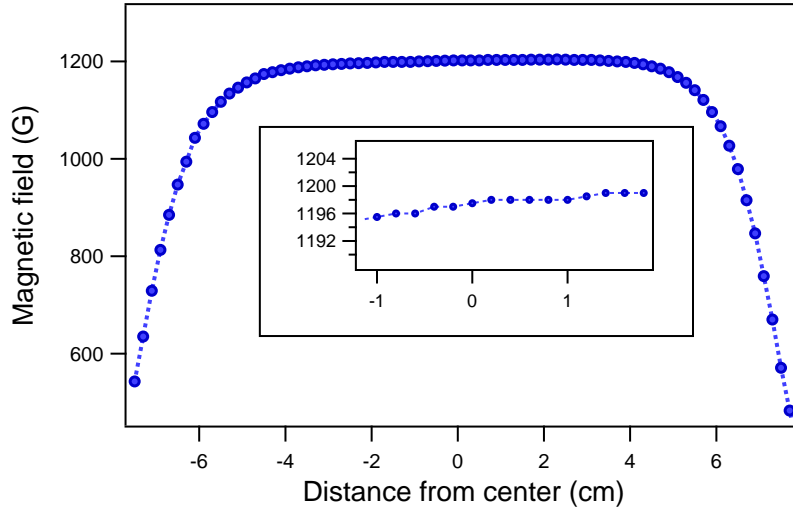


Figure 5.9: Measured longitudinal profile of the magnetic field strength inside the Halbach cylinder. In the inset: zoom on the region occupied by the rubidium vapor cell.

5.2 Spectra

We acquired saturated absorption spectra of D_1 and D_2 manifolds in various magnetic field strength ranging from 0.05 T to 0.13 T. The spectra are obtained both in π (light polarization parallel to the magnetic field direction) and σ configuration (light polarization orthogonal to the magnetic field). The configuration of the beams, which propagate perpendicular to the magnetic field direction, does not allow to separate σ^+ and σ^- transitions so that they are both present in the spectra. Both control and probe beams have the same polarization. A quite large number of resonances appears in each spectrum; in Figure 5.10 we propose a portion of the π spectra of the D_2 line in a magnetic field of about 0.126 T. The spectra contain lines with opposite signs. All lines produced by saturated absorption with control and probe lasers acting on the same two-level system have the same sign. The

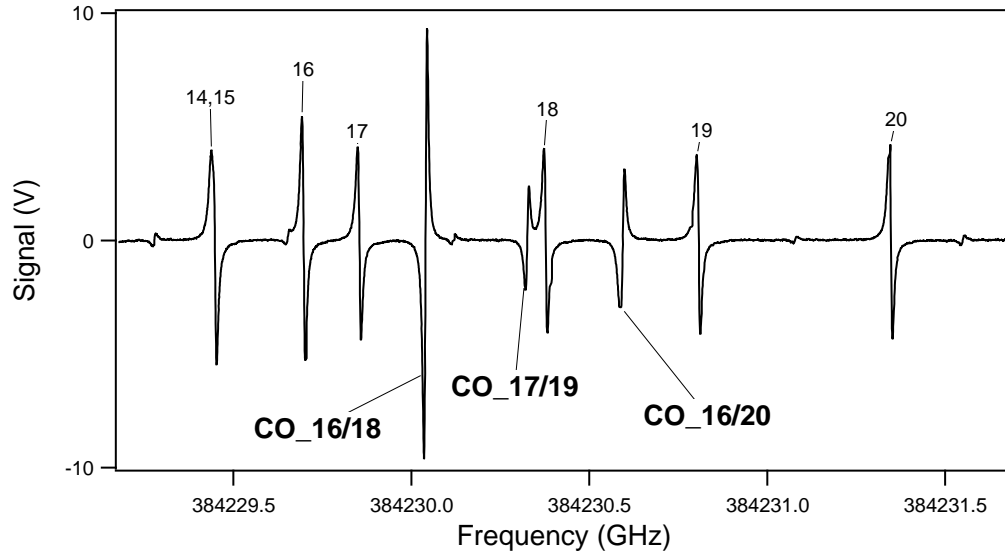


Figure 5.10: Portion of a π spectrum in a magnetic field of about 0.126 T. Two-level transition are numbered (see Table A.1 in Appendix A for the legend) while inverted crossover resonances are indicated by the labels $\text{CO}_{n/n'}$.

remaining spectra lines, labeled $\text{CO}_{n/n'}$ in Figure 5.10, are associated with crossover level schemes, as discussed in Chapter 3. The crossover features are determined by two optical transitions identified by two integer number n and n' , and the crossover label is formed listing the two participating transition obtaining the notation $\text{CO}_{n/n'}$. The crossover laser resonance condition is the median of the participating transitions. That condition is very useful in deriving the quantum numbers of the participating levels. All crossover signals of the portion of spectrum reported in Figure 5.10 are produced by the four-level configuration of Figure 3.9. They correspond to an increased absorption and therefore have a sign opposite to that of the two-level signals. The identification of the transition corresponding to each resonance is the first task that we accomplished. To do this we compared the experimental spectra with computed spectra obtained using the numerical code described in Chapter 2. In Appendix we report more spectra relative to D_1 and D_2 lines for several magnetic field strengths and both polarizations. Each spectrum is equipped with an explanatory table where the observed resonances and the corresponding transitions are listed. Atomic levels are labeled using the

basis $|F, m_F\rangle$ in the ground state while in the excited state we use the basis $|m_J, m_I\rangle$. This choice is due to the fact that with magnetic fields in the range between 0.05 and 0.13 T the excited state is well in the hyperfine Paschen-Back regime while the ground state reaches this regime at higher magnetic field strength. Each line is fitted with the derivative of a Lorentzian function in order to get the position of its center ν_i^{meas} , its intensity S_i^{meas} and its linewidth Γ_i^{meas} . The positions of the center of the resonances are given a measure of the magnetic field strength while the intensities and the linewidths are used for a study of the behavior of these parameters as a function of the line strength.

5.3 Magnetic field evaluation

The measure of the magnetic field comes from the comparison between the observed spectra and the numerical calculation described in Chapter 2. It is a crucial step for the following analysis of Section 5.4, where some field-dependent properties of the system need the knowledge of the magnetic field value to be compared with theory.

5.3.1 Method

The method used to evaluate the magnetic field strength from the spectra relies on the fact that the magnetic field is determined by the mutual distances between the resonances. For each spectrum we select a line as a reference and we measured the difference between the frequency $\nu_{\text{ref}}^{\text{meas}}$ of the chosen line and the frequencies ν_i^{meas} of all the other lines. We denote this difference as ξ :

$$\xi_i^{\text{meas}} = \nu_i^{\text{meas}} - \nu_{\text{ref}}^{\text{meas}} \quad (5.1)$$

Our numerical code can calculate the frequencies of all transitions for any magnetic field strength, so we can define the same quantity as calculated by the numerical model:

$$\xi_i(B)^{\text{calc}} = \nu_i^{\text{calc}}(B) - \nu_{\text{ref}}^{\text{calc}}(B) \quad (5.2)$$

Our best estimation of the value of the magnetic field is obtained looking for the minimum $\mathcal{S}(\bar{B})$ of the sum of squared residual between experimental and calculated frequencies as a function of the magnetic field:

$$\mathcal{S}(B) = \sum_{i=1}^n [\xi_i^{\text{meas}} - \xi_i^{\text{calc}}(B)]^2 \quad (5.3)$$

This function is sampled varying the magnetic field value with steps of 0.00001 T to look for its minimum. In order to check the consistency of the method we recorded four spectra in the same Halbach cylinder with different configurations of the light polarization (parallel or orthogonal to the magnetic field) and according the laser on the D_1 or the D_2 line. We acquired the spectra in a few hours in order to reduce magnetic field variation of the Halbach cylinder which is mainly influenced by temperature variations. This test has been repeated for two different Halbach cylinders, producing different magnetic field strengths. Table 5.1 displays the results obtained by the minimization of the \mathcal{S} function. In both cases the maximal variation in the measured magnetic field is around 0.0003 T=3 G, thus all the results obtained for the same Halbach cylinder are consistent within two standard deviations. The uncertainty reported in Table 5.1 is calculated from the uncertainty associated with the frequency measurements, as explained in the next Section 5.3.2. The values we get for the magnetic field have discrepancies of about 2% with the ones calculated using the technique described in Chapter 4; the computational model suffers of the fact that the magnetic remanence of the magnet bars is known with poor accuracy, so the agreement between the measured field and the design field is quite satisfactory.

5.3.2 Error estimation

We computed the uncertainty on the magnetic field values reported in Table 5.1 by propagating the uncertainty in the measure of the frequencies. We assume the uncertainties on the value ξ_i^{meas} to be equal to the difference between it and the theoretical value $\xi_i^{\text{calc}}(\bar{B})$ calculated at optimal field \bar{B} :

$$\Delta\xi_i^{\text{meas}} = |\xi_i^{\text{calc}}(\bar{B}) - \xi_i^{\text{meas}}| \quad (5.4)$$

Table 5.1: Magnetic field strengths inside two different Halbach cylinders extracted from experimental spectra following the procedure described in the text. For each of the two Halbach cylinders we recorded four spectra i.e. one spectrum for each light polarization (π or σ) for each component of the D line.

Configuration	$\bar{B} \pm \Delta B$
$D_1 \pi$	0.05720 ± 0.00012 T
$D_1 \sigma$	0.05711 ± 0.00012 T
$D_2 \pi$	0.05710 ± 0.00006 T
$D_2 \sigma$	0.05696 ± 0.00006 T
$D_1 \pi$	0.12603 ± 0.00010 T
$D_1 \sigma$	0.12583 ± 0.00012 T
$D_2 \pi$	0.12592 ± 0.00013 T
$D_2 \sigma$	0.12616 ± 0.00006 T

The procedure to compute the uncertainty on the magnetic field value is based on simulated random experiments [64]. We considered the quantities $\Delta\xi_i^{\text{meas}}$, as defined in Eq. 5.4, and we create a set of normal distributions centered at ξ_i^{meas} and with width $\sigma = \Delta\xi_i^{\text{meas}}$

$$N_i(x) = \frac{1}{\Delta\xi_i^{\text{meas}}\sqrt{2\pi}} \exp\left[-\frac{1}{2}\left(\frac{x - \xi_i^{\text{meas}}}{\Delta\xi_i^{\text{meas}}}\right)^2\right] \quad (5.5)$$

We then generate a new set of random values of ξ_i distributed as the defined normal function $N_i(x)$ and we repeat the fit procedure. The iteration of the described procedure gives a set of values of the magnetic field \bar{B}_k whose mean converges to \bar{B} and its standard deviation ΔB is assumed as the uncertainty on the value of the magnetic field. The results in Table 5.1 does not take in account the reproducibility and the accuracy of the wavemeter measurements; to take into account these contributions we modified the width of the distributions N_i in Eq. (5.5). After this operation, the uncertainty on the magnetic field strength ΔB is typically multiplied by a factor 2.

5.4 Line strengths and linewidths

In the previous section we used spectroscopic measures to get a value of the magnetic field; here we will profit of the knowledge of the magnetic field value to analyze in detail some other properties of the system. Thanks to the numerical code described in Chapter 2 we are able to calculate the relative intensity f_{1-2} of all observed transition and to compare it to the experimental spectra.

5.4.1 Line intensities in open systems

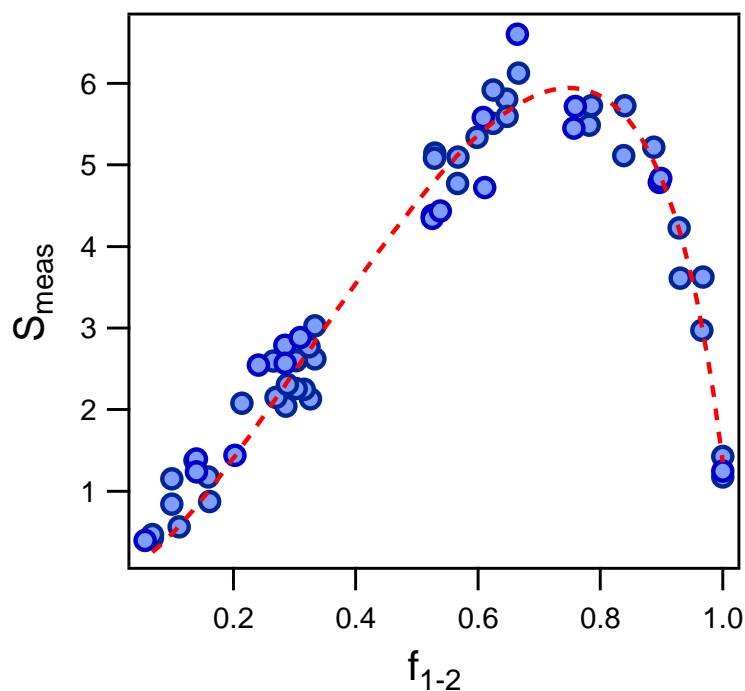


Figure 5.11: Comparison between the S_{meas} intensities of two-level saturation signals (data points) and the f_{g-e} computed relative line strengths. Both π and σ transitions are reported in the same graph. The intensity of the control beam is $I_c = 1.3 I_{\text{sat}}$. Data are fitted with the model presented in Section 3.4 (dashed line).

The removal of the degeneracy due to an intermediate-strength magnetic field and the consequent mixing of angular momentum states make possible

several optical transitions which are forbidden at zero-field. Because of this abundance of allowed atomic transitions, most of them are open and the populations of the ground state are redistributed because of optical pumping, as discussed in Section 3.4. Figure 5.11 reports the measurements of measured relative line strength S_{meas} of two-level transitions of D_2 line at 0.126 T, for a control laser intensity of $I/I_{\text{sat}} = 1.3$. Both π and σ transitions are reported in the same plot, so that a large variety of f_{g-e} values are present. The dependence of S_{meas} on f_{g-e} is linear for values of f_{g-e} lower than about 0.8 and displays an intermediate maximum for $f_{g-e} \simeq 0.8$. The intermediate maximum is observed only in σ spectra of the D_2 line because in the π spectrum and in D_1 spectra for both polarizations there are no lines whose relative intensity f_{g-e} is greater than 0.8. Data show a good agreement with the theory exposed in Chapter 3. The data in Figure 5.11 have been fitted with a curve obtained by the model reported in Section 3.4.1; if we fix the intensity the control beam, which is directly measured, we get from the fit a value of the damping rate γ of the population of the ground state (see Chapter 3). For the data reported in Figure 5.11 the fit procedure gives a value

$$\gamma = 2\pi(1.2 \pm 8) \times 10^5 \text{ s}^{-1} \quad (5.6)$$

This value of γ is compatible with the transit time of the atoms inside the illuminated volume which can be estimated considering the most probable velocity

$$u = \sqrt{\frac{2k_B T}{M}} \quad (5.7)$$

which with diameter of the control beam of 3 mm gives a transit time of about 10 μs .

Figure 5.12 reports similar comparisons for a σ spectrum at 0.072 T. Following our sign convention, we plot S_{meas} measured for the \mathcal{N} signals with a negative sign in order to distinguish them from the V-three-level signals. The f^{VTL} theoretical predictions for the V-three-level positive values are from Eq. 3.28, and the f^{N} ones for the \mathcal{N} negative values are from Eq. 3.31. All the \mathcal{N} crossover signals with $|f^{\text{N}}| > 0.3$ are produced by double- \mathcal{N} schemes, and within the σ spectra intensities larger than the $g_{g-e} = 1$ value associated with the $B = 0$ cycling transition of ^{87}Rb are fairly common. Most crossovers of

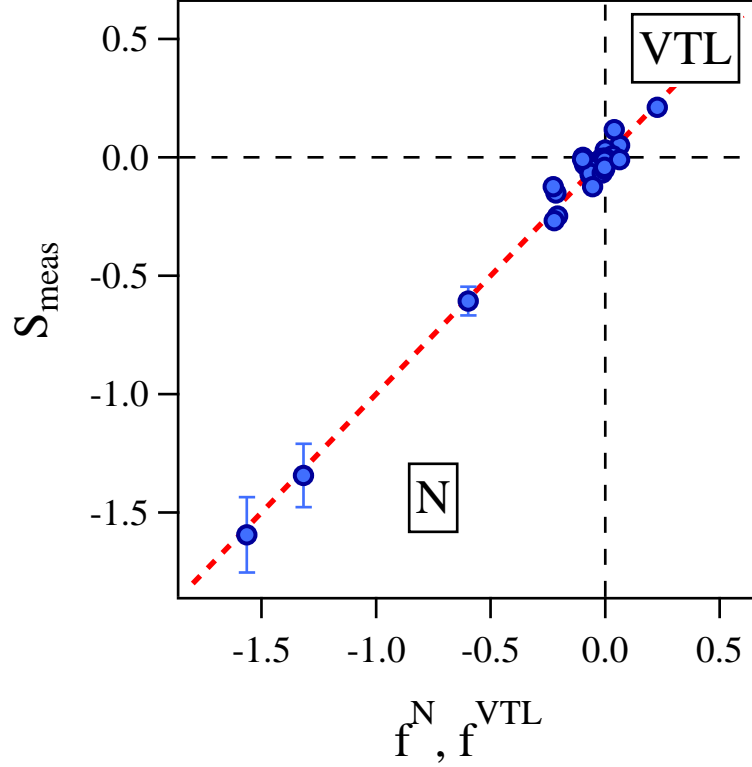


Figure 5.12: Measured S_{meas} intensities of V-three-level (VTL) and N-four-level saturation signals (data points) vs theoretical f^{VTL} and f^N , all dimensionless. Positive values correspond to VTL signals and negative values correspond to N signals. Reported data have been extracted from a σ spectrum at 0.072 T.

the σ spectra are associated with a common level configuration, with ground states within the scheme of Figure 3.9 such as $|1\rangle = |F_g = I - 1/2, m_g\rangle$ and $|3\rangle = |F_g = I + 1/2, m_g\rangle$, where I is the nuclear spin quantum number, $3/2$ and $5/2$ for the two Rb isotopes, respectively. Within the explored magnetic field range, those ground states are coupled to excited states with g_{g-e} line strength larger than 0.4. In addition, all the $|2\rangle$ and $|4\rangle$ excited states have very similar branching decay ratios, i.e., $\Pi_{21} \approx \Pi_{43}$ between 0.6 and 0.4, and $\Pi_{23} \approx \Pi_{41}$ between 0.6 and 0.4. Therefore the \mathcal{N} signals created by exchanging the role of the control and probe lasers on each \mathcal{N} scheme have comparable intensity, contributing to a total intensity which is stronger than all other signals.

5.4.2 Evolution of the transition probability

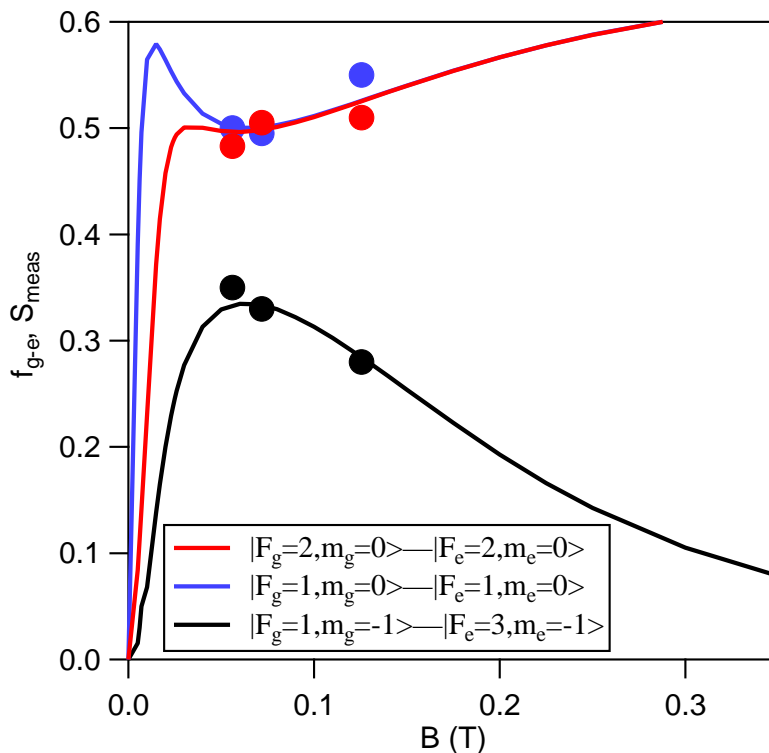


Figure 5.13: Line strength f_{g-e} vs magnetic field B for three ^{87}Rb lines with their $B = 0$ quantum numbers reported in the inset. The dots denote the S_{meas} experimental observations normalized to the black line value at 0.072 T. There is a 10% indetermination associated with the experimental values.

In the precious Section 5.4.1 we showed that the relation between the amplitude of the observed signals S_{meas} and the relative line strength f_{g-e} is linear for values of the line strength smaller than about 0.8; thus, in this range, it is possible to compare the observed amplitude S_{meas} of a given resonance at different values of the magnetic field .

In our spectra we observed some two-level lines which are forbidden at $B = 0$ because of the optical dipole selection rules. At the intermediate magnetic field strength they become allowed by the magnetic field mixing of the hyperfine eigenstates, as recently investigated for rubidium in [65] and for cesium in [66]. Within the magnetic field range of our investigation, the forbidden lines acquire a large probability, as evidenced in Figure 5.13. The

computed relative line strength f_{g-e} for three lines is plotted (continuous lines) as a function of the magnetic field strength in the 0-0.3 T range. At zero magnetic field those lines are forbidden, one of them because $\Delta F = 2$ and the other ones because they are $m_F = 0$ to $m_{F'} = 0$ transitions with $\Delta F = 0$. The dots denote the S_{meas} experimental observations for the three considered lines at three different magnetic field values, 0.056 T, 0.072 T and 0.1250 T. The amplitudes S_{meas} are normalized to the black line value at 0.072 T.

5.4.3 Linewidths

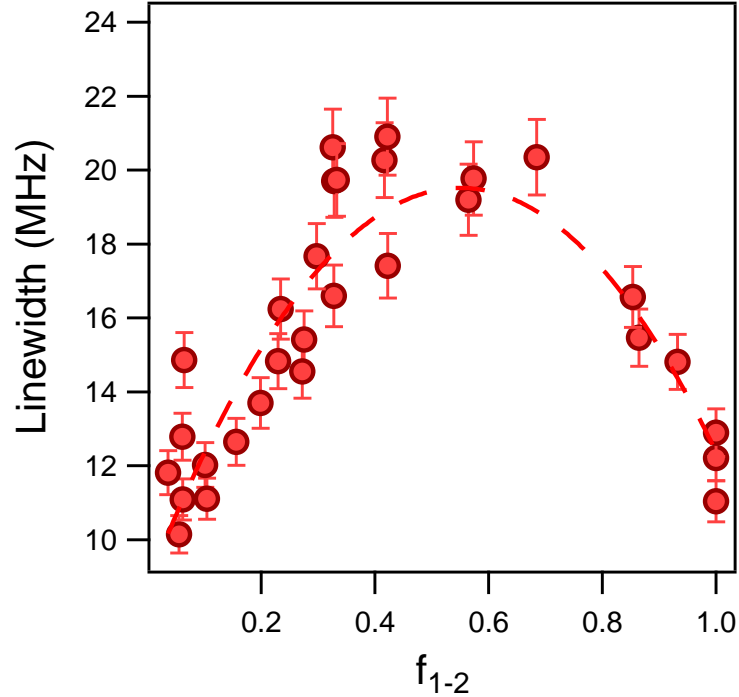


Figure 5.14: Measured linewidths of a σ spectrum of D_2 rubidium line at 0.057 T vs the relative line strength f_{1-2} .

In our spectra we observed a large variety of linewidth ranging up to approximately 20 MHz, much larger than the natural width of about 6 MHz. Here we investigate the contribution of the power broadening to the total linewidth. In Section 3.4 we presented a model of the saturated absorp-

tion spectroscopy in open atomic systems where optical pumping causes the saturation intensities to be dependent on the relative line strength f_{1-2} . Figure 5.14 reports the measured linewidths as a function of the relative line strengths f_{1-2} . Data have been obtained from the analysis of a σ spectrum at 0.057 T. The power broadened width of the $f_{1-2} = 1$ cycling transition is calculated to be about 9 MHz, from the knowledge of the control laser intensity. The observed behavior of the linewidth as a function of the relative line strength displays a central maximum where the linewidth reach value of about 20 MHz, while for values of the relative strength close to zero and to one the observed linewidths goes down to about 10 MHz. This behavior is compatible with the open system model exposed in Section 3.4, where to each line corresponding to a different value of f_{1-2} corresponds an effective saturation intensity, due to optical pumping, and consequently the experienced power broadening depends on the relative line strength f_{1-2} .

5.5 Conclusions

We have performed a sub-Doppler spectroscopic analysis of the Rb absorption in magnetic fields within the 0.05-0.13 T range. We have identified a large number of absorbing transitions. The position of the observed resonances, compared with the numerical solution of the energy levels described in Chapter 2 allows us to give the values of the magnetic field in different configuration of the laser polarizations and for transitions at 780 nm and 795 nm. All the magnetic field strengths we determined are consistent. The spectra present a large number of crossover resonances produced by three-level V-scheme and four-level \mathcal{N} configurations. No three-level Λ -scheme crossover is detected, but several of them should appear within the mixed π/σ laser scheme, which we did not investigate. Our recorded spectra present very strong saturated absorption signals produced by double- \mathcal{N} configurations where two different atomic velocity classes contribute to the absorption. The amplitudes and the width of the observed resonances have been compared with the theoretical model outlined in Chapter 3, which considers the incoherent laser-induced population transfers among atomic levels. More spectra are reported in the Appendix of this manuscript.

Chapter 6

Pulsed magnetic field metrology with rubidium atoms

Contents

6.1	Overview of the method	100
6.2	Pulsed magnetic field coil	101
6.3	Probe design and realization	102
6.4	Pick-up coil calibration	107
6.5	Experimental Set-up	108
6.6	Results	110
6.7	Conclusion	115

This Chapter is devoted to the presentation of the measure of pulsed magnetic fields with rubidium. In the previous Chapter 5 we showed how we can get a measure of a static magnetic field from spectroscopic data of rubidium; we also analyzed some atomic physics phenomena whose theoretical description depends on the value of the field. High-field experiments require a challenging miniaturization of the apparatus. The synergy with the technical staff of LNCMI-T allowed the realization of a miniaturized spectroscopy setup to probe the pulsed magnetic field. In this Chapter we describe in detail the design of the rubidium probe and we present the atomic signals we observed in pulsed magnetic field. From these data we got a measure of the magnetic field strength which can be used for *in situ* experiments on rubidium. In the final section we propose some future development of the technique and some physics experiment which could benefit of a strong magnetic field and of a precise knowledge of its strength.

6.1 Overview of the method

The measure of the magnetic field is performed using the fluorescence spectrum of rubidium and a pick-up coil. Laser light passes through the rubidium cell and the fluorescence is observed perpendicularly to the light propagation; the frequency of the laser is kept fixed during the magnetic field pulse. The resonances in the fluorescence spectrum appear when the energy shift produced by the varying magnetic field matches the selected laser frequency. If we consider the transition between the ground state level $|1/2, 3/2\rangle$ and the level $|3/2, 3/2\rangle$ of the $5P_{3/2}$ manifold of ^{87}Rb , the relation between the magnetic field strength and the resonance frequency is linear:

$$\nu = \frac{\mu_B}{4\pi}(3g_{5P} - g_{5S})B \quad (6.1)$$

where μ_B is the Bohr magneton, g_{5S} and g_{5P} are Landé factors of the ground and excited states. At the same time the temporal shape of the magnetic field pulse is monitored using a calibrated pick-up coil, serving as a fluxmeter. The observation of the considered rubidium resonance at the instant when the magnetic field satisfies the condition of Eq. (6.1) allows

to compare the value of B given by rubidium with the value given by the pick-up coil and a global scaling of the shape of the pulse can be performed.

The magnetic field indetermination ΔB is given by

$$\frac{\Delta B}{B} = \frac{\Delta \nu}{\nu} + \frac{\Delta g_{5P}}{g_{5P}} + \frac{\Delta g_{5S}}{g_{5S}} \quad (6.2)$$

where Δg_{5P} and Δg_{5S} represent the indetermination for the g -factors of the lower and upper state, respectively.

At a magnetic field of 50 T under σ laser polarization, the Zeeman shift is around 700 GHz, the fixed value of the transition frequency is measured with a commercial device (HighFinesse WS7) with an accuracy better than 60 MHz. The first term of the Zeeman frequency contribution to the magnetic field is therefore better than 10^{-4} at 50 T. A quite larger indetermination is associated to the g_{5P} -factors with respect to the one associated to the g_{5S} as discussed in Chapter 2.

6.2 Pulsed magnetic field coil

The pulsed magnetic field coil used in this experiment is a LNCMI standard 60 T coil [62]. It consist in a 24 layers of 40 turns of 9.6 mm² hard copper wire of rectangular cross section reinforced with Toyobo Zylon fibers using the distributed reinforcement technique [67]. The winding outer diameter is 270 mm and the length is 160 mm. This magnet has a 28 mm free bore diameter to perform experiments but to be cooled pulsed magnet are immersed in liquid nitrogen. So to maintain the rubidium cell at room temperature it is placed in a cryostat consisting in a double stainless steel wall separated with vacuum inserted in the magnet bore. Due to the space lost with the walls and the vacuum the room temperature bore diameter in the magnetic field is 20 mm. The magnet is connected to a capacitor bank and needs 10 kA representing 3 MJ of magnetic energy to generate 60 T. The rise time of magnetic field is about 55 ms and the time between two consecutive pulses at maximum field, necessary for the coil to cool down is one hour thanks to an annular cooling channel inserted directly in the winding [68]. In figure 6.1 we show a typical magnetic field pulse corresponding to a maximum field of

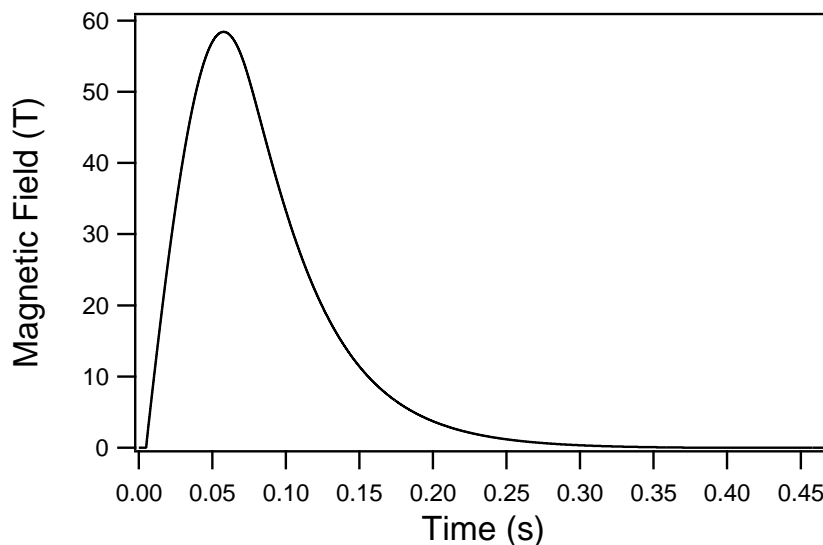


Figure 6.1: Typical magnetic field pulse corresponding to a maximum field of about 59 T.

about 59 T.

6.3 Probe design and realization

The narrow spaces inside a pulsed coil impose the realization of a miniaturized probe for rubidium spectroscopy. This task has been accomplished in close collaboration with technical staff of LNCMI-T. In figure 6.2 we show a scheme of the optics of our sensor.

The central part of the sensor is a rubidium cell of $3 \text{ mm} \times 3 \text{ mm}$ internal cross section and 30 mm length. The cell is filled with natural rubidium therefore containing both ^{85}Rb and ^{87}Rb isotopes. Laser light arrives into the cell via a single mode optical fiber (SMF IN Fiber) passing through a plan-convex lens (Lens 1) of 2 mm diameter and focal length of 4 mm to be focused into the vapor region after reflection on an aluminum coated 45° rod lens (Mirror 1) of 2 mm diameter. Before entering the cell, light is also polarized at 45° with respect to the magnetic field direction to be able to induce both π and σ transitions by a $5 \text{ mm} \times 4 \text{ mm}$ Nano-Particle Glass

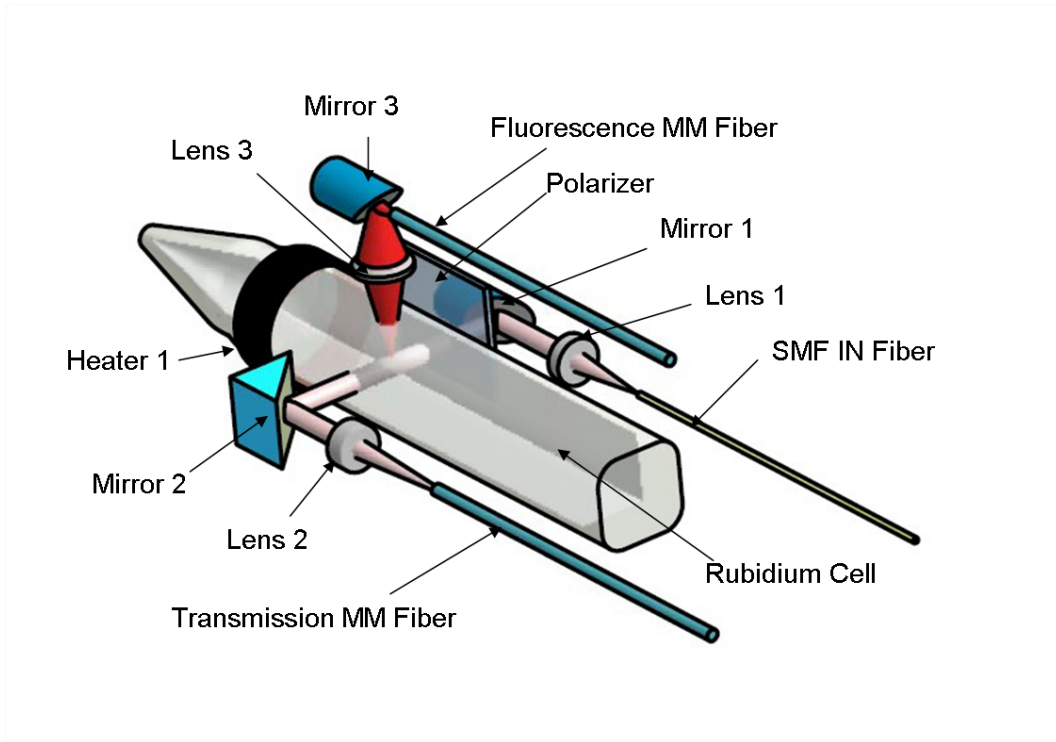


Figure 6.2: Optical scheme of our sensor.

Polarizer slab (Polarizer) of 0.26 mm thickness. Light passing through the gas after reflection on 3 mm diameter aluminum coated N-BK7 right angle mirror (Mirror 2) and after being focused by an aspheric lens (Lens 2) of 5 mm focal length is collected by a 0.39 numerical aperture, 0.2 mm core multimode optical fiber (Transmission MM Fiber). This allows us to monitor the transmission of the rubidium gas. Mirror 1 mount is coupled to an external precision mount allowing Z rotation and Z translation. Mirror 2 is glued on a flexible arm allowing X and Y rotation. At resonance, rubidium atoms absorb photons and they change their internal state from the ground level to the excited one. This excitation energy is then released as fluorescence. A particularity of our probe is to collect part of this fluorescence in a solid angle of about $0.02 \times 4\pi$ steradians. The fluorescence detected in this way coming from a volume of about 0.15 mm^3 is focused by a plan-convex lens (Lens 3) of 2.5 mm diameter and focal length of 2 mm, which is situated at

3.1 mm from the end of the optical fiber, 2.3 mm from the Rb cell and 4.3 mm from its center. Fluorescence light is then collected by a 0.39 numerical aperture, 0.2 mm core multimode optical fiber (Fluorescence MM Fiber) after being reflected by an aluminum coated 45° rod lens (Mirror 3) of 2 mm diameter. Since we will use mainly the fluorescence signal to determine the magnetic field, the volume of vapor being at the origin of the fluorescence signal gives also the spatial sensitivity of our system. Fig 6.3 gives a sketch of the fluorescence module optics.

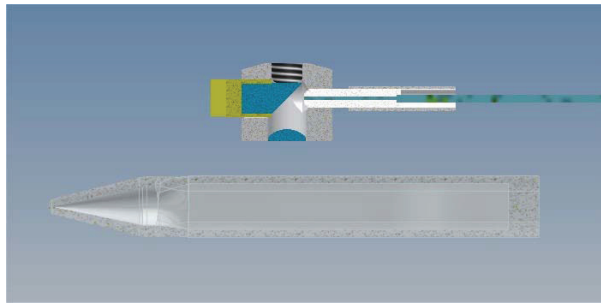


Figure 6.3: Fluorescence module optics: fluorescence light emitted by rubidium vapor is collected by a lens and injected into a multi-mode fiber via a 45° mirror.

All these elements are hosted on a structure built thanks a 3-D printer in PLA (Polylactic Acid) as shown in fig 6.4.

The fluorescence module constitutes a separate part that is aligned before operation using light propagating in the opposite direction to have a focus at about 4 mm from lens 3. Thanks to the screw threading shown in 6.3 the module is mounted on an external precision mount to find the proper positioning. Once transmission and fluorescence aligned, all the optics is glued to the PLA structure and the external precision mounts are removed. The flexible arm on which Mirror 2 is mounted is also glued.

During operation, the probe is situated in a cryostat inserted in the pulsed field magnet, as explained before. This kind of magnets is cooled with liquid nitrogen and even if the cryostat have a good level of thermal isolation at the position of the sensor the temperature can be several degrees under 0 °C. In contact with the cell with have therefore a heating system (Heater

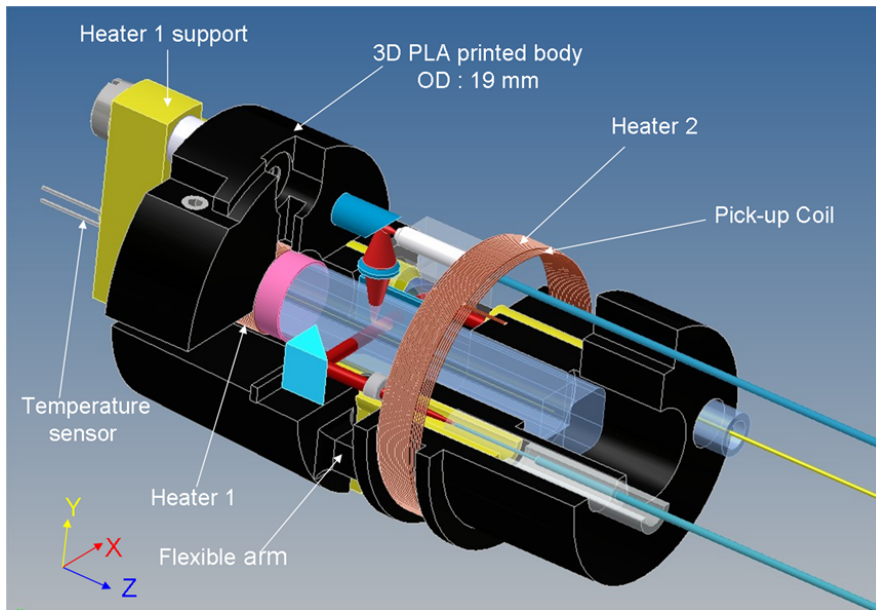


Figure 6.4: Polylactic Acid structure hosting the sensor optics.

1) to control the rubidium temperature. During standard operation power consumption of this heater is around 200 mW. Heaters mounted in our apparatus are made by winding 0.1 diameter wires of a copper, manganese and nickel alloy.

A second heater (Heater 2) surrounds the whole sensor and it is used in parallel with the first one to stabilize the gas temperature and participate therefore to the effort to keep rubidium temperature around $30\text{ }^{\circ}\text{C}$ driven by about 100 mW power, as measured by the temperature sensor located in contact with the gas cell. The overall dimension of the sensor are 40 mm length and 19 mm diameter. Figure 6.5 shows a photo of the 3D printed PLA structure and of the Rb cell.

Figure 6.6 shows a photo of the whole probe. The head of the probe contains three home-made optical vacuum feedthrough without fiber discontinuity and all the electrical connections, thanks to a twelve-contact connector (not visible in Figure 6.6). A third heater consisting of a hot air flow entrance is added to the head to increase the total heating power.

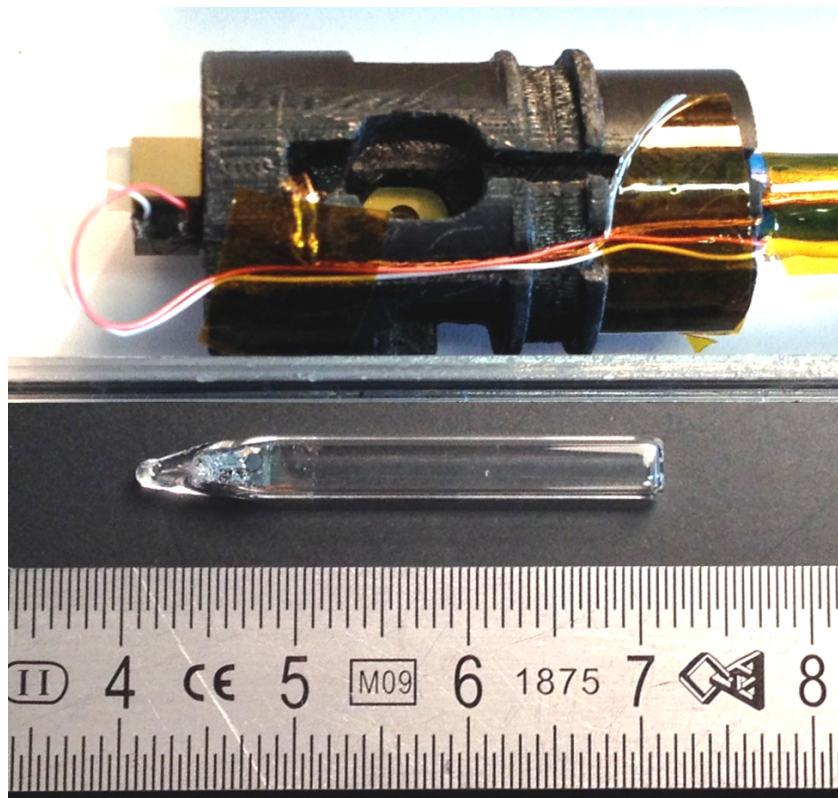


Figure 6.5: Photo of the PLA structure and of the Rb cell.

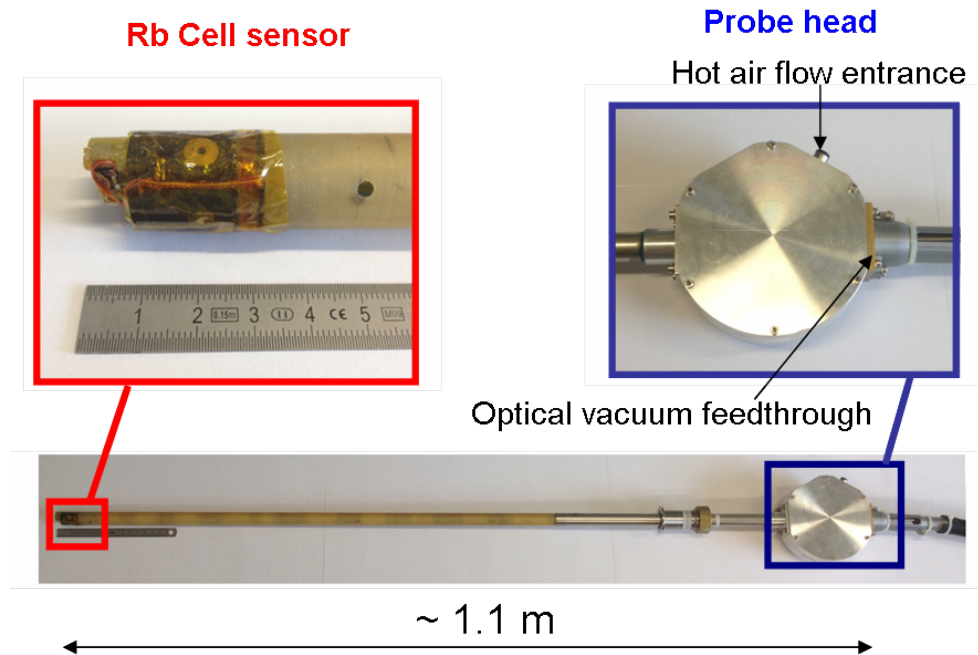


Figure 6.6: View of the whole probe.

6.4 Pick-up coil calibration

Pulsed magnetic fields are usually monitored with in situ pick-up coils. One of them, consisting in 21 turns of copper wire on an insulating mandrel perpendicular to the field direction, is therefore also hosted by the PLA structure. It is used to provide the time profile of the magnetic pulse. Once calibrated, it can be also used a magnetometer. For practical reason the pick-up coil is situated at about 7 mm of distance from the volume of gas from which the fluorescence is originated.

As usual, the evaluation of the total area of this pick-up coil is realized by inserting it in a magnetic field provided by a calibration solenoid whose geometrical properties are summarized in table 6.1.

Solenoid first layer of wire is wound on a glass fabric/epoxy tube and fixed with epoxy. The second layer, also fixed with epoxy is wound on the first layer after rectification of the additional fixation epoxy to obtain a diameter as regular as possible.

Using textbook formulas for a solenoid of finite length, the field at the

Useful inner diameter	28 mm
Number of layers	2
Number of turns per layer	1463
Wire diameter including insulation (dw)	0.34 mm
Winding length (lc)	506.00 mm \pm 0.17 mm
Number of turns per meter	5783 \pm 2 m ⁻¹
First layer inner diameter (din ₁)	30.10 mm \pm 0.02 mm
Second layer inner diameter(din ₂)	30.8 mm \pm 0.1 mm

Table 6.1: geometrical characteristics of the calibration solenoid.

center of it on the symmetry axis is such that the ratio between the driving current and the obtained field $r_{B/I}$ is $7253.4 \pm 2.5 \mu\text{T}/\text{A}$.

During calibration of the pick-up coil, the solenoid is driven by an alternating current of the order of 40 mA at frequencies varying in the range of several tens of Hz. The value of the driving current is measured with a commercial instrument whose accuracy is about 0.1 %. The signal at the ends of the pick up coil is demodulated using a lock-in amplifier. The accuracy of this instrument for voltage measurements is about 1 %. This accuracy is the limiting one for the pick-up coil calibration. The measured product of the number of turns times the pick-up surface is $(0.005266 \pm 0.000022) \text{ m}^2$. This value of the pick-up coil equivalent surface is used to recover the magnetic field value of the pulsed magnet, which is therefore given with respect to the one calculated for the calibration solenoid.

6.5 Experimental Set-up

A view of the whole experimental set-up is shown in Figure 6.7. The light beam coming from a DLX Toptica laser is sent to a reference Rb cell in the ambient field, to the commercial wavemeter to monitor its wavelength continuously and it is injected in the fiber to transport it to the sensor after passing through a half wave plate (HWP) that we use to rotate light polarization when necessary. Transmission from the reference cell is detected by a photodiode (Ph1), while transmission of the sensor Rb cell and fluorescence are monitored by photodiodes Ph2 and Ph3. All these signal are stored in a

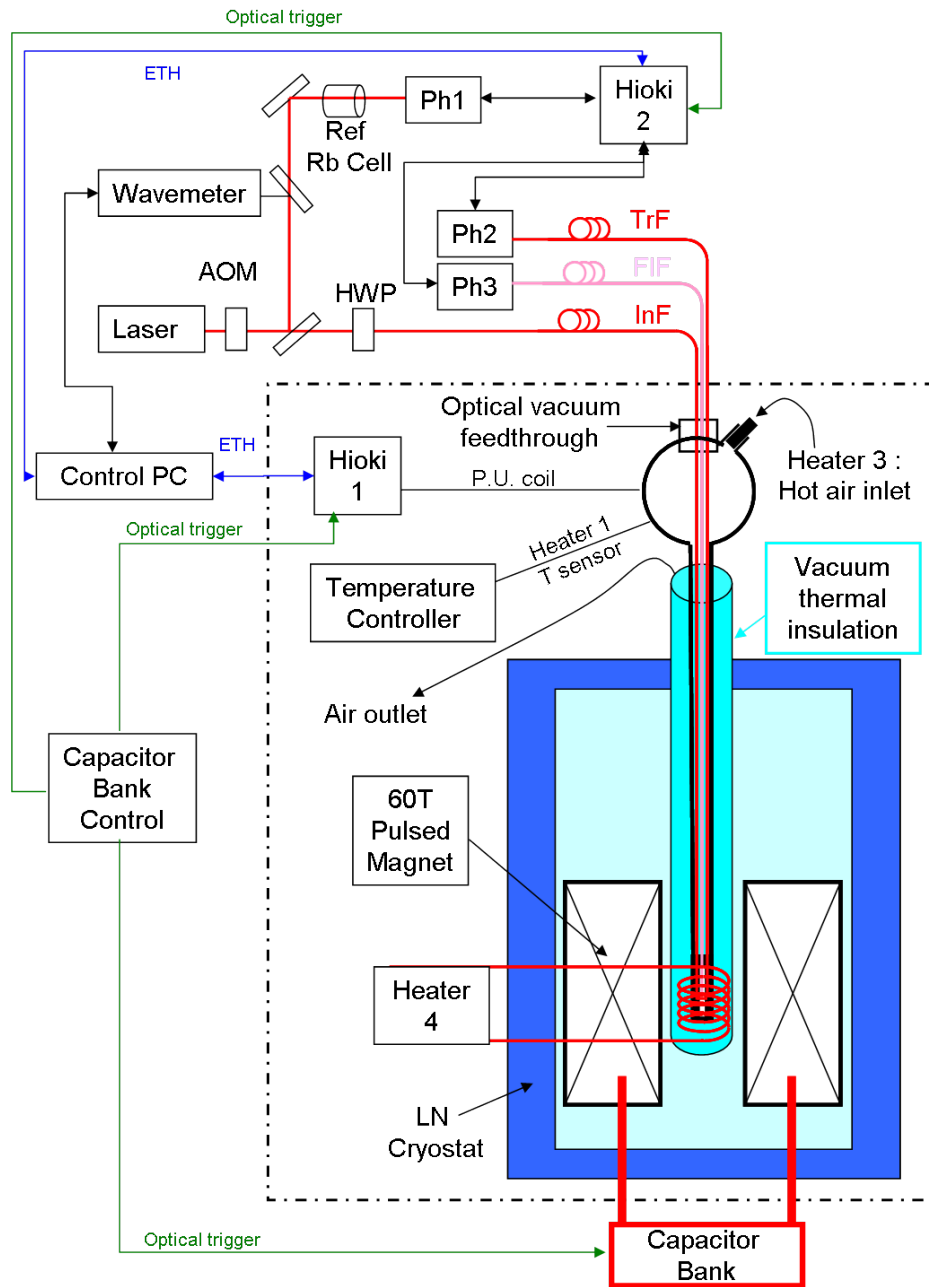


Figure 6.7: A view of the whole experimental set-up.

computer (Control PC) via a Hioki oscilloscope (Hioki 2) which also monitors the trigger signal given by the Capacitor Bank Control that delivers the optical trigger to fire the magnetic pulse.

All the instruments that are in Figure 6.7 inside the dashed box are actually inside the magnet box that is not accessible during operation for safety reasons. The connection between the box and the outside is done thanks to another Hioki oscilloscope (Hioki 1) which is also under control from the central computer (Control PC). Inside the box, hot air can be fluxed through the probe and a heater on the internal side of the vacuum isolation socket can be used to keep the cell temperature under control.

6.6 Results

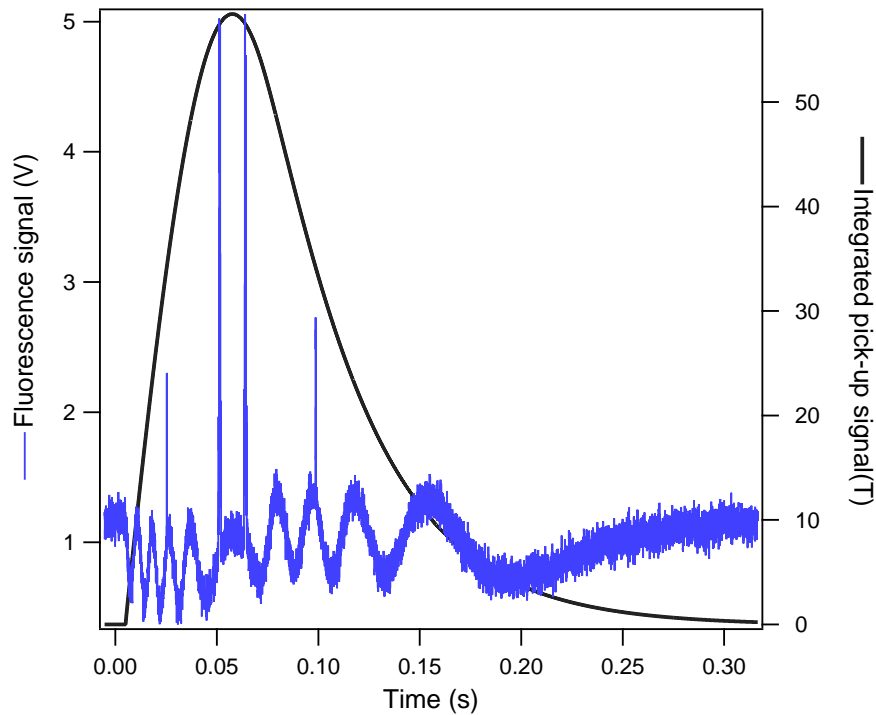


Figure 6.8: Typical data acquisition during a magnetic field pulse: in gray the integrated pick-up coil signal and in blue the signal relative to the collected fluorescence from rubidium.

We recorded rubidium fluorescence spectra and pick-up signals during several magnetic field pulses with different peak strength. Figure 6.8 shows a typical acquisition of data. In gray, the integrated pick-up signal is reported; it allows to record the temporal shape of magnetic field pulse. The accuracy of the measurement of the pick-up signal is about 0.2%, due to the voltage measurement. Another contribution to the uncertainty on the absolute magnetic field strength measured by the pick-up comes from its calibration; we estimate this contribution to be about 1%. The blue trace in Figure 6.8 shows the fluorescence signal. We observe four spikes, two of them during the rise of the field and the other ones during the decreasing phase of the pulse. Each spike is composed by four resolved resonances, as shown in Figure 6.9. The resonances appearing at higher magnetic field correspond to the σ^+ transitions $|1/2, m_I\rangle \rightarrow |3/2, m_I\rangle$ while the resonances observed at lower magnetic field correspond to the π transitions $|1/2, m_I\rangle \rightarrow |1/2, m_I\rangle$ of both isotopes. The atomic signal lies on an oscillating background: the background is due to the scattered light on the glass cell surfaces while the observed oscillation is caused by Faraday effect on the light passing through the input single mode fiber. Light inside the fibers propagates parallel to the magnetic field direction, so the polarization rotates during the pulse; the polarizer placed in front of the rubidium cell prevents light to be transmitted according to Malus law. We always select a laser frequency such that the resonances in the fluorescence signal corresponds to a maximum of the transmitted light by the polarizer.

Figure 6.9 proposes a zoom of the same data presented in Figure 6.8; we distinguish four resonances for rising and descending magnetic field. These resonances correspond to the following transitions of ^{87}Rb , in order for increasing magnetic field strength:

$$\begin{aligned}
 |1/2, -3/2\rangle &\rightarrow |3/2, -3/2\rangle \\
 |1/2, -1/2\rangle &\rightarrow |3/2, -1/2\rangle \\
 |1/2, 1/2\rangle &\rightarrow |3/2, 1/2\rangle \\
 |1/2, 3/2\rangle &\rightarrow |3/2, 3/2\rangle
 \end{aligned}$$

In addition, approximately in center of the group of four ^{87}Rb resonances

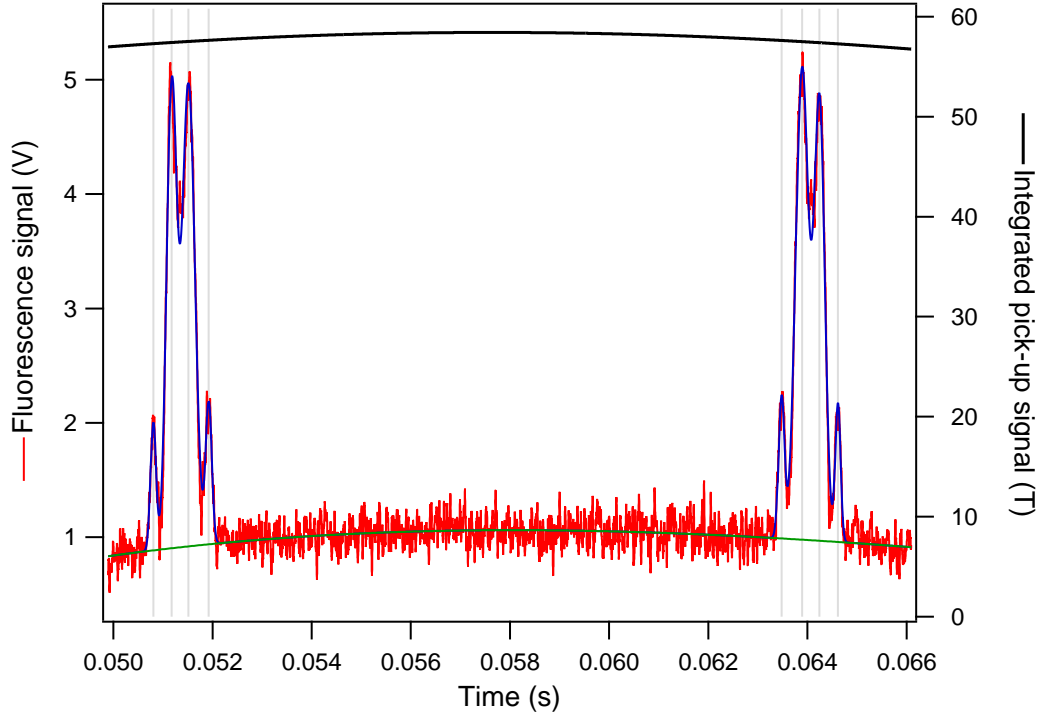


Figure 6.9: Detail of the fluorescence spectrum presented in Figure 6.8. The resonances are fitted with gaussian functions to identify their centers (vertical light gray lines).

there are six resonance of ^{85}Rb which are not resolved because their mutual separation is smaller than the Doppler width; their effect is to give an almost flat offset for the two central ^{87}Rb resonances. In principle this fact could affect the position of the observed center of the involved resonances, so we consider only the two lateral resonances of the group which do not suffer from this effect. The data presented in Figure 6.9 have been obtained with a laser frequency

$$\nu = (385042.74 \pm 0.06) \text{ GHz}$$

where the uncertainty is given by the absolute accuracy of the wavelength meter. We consider the transition $|1/2, 3/2\rangle \rightarrow |3/2, 3/2\rangle$ which, as already pointed out, experiences a linear frequency shift for any value of the magnetic field. At the given laser frequency, the center of the considered resonance

appears at the instant when the magnetic field is

$$B = (58.20 \pm 0.01) \text{ T}$$

where we computed the uncertainty using Eq. (6.2). The values of the magnetic field at the instants corresponding to the centers of the other resonances are obtained using the numerical code presented in Chapter 2. Using these

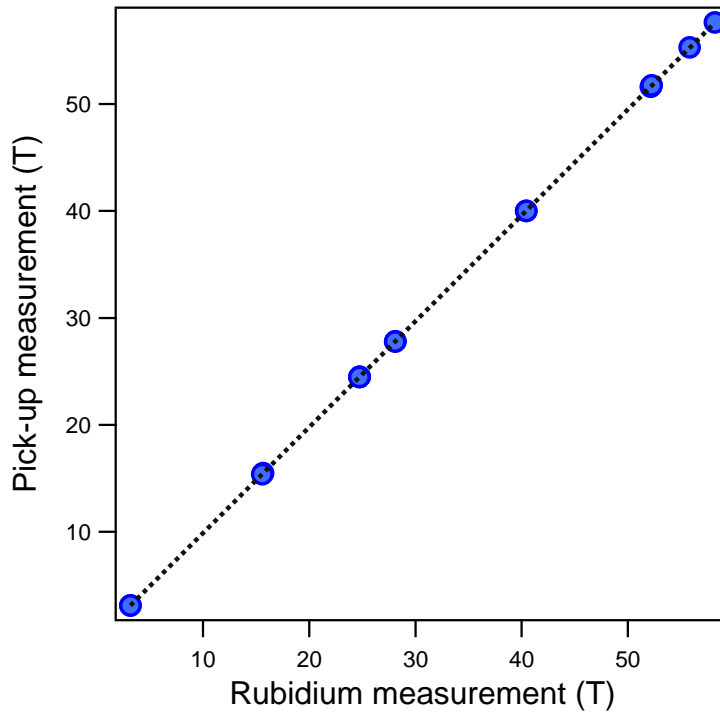


Figure 6.10: Magnetic field strength measured by the pick-up coil as a function of the magnetic field strength given by rubidium. Error bars are not represented because they are smaller than the markers in the plot.

data we rescale the temporal profile of the magnetic field pulse given by the pick-up coil; thus we obtain the magnetic field strength during the whole duration of the pulse with an accuracy of 10^{-4} , two orders of magnitude better than the calibrated pick-up coil alone. The measurement of the magnetic field provided by the pick-up coil results systematically lower of about 1% with respect to the value inferred by rubidium spectra. This behavior is confirmed at several values of magnetic fields. Figure 6.10 reports the value

of the magnetic field B_{PU} measured by the pick-up coil as a function of the values B_{Rb} given by rubidium spectra; the relation is linear and the slope of the line is

$$\frac{B_{PU}}{B_{Rb}} = 0.9898 \pm 0.0002 \quad (6.3)$$

A contribution of this discrepancy is due to the fact that the pick-up coil is located 7.5 mm higher than the probed atomic volume, as shown in Figure 6.3; this fact accounts only for 0.2% of the observed discrepancy, as can be inferred from the calculation of the longitudinal magnetic field profile of the coil and from the direct measurement performed moving the pick-up coil along the axis of the magnet (Figure 6.11). The remaining discrepancy between the values obtained with the pick-up coil and with rubidium are due to the calibration of the pick-up coil and to the measurement of its voltage.

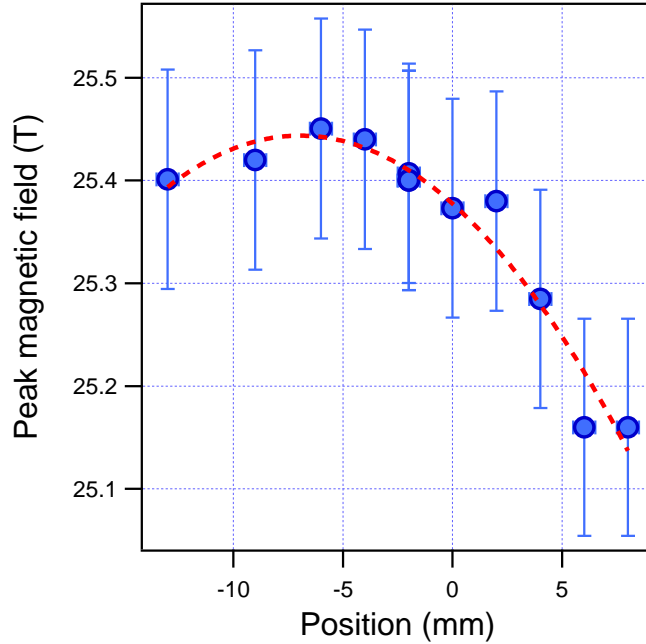


Figure 6.11: Peak values of the magnetic field measured by the pick-up coil in different longitudinal position inside the pulsed magnet.

6.7 Conclusion

We designed and realized a magnetic field sensor based on the fluorescence spectrum of rubidium in Paschen-Back regime. We illustrated in details the complex design of the rubidium probe. We demonstrated that this system is suitable to perform fast measurements of pulsed magnetic fields up to more than 58 T. The small probed volume is about 0.15 mm^3 and the attained measurement accuracy is of 10^{-4} . The accuracy is limited by the knowledge of the excited state Landé factor and by the measurement of the laser frequency. These aspects could be improved for future developments. Possible perspectives of this preliminary work will be outlined in the general conclusion of this thesis.

Chapter 7

Conclusions and perspectives

We started a new experimental activity at the *Laboratoire National des Champs Magnétiques Intenses* of Toulouse. The first goal of the project is to develop an experimental setup which allows to perform spectroscopy on atomic vapors in high magnetic fields, satisfying all the constraints imposed by a high magnetic fields facility.

In the preliminary phase of this work we installed a saturated absorption setup to perform spectroscopy in a static magnetic field produced by a Halbach cylinder. We got the magnetic field strength from the interpretation of the observed spectra, by comparison with the results of our numerical calculations. The relative uncertainty on the measured strength of the magnetic field is of the order of 10^{-3} . In this framework we studied the intensities and the widths of the observed saturated absorption resonances; the interpretation of these data requires a theoretical model of the saturation spectra involving multiple atomic levels, as we pointed out in Chapter 3 and Chapter 5.

In our experimental observations the laser-induced population transfers among the levels of \mathcal{N} -four-level schemes are incoherently produced by spontaneous emission processes. However, all the explored incoherent \mathcal{N} schemes can be transformed into coherent ones by applying an additional resonant laser radiation to perform studies about electromagnetically induced transparency [69] and slow light. As a quite straightforward application of the present scheme within the medium-high field regime and based on permanent magnets that split the atomic absorption lines, a strong reference line can be produced at any frequency close to the $B=0$ ones by properly choosing the applied magnetic field, as done by McFerran with ytterbium [70]. It may be difficult to assemble a permanent magnet array generating exactly the required field value, but a fine tuning of the magnetic field may be realized with additional Helmholtz coils. A well-designed magnet assembly will produce narrow absorption lines good enough for a simple, but precise and stable, reference setup.

After the investigations in a weak static magnetic field we developed a probe to perform atomic spectroscopy in pulsed magnetic fields, as described in Chapter 6. This challenging task led us to observe rubidium fluorescence spectra in magnetic fields up to about 58 T. We have been able to measure

pulsed fields with a relative uncertainty of about 10^{-4} . In addition to the interest of a new tool to accurately measure strong and fast magnetic fields, the probe we realized could be used to perform atomic physics investigations. A development will be to inject more than one laser into the same optical fiber in order to use a beam to measure the magnetic field and the others to perform other atomic physics experiments. For instance, injecting an input light in both optical fiber, so that the two laser beams counterpropagate inside the vapor cell, we could perform saturated absorption spectroscopy or two photon spectroscopy. These Doppler-free techniques are limited by the bandwidth of our detection system, but it should be interesting to perform this kind investigations at the static high field facility LNCMI of Grenoble. By saturation spectroscopy we could measure the Landé factor of the $5P_{1/2}$ state of rubidium, which has never been measured. Using two-photon spectroscopy we can access to the excited S states and measure the quadratic diamagnetic shift of the excited states (see Chapter 2).

Thus, the work presented in this thesis is only the first step of this new experimental activity which introduce atomic physics among the topics which can benefit of a high magnetic field.

Appendix A

D_2 spectra in static fields

In this Appendix we report D_2 rubidium spectra obtained using two different Halbach cylinders (one providing about 0.126 T and the other about 0.057 T) for both polarizations (π for the light polarization parallel to the magnetic field direction and σ for the light polarization perpendicular to the magnetic field). The resonances appearing in the spectra are labeled with a number; a table accompanying each spectrum gives the transitions corresponding to the labeled resonances. The lower level of the transition is indicated via the quantum numbers $|F, m_F\rangle$ while the upper levels are denoted by the quantum numbers $|m_J, m_I\rangle$.

Table A.1: Information about the resonances appearing in the spectrum of Figure A.1; resonances are numbered as in the spectrum. The isotope, the lower and upper levels of the transition are reported.

Number	Isotope	Lower state	Upper state
1	^{87}Rb	$ 2, 1\rangle$	$ -1/2, 3/2\rangle$
2	^{87}Rb	$ 2, 0\rangle$	$ -1/2, 1/2\rangle$
3	^{85}Rb	$ 3, 0\rangle$	$ -1/2, 1/2\rangle$
4	^{87}Rb	$ 2, -1\rangle$	$ -1/2, -1/2\rangle$
5	^{87}Rb	$ 2, 2\rangle$	$ 1/2, 3/2\rangle$
6	^{85}Rb	$ 3, -1\rangle$	$ -1/2, -1/2\rangle$
7	^{87}Rb	$ 2, 1\rangle$	$ 1/2, 1/2\rangle$
8	^{85}Rb	$ 3, -2\rangle$	$ -1/2, -3/2\rangle$
9	^{85}Rb	$ 3, 3\rangle$	$ 1/2, 5/2\rangle$
10	^{87}Rb	$ 2, -2\rangle$	$ -1/2, -3/2\rangle$
11	^{87}Rb	$ 2, 0\rangle$	$ 1/2, -1/2\rangle$
12	^{85}Rb	$ 3, 2\rangle$	$ 1/2, 3/2\rangle$
13	^{85}Rb	$ 3, 1\rangle$	$ 1/2, 1/2\rangle$
14	^{87}Rb	$ 2, -1\rangle$	$ 1/2, -3/2\rangle$
15	^{85}Rb	$ 3, 0\rangle$	$ 1/2, -1/2\rangle$
16	^{85}Rb	$ 3, -3\rangle$	$ -1/2, -5/2\rangle$
17	^{85}Rb	$ 3, -1\rangle$	$ 1/2, -3/2\rangle$
18	^{85}Rb	$ 3, -2\rangle$	$ 1/2, -5/2\rangle$
19	^{85}Rb	$ 2, -2\rangle$	$ -1/2, -3/2\rangle$
20	^{85}Rb	$ 2, -1\rangle$	$ -1/2, -1/2\rangle$
21	^{85}Rb	$ 2, 0\rangle$	$ -1/2, 1/2\rangle$
22	^{85}Rb	$ 2, 1\rangle$	$ -1/2, 3/2\rangle$
23	^{85}Rb	$ 2, 2\rangle$	$ -1/2, 5/2\rangle$
24	^{85}Rb	$ 2, -2\rangle$	$ 1/2, -5/2\rangle$
25	^{87}Rb	$ 1, -1\rangle$	$ -1/2, -1/2\rangle$
26	^{85}Rb	$ 2, -1\rangle$	$ 1/2, -3/2\rangle$
27	^{87}Rb	$ 1, 0\rangle$	$ 1/2, -1/2\rangle$
28	^{85}Rb	$ 2, 0\rangle$	$ 1/2, -1/2\rangle$
29	^{87}Rb	$ 1, 1\rangle$	$ -1/2, 3/2\rangle$

Number	Isotope	Lower state	Upper state
30	^{87}Rb	$ 1, -1\rangle$	$ 1/2, -3/2\rangle$
31	^{87}Rb	$ 1, 0\rangle$	$ 1/2, -1/2\rangle$
32	^{87}Rb	$ 1, 1\rangle$	$ 1/2, 1/2\rangle$

Table A.2: Information about the resonances appearing in the spectrum of Figure A.2; resonances are numbered as in the spectrum. The isotope, the lower and upper levels of the transition are reported.

Number	Isotope	Lower state	Upper state
1	^{87}Rb	$ 2, 1\rangle$	$ -3/2, 3/2\rangle$
2	^{87}Rb	$ 2, 0\rangle$	$ -3/2, 1/2\rangle$
3	^{85}Rb	$ 3, 0\rangle$	$ -3/2, 1/2\rangle$
4	^{87}Rb	$ 2, 2\rangle$	$ -1/2, 3/2\rangle$
5	^{87}Rb	$ 2, -1\rangle$	$ -3/2, -1/2\rangle$
6	^{85}Rb	$ 3, -1\rangle$	$ -3/2, -1/2\rangle$
7	^{87}Rb	$ 2, 1\rangle$	$ -1/2, 1/2\rangle$
8	^{85}Rb	$ 3, -2\rangle$	$ -3/2, -3/2\rangle$
9	^{85}Rb	$ 3, 3\rangle$	$ -1/2, 5/2\rangle$
10	^{85}Rb	$ 3, 2\rangle$	$ -1/2, 3/2\rangle$
11	^{85}Rb	$ 3, 0\rangle$	$ -1/2, -1/2\rangle$
12	^{87}Rb	$ 2, -1\rangle$	$ -1/2, -3/2\rangle$
13	^{85}Rb	$ 3, -3\rangle$	$ -3/2, -5/2\rangle$
14	^{85}Rb	$ 3, -1\rangle$	$ -1/2, -3/2\rangle$
15	^{85}Rb	$ 3, -2\rangle$	$ -1/2, -5/2\rangle$
16	^{85}Rb	$ 3, -2\rangle$	$ -3/2, -3/2\rangle$
17	^{85}Rb	$ 2, -1\rangle$	$ -3/2, -1/2\rangle$
18	^{85}Rb	$ 2, 0\rangle$	$ -3/2, 1/2\rangle$
19	^{85}Rb	$ 2, 1\rangle$	$ -3/2, 3/2\rangle$
20	^{87}Rb	$ 2, 2\rangle$	$ 3/2, 3/2\rangle$
21	^{85}Rb	$ 2, 2\rangle$	$ -3/2, 5/2\rangle$
22	^{87}Rb	$ 2, 1\rangle$	$ 3/2, 1/2\rangle$
23	^{87}Rb	$ 2, 0\rangle$	$ 3/2, -1/2\rangle$
24	^{85}Rb	$ 3, 3\rangle$	$ 3/2, 5/2\rangle$
25	^{85}Rb	$ 3, 2\rangle$	$ 3/2, 3/2\rangle$

Number	Isotope	Lower state	Upper state
26	^{85}Rb	$ 3, 1\rangle$	$ 3/2, 1/2\rangle$
27	^{87}Rb	$ 1, 0\rangle$	$ -3/2, 1/2\rangle$
28	^{87}Rb	$ 2, -1\rangle$	$ 3/2, -3/2\rangle$
29	^{85}Rb	$ 3, 0\rangle$	$ 3/2, -1/2\rangle$
30	^{85}Rb	$ 3, -3\rangle$	$ 1/2, -5/2\rangle$
31	^{87}Rb	$ 1, 1\rangle$	$ -3/2, 3/2\rangle$
32	^{85}Rb	$ 3, -1\rangle$	$ 3/2, -3/2\rangle$
33	^{85}Rb	$ 3, -2\rangle$	$ 3/2, -5/2\rangle$
34	^{85}Rb	$ 2, -2\rangle$	$ 1/2, -3/2\rangle$
35	^{85}Rb	$ 2, -1\rangle$	$ 1/2, -1/2\rangle$
36	^{85}Rb	$ 2, 0\rangle$	$ 1/2, 1/2\rangle$
37	^{85}Rb	$ 2, 1\rangle$	$ 1/2, 3/2\rangle$
38	^{85}Rb	$ 2, 2\rangle$	$ 1/2, 5/2\rangle$
39	^{85}Rb	$ 2, -2\rangle$	$ 3/2, -5/2\rangle$
40	^{87}Rb	$ 1, -1\rangle$	$ 1/2, -1/2\rangle$
41	^{85}Rb	$ 2, -1\rangle$	$ 3/2, -3/2\rangle$
42	^{87}Rb	$ 1, 0\rangle$	$ 1/2, 1/2\rangle$
43	^{85}Rb	$ 2, 0\rangle$	$ 3/2, -1/2\rangle$
44	^{87}Rb	$ 1, 1\rangle$	$ 1/2, 3/2\rangle$
45	^{87}Rb	$ 1, -1\rangle$	$ 3/2, -3/2\rangle$

Table A.3: Information about the resonances appearing in the spectrum of Figure A.3; resonances are numbered as in the spectrum. The isotope, the lower and upper levels of the transition are reported.

Number	Isotope	Lower state	Upper state
1	^{87}Rb	$ 2, 1\rangle$	$ 1/2, 3/2\rangle$
2	^{87}Rb	$ 2, 0\rangle$	$ -1/2, 1/2\rangle$
3	^{87}Rb	$ 2, 2\rangle$	$ 1/2, 3/2\rangle$
4	^{87}Rb	$ 2, -1\rangle$	$ -1/2, -1/2\rangle$
5	^{87}Rb	$ 2, -2\rangle$	$ -1/2, -3/2\rangle$
6	^{87}Rb	$ 2, 0\rangle$	$ 1/2, -1/2\rangle$
7	^{85}Rb	$ 3, 3\rangle$	$ 1/2, 5/2\rangle$
8	^{85}Rb	$ 3, -2\rangle$	$ -1/2, -3/2\rangle$

Number	Isotope	Lower state	Upper state
9	^{85}Rb	$ 3, 2\rangle$	$ 1/2, 3/2\rangle$
10	^{85}Rb	$ 3, 1\rangle$	$ 1/2, 1/2\rangle$
11	^{85}Rb	$ 3, -3\rangle$	$ -1/2, -5/2\rangle$
12	^{85}Rb	$ 3, 0\rangle$	$ 1/2, -1/2\rangle$
13	^{85}Rb	$ 3, -2\rangle$	$ 1/2, -5/2\rangle$
14	^{85}Rb	$ 2, -2\rangle$	$ -1/2, -3/2\rangle$
15	^{85}Rb	$ 2, -1\rangle$	$ -1/2, -1/2\rangle$
16	^{85}Rb	$ 2, 0\rangle$	$ -1/2, 1/2\rangle$
17	^{85}Rb	$ 2, 1\rangle$	$ -1/2, 3/2\rangle$
18	^{85}Rb	$ 2, 2\rangle$	$ -1/2, 5/2\rangle$
19	^{85}Rb	$ 2, -2\rangle$	$ 1/2, -5/2\rangle$
20	^{85}Rb	$ 2, -1\rangle$	$ 1/2, -3/2\rangle$
21	^{85}Rb	$ 2, 0\rangle$	$ 1/2, -1/2\rangle$
22	^{85}Rb	$ 2, 1\rangle$	$ 1/2, 1/2\rangle$
23	^{85}Rb	$ 2, 2\rangle$	$ 1/2, 3/2\rangle$
24	^{87}Rb	$ 1, -1\rangle$	$ -1/2, -1/2\rangle$
25	^{87}Rb	$ 1, 0\rangle$	$ -1/2, 1/2\rangle$
26	^{87}Rb	$ 1, 1\rangle$	$ -1/2, 3/2\rangle$
27	^{87}Rb	$ 1, -1\rangle$	$ 1/2, -3/2\rangle$
28	^{87}Rb	$ 1, 0\rangle$	$ 1/2, -1/2\rangle$
29	^{87}Rb	$ 1, 1\rangle$	$ 1/2, 1/2\rangle$

Table A.4: Information about the resonances appearing in the spectrum of Figure A.4; resonances are numbered as in the spectrum. The isotope, the lower and upper levels of the transition are reported.

Number	Isotope	Lower state	Upper state
1	^{87}Rb	$ 2, -1\rangle$	$ -3/2, -1/2\rangle$
2	^{85}Rb	$ 3, -1\rangle$	$ -3/2, -1/2\rangle$
3	^{85}Rb	$ 3, 3\rangle$	$ -1/2, 5/2\rangle$
4	^{85}Rb	$ 3, -2\rangle$	$ -3/2, -3/2\rangle$
5	^{85}Rb	$ 3, 2\rangle$	$ -1/2, 3/2\rangle$
6	^{85}Rb	$ 3, 1\rangle$	$ -1/2, 1/2\rangle$
7	^{85}Rb	$ 3, 0\rangle$	$ -1/2, -1/2\rangle$

Number	Isotope	Lower state	Upper state
8	^{85}Rb	$ 3, -3\rangle$	$ -3/2, -5/2\rangle$
9	^{85}Rb	$ 3, -1\rangle$	$ -1/2, -3/2\rangle$
10	^{87}Rb	$ 2, 1\rangle$	$ 3/2, 1/2\rangle$
11	^{87}Rb	$ 2, -2\rangle$	$ 1/2, -3/2\rangle$
12	^{87}Rb	$ 2, -1\rangle$	$ 3/2, -3/2\rangle$
13	^{85}Rb	$ 3, -1\rangle$	$ 1/2, -1/2\rangle$
14	^{85}Rb	$ 2, 1\rangle$	$ -3/2, 3/2\rangle$
15	^{85}Rb	$ 3, -2\rangle$	$ 3/2, -5/2\rangle$
16	^{85}Rb	$ 2, 2\rangle$	$ -3/2, 5/2\rangle$
17	^{85}Rb	$ 2, -1\rangle$	$ -1/2, -3/2\rangle$
18	^{85}Rb	$ 2, 0\rangle$	$ -1/2, -1/2\rangle$
19	^{85}Rb	$ 2, -2\rangle$	$ 1/2, -3/2\rangle$
20	^{85}Rb	$ 2, -1\rangle$	$ 1/2, -1/2\rangle$
21	^{87}Rb	$ 1, -1\rangle$	$ -3/2, -1/2\rangle$
22	^{85}Rb	$ 2, 0\rangle$	$ 1/2, 1/2\rangle$
23	^{87}Rb	$ 1, -1\rangle$	$ 1/2, -1/2\rangle$
24	^{87}Rb	$ 1, 1\rangle$	$ 1/2, 3/2\rangle$
25	^{87}Rb	$ 1, -1\rangle$	$ 3/2, -3/2\rangle$
26	^{87}Rb	$ 1, 0\rangle$	$ 3/2, -1/2\rangle$
27	^{87}Rb	$ 1, 1\rangle$	$ 3/2, 1/2\rangle$

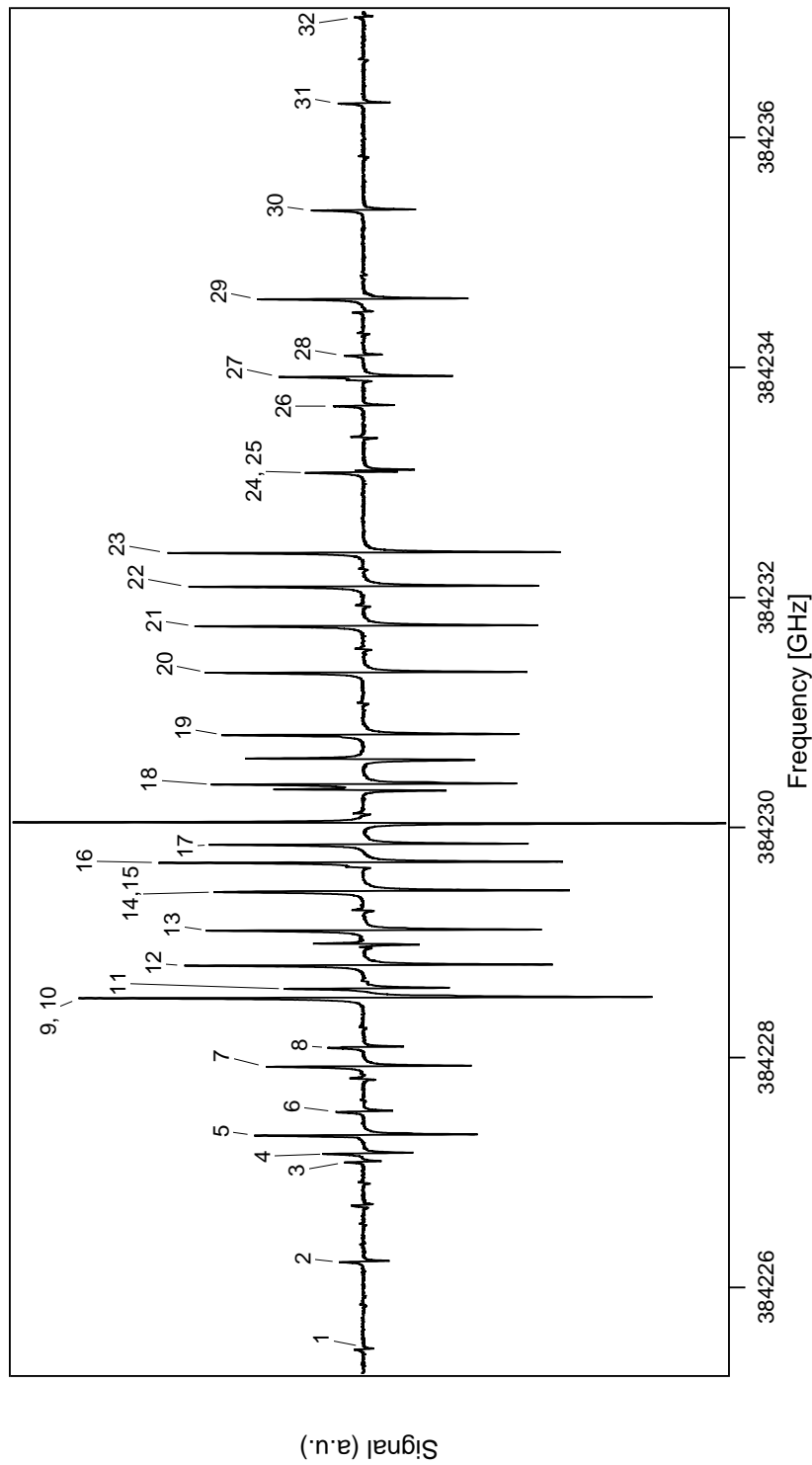


Figure A.1: Spectrum of D_2 line of rubidium in a magnetic field of about 0.126 T. Both beams are polarized parallel to the magnetic field direction. Legend in Table A.1.

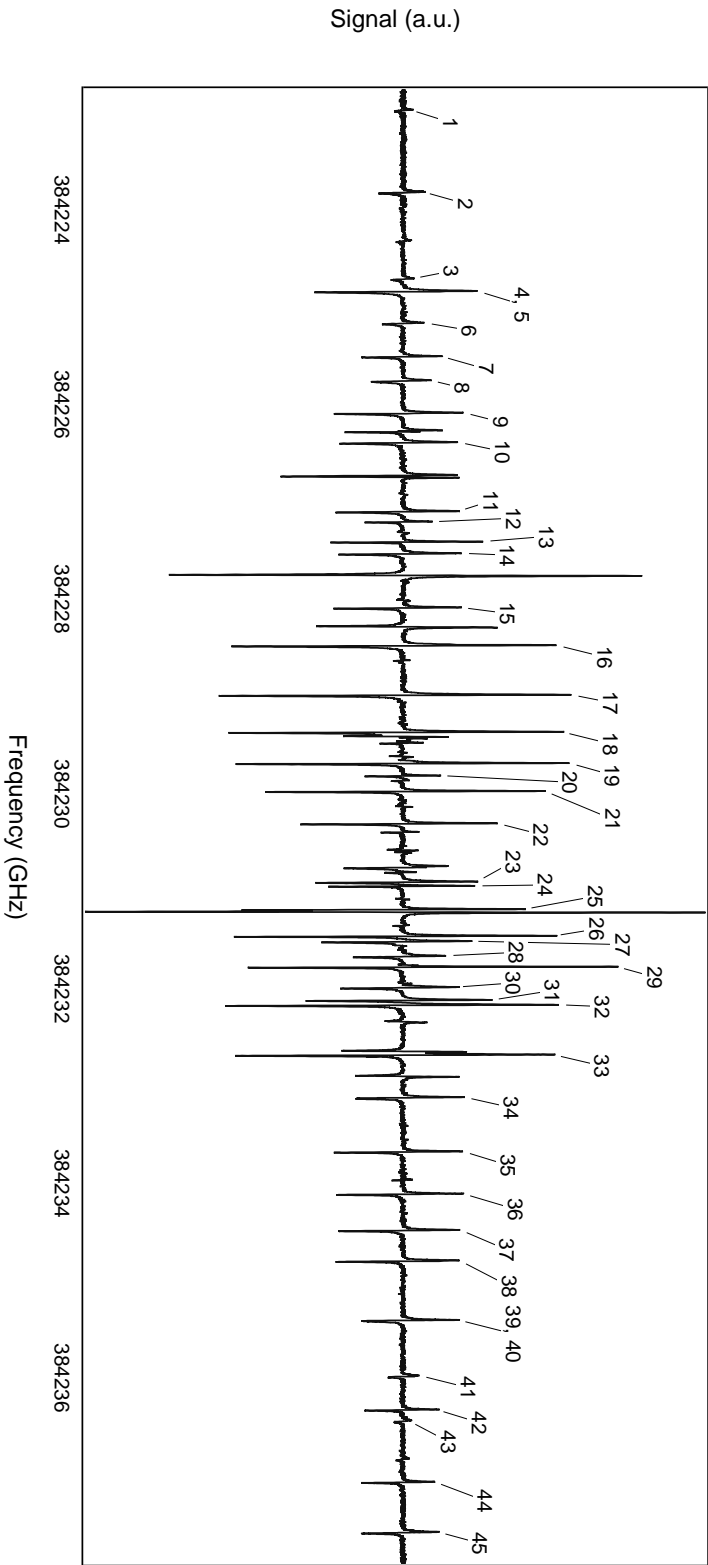


Figure A.2: Spectrum of D_2 line of rubidium in a magnetic field of about 0.126 T. Both beams are polarized perpendicular to the magnetic field direction. Legend in Table A.2.

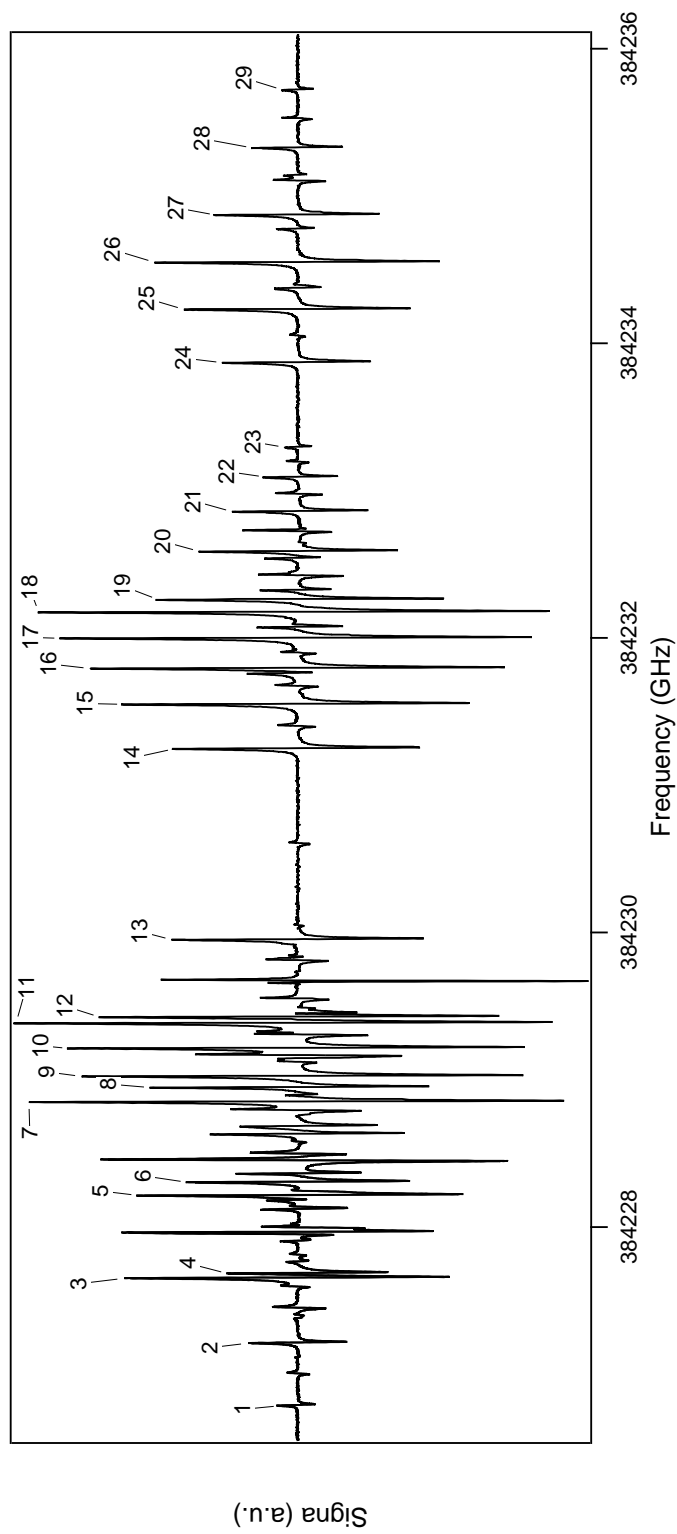


Figure A.3: Spectrum of D_2 line of rubidium in a magnetic field of about 0.057 T. Both beams are polarized parallel to the magnetic field direction. Legend in Table A.3.

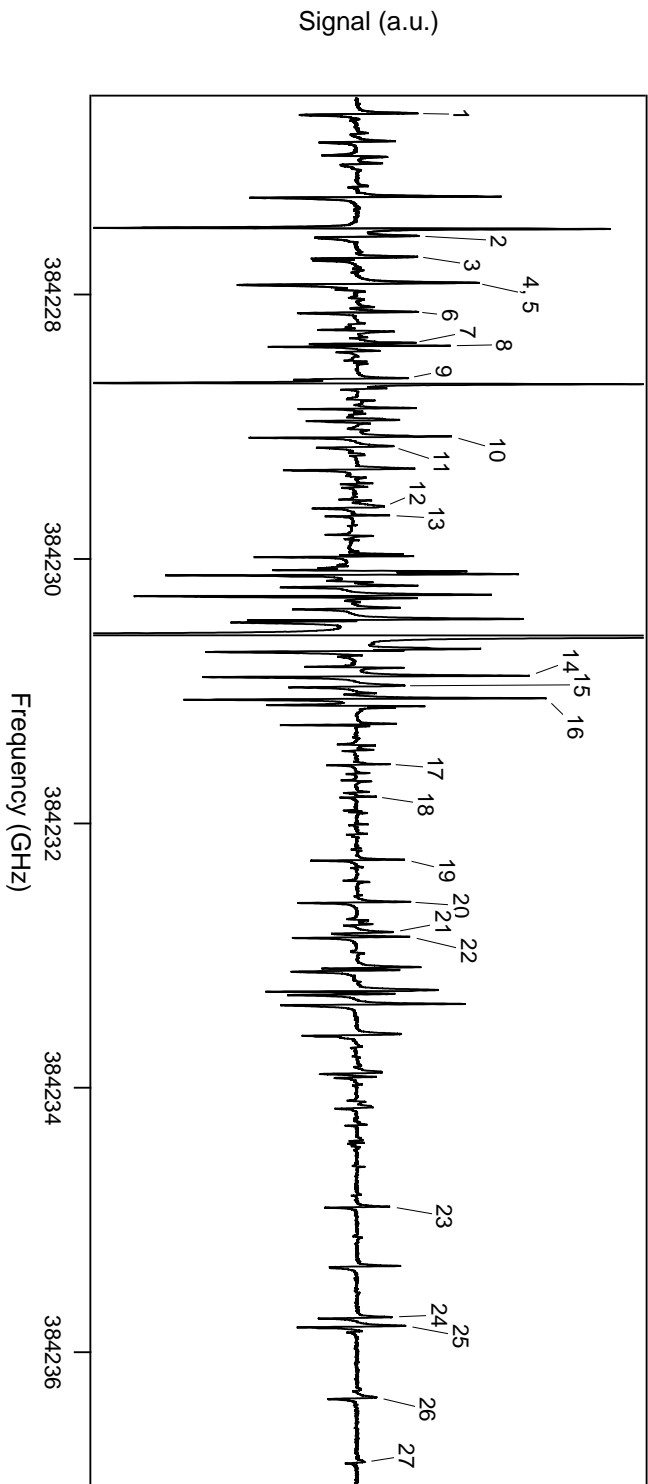


Figure A.4: Spectrum of D_2 line of rubidium in a magnetic field of about 0.057 T. Both beams are polarized perpendicular to the magnetic field direction. Legend in Table A.4.

Appendix B

D_1 spectra in static fields

In this Appendix we report D_1 rubidium spectra obtained using two different Halbach cylinders (one providing about 0.126 T and the other about 0.057 T) for both polarizations (π for the light polarization parallel to the magnetic field direction and σ for the light polarization perpendicular to the magnetic field). The resonances appearing in the spectra are labeled with a number; a table accompanying each spectrum gives the transitions corresponding to the labeled resonances. The lower level of the transition is indicated via the quantum numbers $|F, m_F\rangle$ while the upper levels are denoted by the quantum numbers $|m_J, m_I\rangle$.

Table B.1: Information about the resonances appearing in the spectrum of Figure B.1; resonances are numbered as in the spectrum. The isotope, the lower and upper levels of the transition are reported.

Number	Isotope	Lower state	Upper state
1	^{87}Rb	$ 2, 1\rangle$	$ -1/2, 3/2\rangle$
2	^{87}Rb	$ 2, 0\rangle$	$ -1/2, 1/2\rangle$
3	^{85}Rb	$ 3, 2\rangle$	$ -1/2, 5/2\rangle$
4	^{87}Rb	$ 2, 2\rangle$	$ 1/2, 3/2\rangle$
5	^{85}Rb	$ 3, 1\rangle$	$ -1/2, 3/2\rangle$
6	^{87}Rb	$ 2, 1\rangle$	$ 1/2, 1/2\rangle$
7	^{85}Rb	$ 3, 0\rangle$	$ -1/2, 1/2\rangle$
8	^{87}Rb	$ 2, -1\rangle$	$ -1/2, -1/2\rangle$
9	^{85}Rb	$ 3, 3\rangle$	$ 1/2, 5/2\rangle$
10	^{87}Rb	$ 2, 0\rangle$	$ 1/2, -1/2\rangle$
11	^{85}Rb	$ 3, -1\rangle$	$ -1/2, -1/2\rangle$
12	^{85}Rb	$ 3, 2\rangle$	$ 1/2, 3/2\rangle$
13	^{85}Rb	$ 3, 1\rangle$	$ 1/2, 1/2\rangle$
14	^{85}Rb	$ 3, -2\rangle$	$ -1/2, -3/2\rangle$
15	^{85}Rb	$ 3, 0\rangle$	$ 1/2, -1/2\rangle$
16	^{85}Rb	$ 3, -1\rangle$	$ 1/2, -3/2\rangle$
17	^{87}Rb	$ 2, -2\rangle$	$ -1/2, -3/2\rangle$
18	^{85}Rb	$ 3, -2\rangle$	$ 1/2, -5/2\rangle$
19	^{85}Rb	$ 3, -3\rangle$	$ -1/2, -5/2\rangle$
20	^{85}Rb	$ 2, -2\rangle$	$ -1/2, -3/2\rangle$
21	^{85}Rb	$ 2, -1\rangle$	$ -1/2, -1/2\rangle$
22	^{85}Rb	$ 2, 0\rangle$	$ -1/2, 1/2\rangle$
23	^{85}Rb	$ 2, -2\rangle$	$ 1/2, -5/2\rangle$
24	^{85}Rb	$ 2, 1\rangle$	$ -1/2, 3/2\rangle$
25	^{85}Rb	$ 2, 2\rangle$	$ -1/2, 5/2\rangle$
26	^{85}Rb	$ 2, -1\rangle$	$ 1/2, -3/2\rangle$
27	^{85}Rb	$ 2, 0\rangle$	$ 1/2, -1/2\rangle$
28	^{87}Rb	$ 1, -1\rangle$	$ -1/2, -1/2\rangle$
29	^{85}Rb	$ 2, 1\rangle$	$ 1/2, 1/2\rangle$

Number	Isotope	Lower state	Upper state
30	^{87}Rb	$ 1, 0\rangle$	$ -1/2, 1/2\rangle$
31	^{85}Rb	$ 2, 2\rangle$	$ 1/2, 3/2\rangle$
32	^{87}Rb	$ 1, -1\rangle$	$ 1/2, -3/2\rangle$
33	^{87}Rb	$ 1, 1\rangle$	$ -1/2, 3/2\rangle$
34	^{87}Rb	$ 1, 0\rangle$	$ 1/2, -1/2\rangle$
35	^{87}Rb	$ 1, 1\rangle$	$ 1/2, 1/2\rangle$

Table B.2: Information about the resonances appearing in the spectrum of Figure B.2; resonances are numbered as in the spectrum. The isotope, the lower and upper levels of the transition are reported.

Number	Isotope	Lower state	Upper state
1	^{87}Rb	$ 2, 2\rangle$	$ -1/2, 3/2\rangle$
2	^{87}Rb	$ 2, 1\rangle$	$ -1/2, 1/2\rangle$
3	^{85}Rb	$ 3, 3\rangle$	$ -1/2, 5/2\rangle$
4	^{87}Rb	$ 2, 0\rangle$	$ -1/2, -1/2\rangle$
5	^{85}Rb	$ 3, 2\rangle$	$ -1/2, 3/2\rangle$
6	^{85}Rb	$ 3, 1\rangle$	$ -1/2, 1/2\rangle$
7	^{85}Rb	$ 3, 0\rangle$	$ -1/2, -1/2\rangle$
8	^{87}Rb	$ 2, -1\rangle$	$ -1/2, -3/2\rangle$
9	^{85}Rb	$ 3, -1\rangle$	$ -1/2, -3/2\rangle$
10	^{85}Rb	$ 3, -2\rangle$	$ -1/2, -5/2\rangle$
11	^{85}Rb	$ 3, -1\rangle$	$ 1/2, -1/2\rangle$
12	^{85}Rb	$ 3, -2\rangle$	$ 1/2, -3/2\rangle$
13	^{87}Rb	$ 2, -2\rangle$	$ 1/2, -3/2\rangle$
14	^{85}Rb	$ 3, -3\rangle$	$ 1/2, -5/2\rangle$
15	^{85}Rb	$ 2, -2\rangle$	$ -1/2, -5/2\rangle$
16	^{85}Rb	$ 2, -1\rangle$	$ -1/2, -3/2\rangle$
17	^{85}Rb	$ 2, 0\rangle$	$ -1/2, -1/2\rangle$
18	^{85}Rb	$ 2, -2\rangle$	$ 1/2, -3/2\rangle$
19	^{85}Rb	$ 2, 1\rangle$	$ -1/2, 1/2\rangle$
20	^{85}Rb	$ 2, -1\rangle$	$ 1/2, -1/2\rangle$
21	^{85}Rb	$ 2, 0\rangle$	$ 1/2, 1/2\rangle$
22	^{87}Rb	$ 1, -1\rangle$	$ -1/2, -3/2\rangle$

Number	Isotope	Lower state	Upper state
23	^{85}Rb	$ 2, 1\rangle$	$ 1/2, 3/2\rangle$
24	^{85}Rb	$ 2, 2\rangle$	$ 1/2, 5/2\rangle$
25	^{87}Rb	$ 1, 0\rangle$	$ -1/2, -1/2\rangle$
26	^{87}Rb	$ 1, -1\rangle$	$ 1/2, -1/2\rangle$
27	^{87}Rb	$ 1, 1\rangle$	$ -1/2, 1/2\rangle$
28	^{87}Rb	$ 1, 0\rangle$	$ 1/2, -3/2\rangle$
29	^{87}Rb	$ 1, 0\rangle$	$ 1/2, 1/2\rangle$
30	^{87}Rb	$ 1, 1\rangle$	$ 1/2, -1/2\rangle$
31	^{87}Rb	$ 1, 1\rangle$	$ 1/2, 3/2\rangle$

Table B.3: Information about the resonances appearing in the spectrum of Figure B.3; resonances are numbered as in the spectrum. The isotope, the lower and upper levels of the transition are reported.

Number	Isotope	Lower state	Upper state
1	^{87}Rb	$ 2, 1\rangle$	$ -1/2, 3/2\rangle$
2	^{87}Rb	$ 2, 0\rangle$	$ -1/2, 1/2\rangle$
3	^{87}Rb	$ 2, 2\rangle$	$ 1/2, 3/2\rangle$
4	^{87}Rb	$ 2, -1\rangle$	$ -1/2, -1/2\rangle$
5	^{85}Rb	$ 3, 1\rangle$	$ -1/2, 3/2\rangle$
6	^{85}Rb	$ 3, 0\rangle$	$ -1/2, 1/2\rangle$
7	^{85}Rb	$ 3, -2\rangle$	$ 1/2, -5/2\rangle$
8	^{85}Rb	$ 3, -3\rangle$	$ -1/2, -5/2\rangle$
9	^{85}Rb	$ 2, -2\rangle$	$ -1/2, -3/2\rangle$
10	^{85}Rb	$ 2, 1\rangle$	$ -1/2, 3/2\rangle$
11	^{85}Rb	$ 2, 2\rangle$	$ -1/2, 5/2\rangle$
12	^{85}Rb	$ 2, -1\rangle$	$ 1/2, -3/2\rangle$
13	^{85}Rb	$ 2, 0\rangle$	$ 1/2, -1/2\rangle$
14	^{85}Rb	$ 2, 1\rangle$	$ 1/2, 1/2\rangle$
15	^{85}Rb	$ 2, 2\rangle$	$ 1/2, 3/2\rangle$
16	^{87}Rb	$ 1, 0\rangle$	$ -1/2, 1/2\rangle$
17	^{87}Rb	$ 1, 1\rangle$	$ -1/2, 3/2\rangle$
18	^{87}Rb	$ 1, -1\rangle$	$ 1/2, -3/2\rangle$
19	^{87}Rb	$ 1, 0\rangle$	$ 1/2, -1/2\rangle$

Number	Isotope	Lower state	Upper state
20	^{87}Rb	$ 1, 1\rangle$	$ 1/2, 1/2\rangle$

Table B.4: Information about the resonances appearing in the spectrum of Figure B.4; resonances are numbered as in the spectrum. The isotope, the lower and upper levels of the transition are reported.

Number	Isotope	Lower state	Upper state
1	^{87}Rb	$ 2, 2\rangle$	$ - 1/2, 3/2\rangle$
2	^{87}Rb	$ 2, 1\rangle$	$ - 1/2, 1/2\rangle$
3	^{85}Rb	$ 3, 3\rangle$	$ - 1/2, 5/2\rangle$
4	^{85}Rb	$ 3, 2\rangle$	$ - 1/2, 3/2\rangle$
5	^{85}Rb	$ 3, 1\rangle$	$ - 1/2, 1/2\rangle$
6	^{85}Rb	$ 3, 0\rangle$	$ - 1/2, -1/2\rangle$
7	^{85}Rb	$ 3, -3\rangle$	$ - 1/2, -3/2\rangle$
8	^{85}Rb	$ 3, -2\rangle$	$ 1/2, -3/2\rangle$
9	^{85}Rb	$ 3, -3\rangle$	$ 1/2, -5/2\rangle$
10	^{85}Rb	$ 2, -2\rangle$	$ - 1/2, -1/2\rangle$
11	^{85}Rb	$ 2, 0\rangle$	$ 1/2, 1/2\rangle$
12	^{85}Rb	$ 2, 1\rangle$	$ 1/2, 3/2\rangle$
13	^{85}Rb	$ 2, 2\rangle$	$ 1/2, 5/2\rangle$
14	^{87}Rb	$ 1, -1\rangle$	$ - 1/2, 1/2\rangle$
15	^{87}Rb	$ 1, -1\rangle$	$ - 1/2, -3/2\rangle$
16	^{87}Rb	$ 1, -1\rangle$	$ 1/2, -1/2\rangle$
17	^{87}Rb	$ 1, 0\rangle$	$ 1/2, -3/2\rangle$
18	^{87}Rb	$ 1, 0\rangle$	$ 1/2, 1/2\rangle$
19	^{87}Rb	$ 1, 1\rangle$	$ 1/2, -1/2\rangle$
20	^{87}Rb	$ 1, 1\rangle$	$ 1/2, 3/2\rangle$

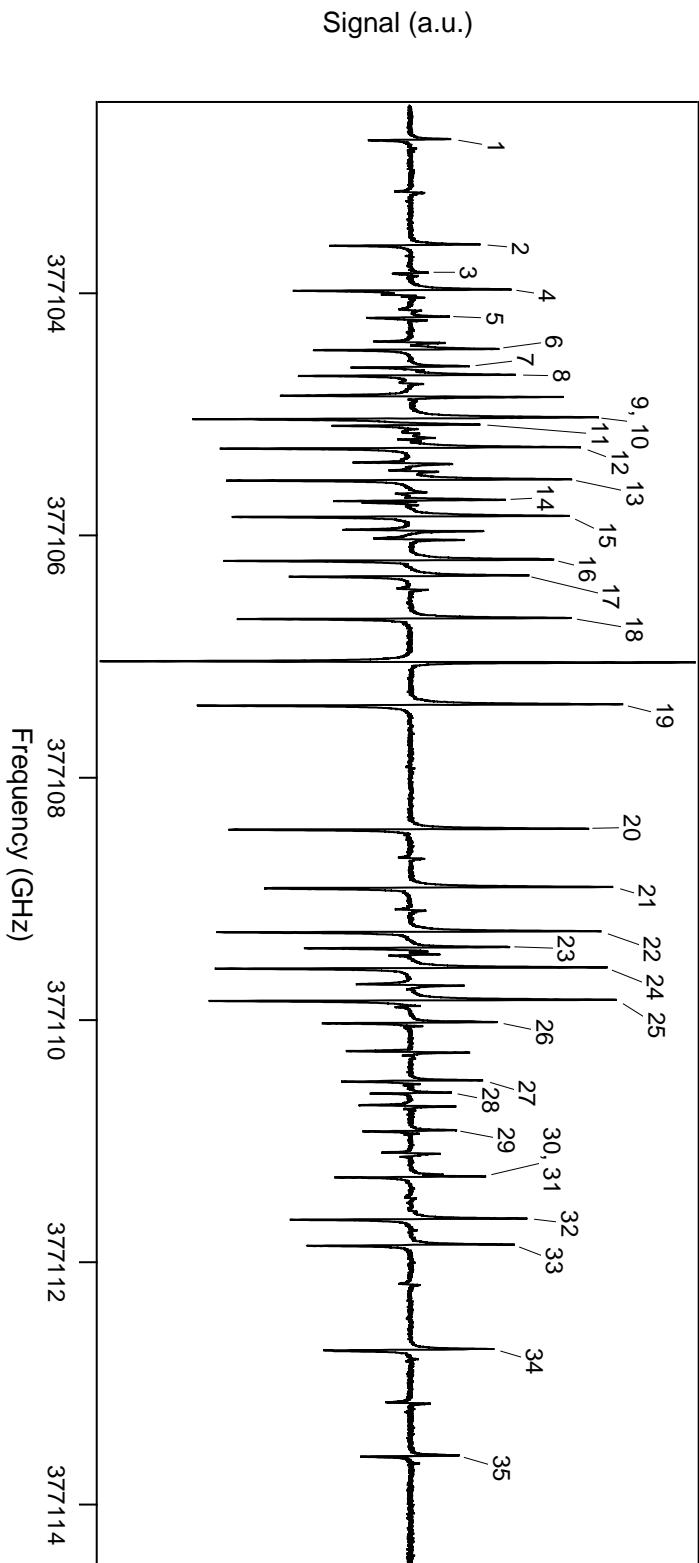


Figure B.1: Spectrum of D_1 line of rubidium in a magnetic field of about 0.126 T. Both beams are polarized parallel to the magnetic field direction. Legend in Table B.1.

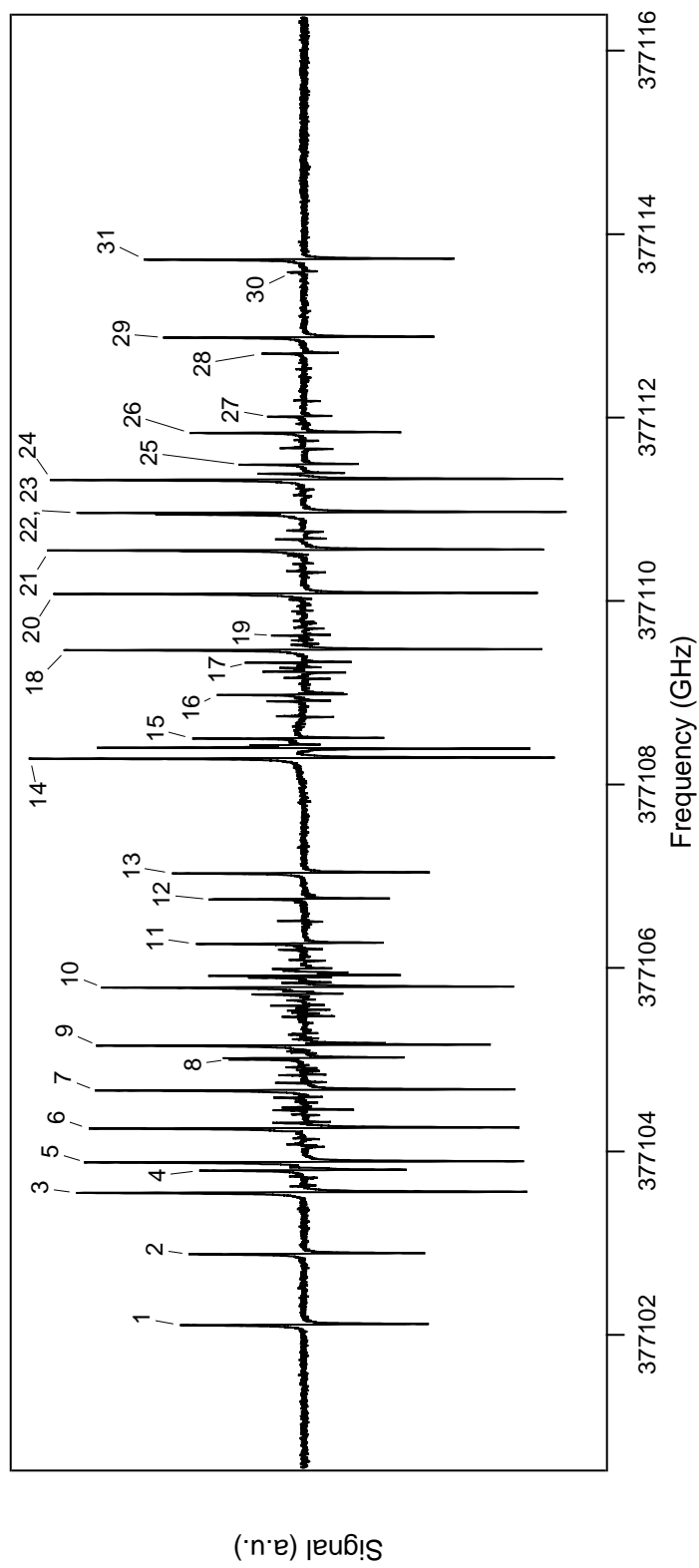


Figure B.2: Spectrum of D_1 line of rubidium in a magnetic field of about 0.126 T. Both beams are polarized perpendicular to the magnetic field direction. Legend in Table B.2.

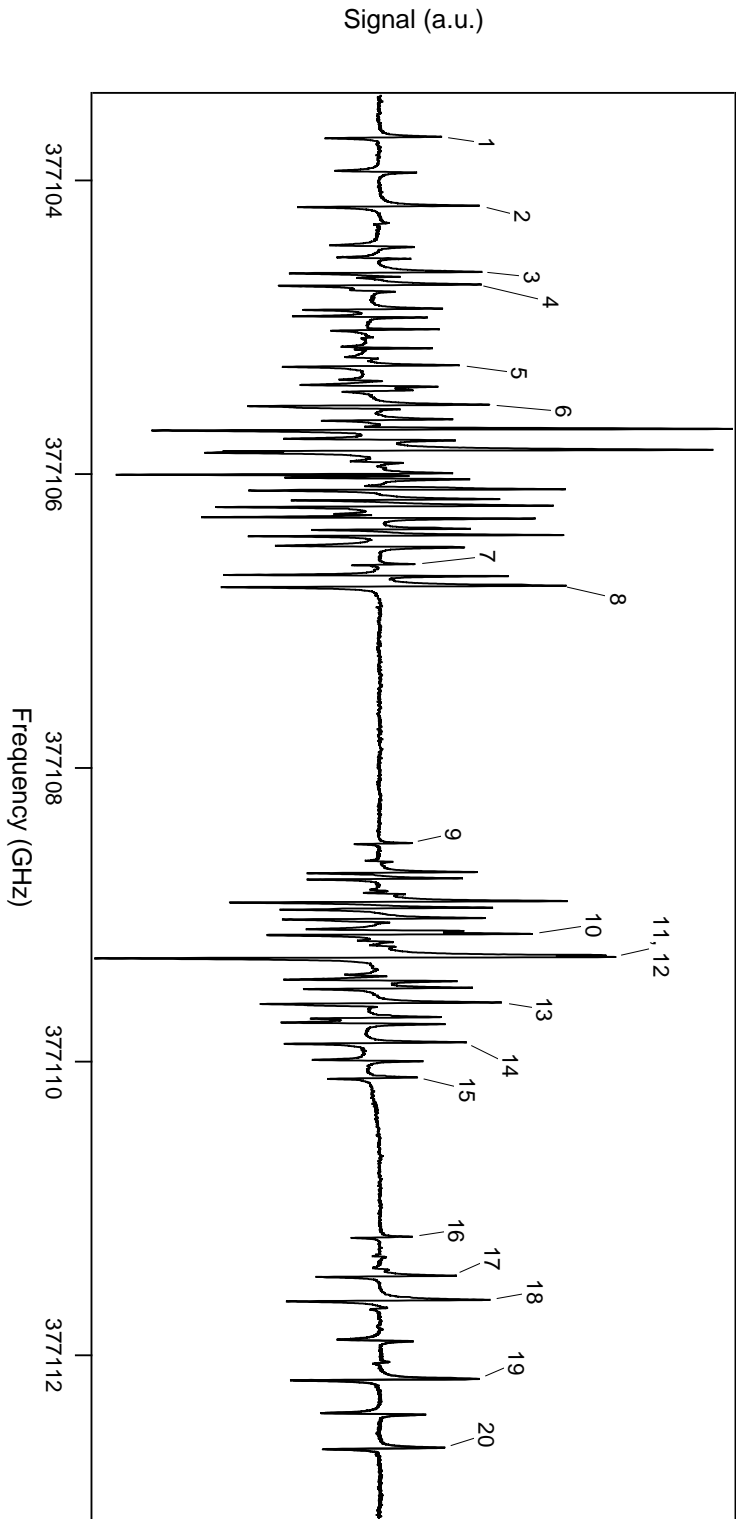


Figure B.3: Spectrum of D_1 line of rubidium in a magnetic field of about 0.057 T. Both beams are polarized parallel to the magnetic field direction. Legend in Table B.3.

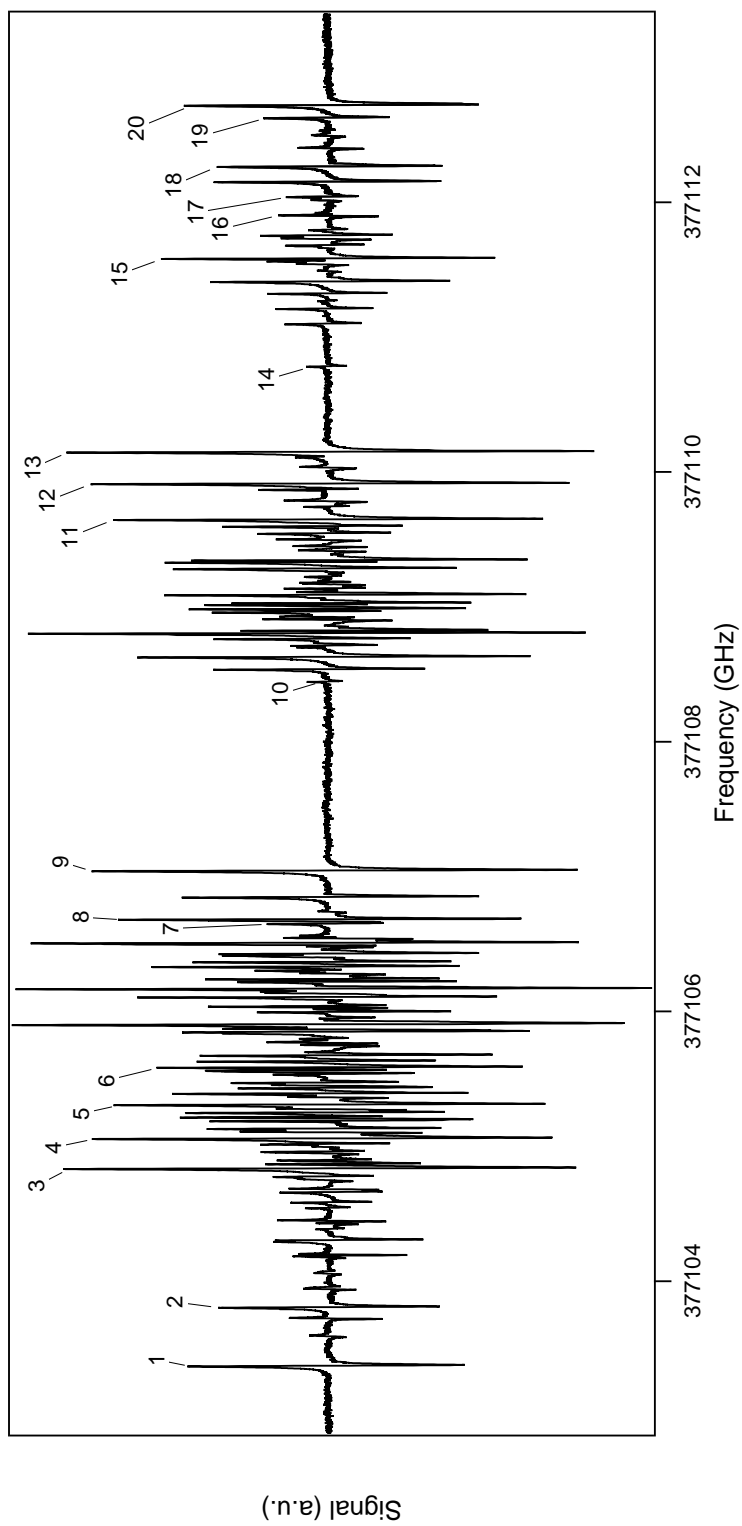


Figure B.4: Spectrum of D_1 line of rubidium in a magnetic field of about 0.057 T. Both beams are polarized perpendicular to the magnetic field direction. Legend in Table B.4.

Appendix C

Résumé de la thèse en français

Dans cette annexe nous présentons un résumé en français de ce travail de thèse. Le lecteur ne trouvera aucune nouvelle information et les figures utilisées sont les mêmes que dans la version anglaise.

C.1 Métrologie pour les champs magnétiques

Le premier chapitre énumère les techniques disponibles pour la mesure des champs magnétiques, plus précisément les techniques qui permettant de mesurer les champs magnétiques dans l'intervalle entre 0.1 T et quelques dizaines de teslas. Le choix de la meilleure méthode à utiliser pour une application donnée doit être réalisé en tenant compte de plusieurs paramètres comme:

- l'intervalle de mesure souhaité
- la résolution de l'instrument de mesure
- l'exactitude de la mesure
- l'échelle temporelle des variations du champ (bande passante de l'instrument)
- le volume de mesure

Le schéma en Figure C.1 propose une vue d'ensemble des techniques les plus communes avec, pour chaque technique, l'indication de l'intervalle de champ magnétique pouvant être mesuré et l'exactitude pouvant être atteinte.

Les techniques principales que l'on retrouve dans l'intervalle qui nous intéresse (0.1 T - \sim 50 T) sont la résonance magnétique nucléaire (RMN), l'effet Hall classique et les fluxmètres.

La mesure du champ par résonance magnétique nucléaire repose sur la mesure de la fréquence de transition entre deux niveaux quantiques du proton: lorsqu'un proton est soumis à un champ magnétique, ses deux états de spin se séparent en énergie, l'écart en énergie étant proportionnel à la valeur du champ. Le lien entre la valeur du champ magnétique et la fréquence de résonance observée est fait par le rapport gyromagnétique γ :

$$\nu = \gamma B \tag{C.1}$$

L'exactitude de cette technique (incertitude relative typique $\sim 10^{-6}$) vient du fait que la valeur de γ pour le proton dans l'eau est parfaitement connue. C'est pour cette raison que les mesures de champ réalisées par RMN sont

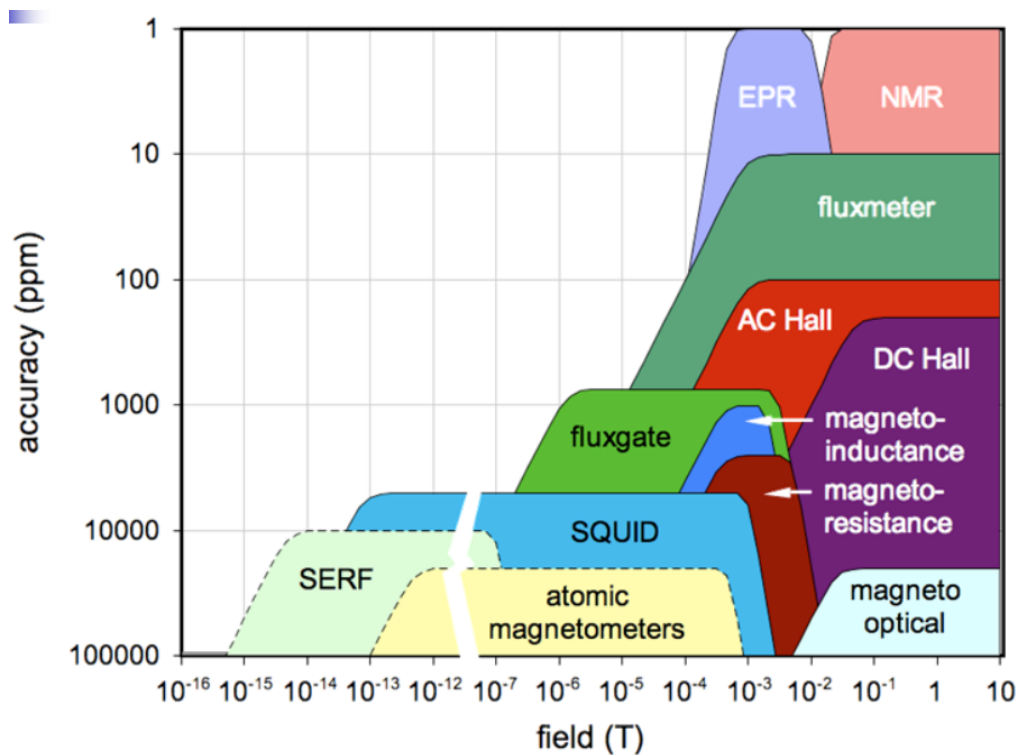


Figure C.1: Schéma des techniques de mesure des champs magnétiques, classée selon l'intervalle de mesure et l'exactitude des techniques. (Tiré d'une présentation de Luca Bottura - CERN [7])

en général utilisées pour la calibration des autres instruments de mesure du champ magnétique.

L'intervalle typique des champs magnétiques pouvant être explorés avec des instruments RMN commerciaux varie entre 0.1 T et $\simeq 20$ T, mais leur bande passante est limitée à quelques hertz. Des mesures plus rapides peuvent être effectuées avec des fluxmètres ou des sondes à effet Hall.

Le principe de fonctionnement d'un fluxmètre repose sur la loi de l'induction électromagnétique: lorsqu'une bobine est placée dans un champ magnétique variable, une tension V est générée, proportionnelle à la dérivée temporelle du flux magnétique ϕ :

$$V = -\frac{d\phi}{dt} \quad (\text{C.2})$$

La mesure puis l'intégration de la tension V , sur une bobine préalablement calibrée (via la comparaison avec une mesure de RMN par exemple) donne la

valeur du champ magnétique. Dans le cas de champs statiques, la variation du flux peut être produite par un mouvement contrôlé de la bobine (par exemple une rotation). L'intervalle de champ magnétique pouvant être mesuré avec cette méthode s'étend sur des valeurs allant d'environ $0.1 \mu\text{T}$ jusqu'à des valeurs très élevés, sans des limites de nature fondamentale. L'incertitude des mesures est liée à la procédure de calibration et à l'erreur due à la mesure de tension. Les valeurs typiques de l'incertitude relative pouvant être atteintes sont aux alentours de 100 ppm.

Le principe des sondes à effet Hall repose sur la tension générée aux bords d'une plaquette conductrice (ou semiconductrice) lorsqu'elle traversée par un courant électrique en présence d'un champ magnétique perpendiculaire à la surface de la plaquette. La valeur de la tension mesurée est en correspondance avec la valeur du champ magnétique. Les dispositifs commerciaux peuvent atteindre une erreur relative de 1000 ppm avec une bande passante de 500 kHz.

Aucune des techniques décrites n'est adaptée à la mesure des champs pulsés; au cours de ce travail de thèse nous avons développé une méthode utilisant des atomes de rubidium afin de mesurer les champs magnétiques pulsés produits au Laboratoire National des Champs Magnétiques Intenses de Toulouse.

C.2 Spectres des atomes alcalins sous champ magnétique

Le deuxième chapitre est consacré à la description théorique de l'interaction entre les atomes de rubidium avec le champ magnétique.

Le rubidium est un métal alcalin de numéro atomique $Z = 37$. Il possède deux isotopes naturels: le ^{85}Rb et le ^{87}Rb . La structure des niveaux d'énergie sans champ magnétique est décrite par un Hamiltonien comprenant plusieurs termes:

- l'énergie cinétique des électrons
- l'interaction électrostatique électron-noyau et électron-électron

- les corrections relativistes produisant le couplage spin-orbite
- l'interaction magnétique entre le noyau et les électrons

La prise en compte de toutes ces contributions permet d'expliquer la structure des niveaux qui est représentée en Figure C.2 pour le ^{85}Rb . Une structure similaire peut être obtenue pour l'isotope ^{87}Rb .

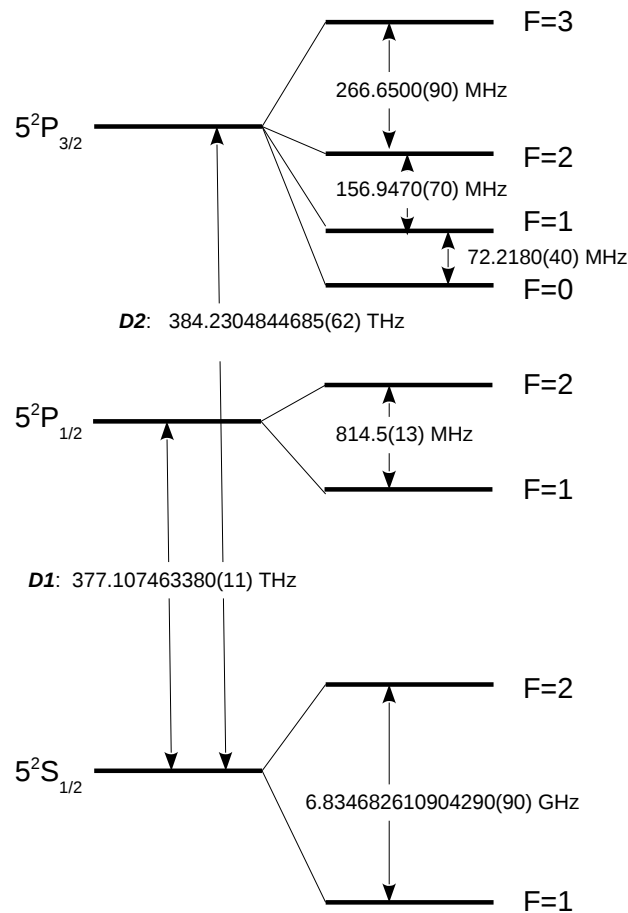


Figure C.2: Structure des niveaux d'énergie des raies D du ^{87}Rb . À gauche les niveaux de structure fine $5^2S_{1/2}$, $5^2P_{1/2}$ et $5^2P_{3/2}$. À droite les états hyperfins classés selon leurs moments angulaires totaux F .

En présence d'un champ magnétique appliqué, l'Hamiltonien est modifié par l'ajout d'un terme d'interaction entre le moment de dipôle magnétique

de l'atome et le champ magnétique:

$$\mathcal{H}_{int} = \boldsymbol{\mu} \cdot \mathbf{B} \quad (\text{C.3})$$

Le moment dipolaire de l'atome peut être exprimé en fonction du moments angulaire orbital L , de spin électronique S et de spin nucléaire I , en introduisant les facteurs de Landé $g_{L,S,I}$:

$$\mathcal{H}_{int} = \mu_B(g_L \mathbf{L} + g_e \mathbf{S} + g_I \mathbf{I}) \cdot \mathbf{B} \quad (\text{C.4})$$

Nous avons développé des codes numériques pour résoudre l'Hamiltonien, en particulier calculer les énergies des niveaux atomiques en fonction de la valeur du champ magnétique et l'intensité des transitions optiques. L'évolution des niveaux d'énergie du multiplet $5P_{3/2}$ est montrée Figure C.3. Deux régimes différents peuvent être distingués: pour des champs faibles la classification des niveaux se fait avec le moment angulaire totale F et sa projection m_F (régime Zeeman), pour des champs plus importants (lorsque le déplacement des niveaux causé par le champ est plus grand que la séparation hyperfine) les états quantiques doivent être classifiés en utilisant la projection du moment angulaire total électronique m_J (régime Paschen-Back hyperfin).

C.3 Techniques expérimentales: spectroscopie laser

Le troisième chapitre présente les techniques de spectroscopie laser que nous avons utilisé au cours ce travail de thèse. La technique la plus simple est l'absorption linéaire (spectroscopie Doppler): un faisceau laser traverse la vapeur atomique et, à la sortie, la fraction de la puissance lumineuse absorbée par le milieu atomique est mesurée. Dû au mouvement thermique, chaque atome "voit" une fréquence différente (effet Doppler), ce qui engendre un élargissement des raies atomiques. La largeur Doppler des raies D_1 et D_2 du rubidium vaut $\Delta_D \simeq 500$ MHz, alors que la largeur naturelle des raies (produite par émission spontanée) est de 6 MHz. De par sa simplicité, cette technique se révèle être utile dans le cas de la spectroscopie en

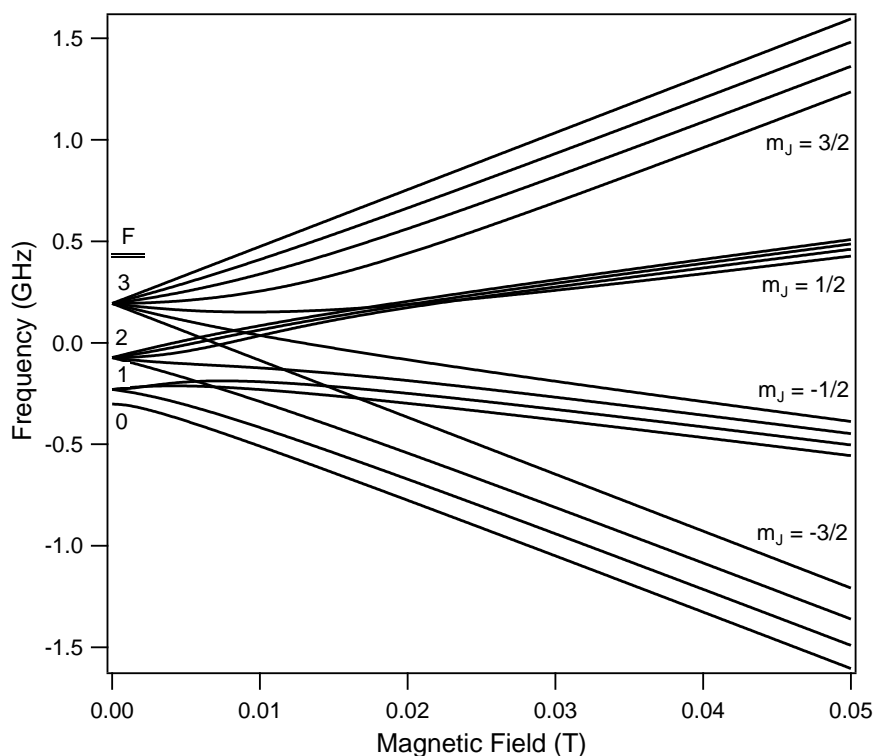


Figure C.3: Diagramme des niveaux d'énergie de l'état $5^2P_{3/2}$ du ^{87}Rb . Le diagramme montre l'évolution du système du régime Zeeman vers le régime Paschen-Back hyperfin.

champ intense puisque, dans ce régime, les résonances sont suffisamment séparées pour pouvoir être résolues. Dans le régime de champs intermédiaires, lorsque l'atome n'est plus en régime Zeeman, mais n'a pas encore atteint le régime Paschen-Back, beaucoup de raies d'absorption sont présentes dû à la rupture des règles de sélection. La spectroscopie Doppler ne permet pas de résoudre les raies atomiques trop proches. Nous avons alors utilisé la technique de l'absorption saturée qui consiste à envoyer dans la vapeur deux faisceaux laser contrepropageants. Nous avons étudié en détails la dynamique du pompage optique en mettant en évidence les effets observables sur les spectres: modification de l'intensité des raies atomiques, résonance de croisement à trois et quatre niveaux. La comparaison avec les données expérimentales est présentée dans le cinquième chapitre.

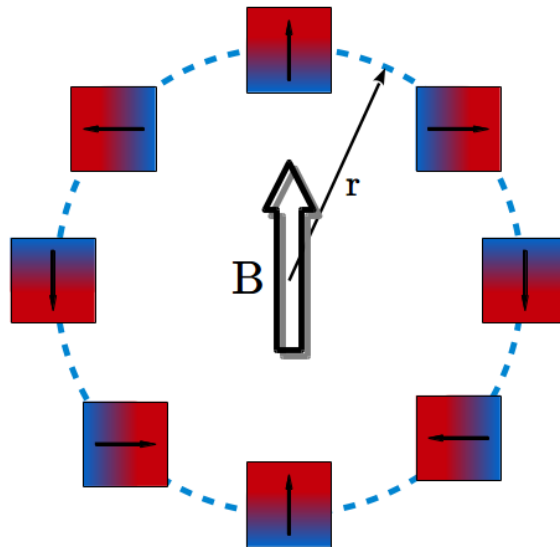


Figure C.4: Schéma d'un cylindre de Halbach réalisé avec 8 barres magnétiques. Les flèches indiquent l'orientation du vecteur aimantation de chaque barre.

C.4 Techniques expérimentales: production du champ magnétique

Le quatrième chapitre est consacré à la présentation des techniques que nous avons utilisé pour générer des champs magnétiques. Pour la production des champs statiques dans l'intervalle 0.05 T - 0.2 T, nous avons réalisé des assemblages d'aimants permanents dits cylindres de Halbach. L'orientation du vecteur aimantation de chaque barre magnétique doit respecter un schéma précis, représenté en Figure C.4. Nous avons réalisé un code numérique afin de calculer le profil du champ magnétique produit par des cylindres de différentes tailles; un exemple est montré en Figure C.5 pour un cylindre de 148 mm de longueur et 40 mm de diamètre.

Pour les mesures en champ intense, nous avons utilisé les installations présentes au sein du Laboratoire National des Champs Magnétiques Intenses de Toulouse. Le champ est généré par un courant électrique circulant dans une bobine résistive; le courant est produit par la décharge d'un banc de

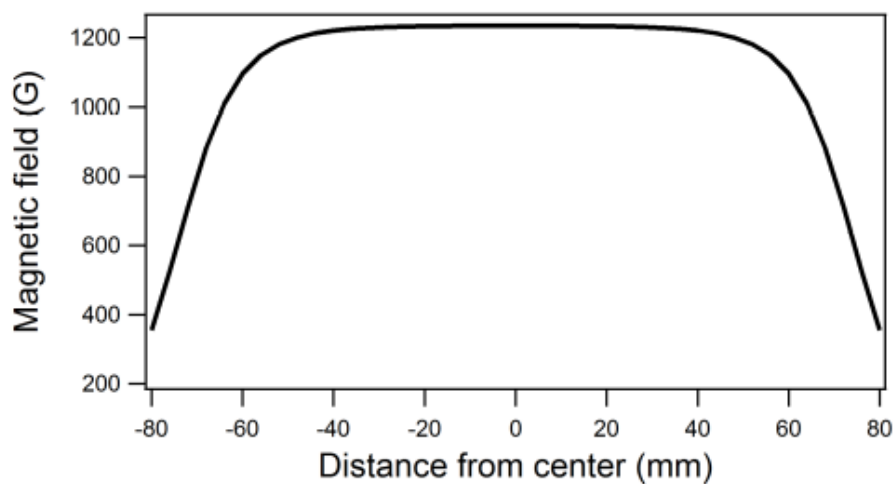


Figure C.5: Profil du champ magnétique dans la direction longitudinale.

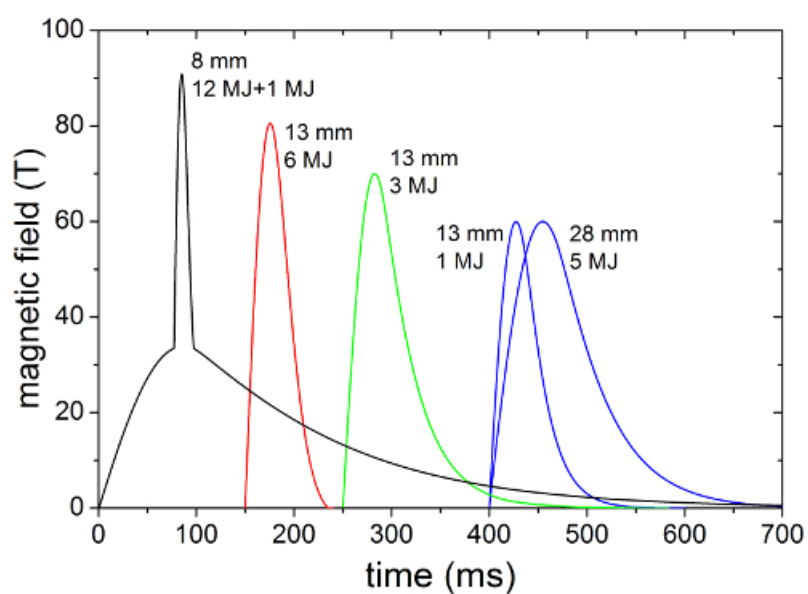


Figure C.6: Vue d'ensemble des bobines disponibles au LNCMI-T. Les profils temporels du champ magnétique, ainsi que l'énergie requise sont indiqués.

condensateurs. Plusieurs modèles de bobines sont disponibles, permettant de générer des champs magnétiques jusqu'à 90 T. Le schéma en Figure C.6 montre les différents profils temporels des champs magnétiques produits au laboratoire.

C.5 Spectres du rubidium sous champs magnétiques statiques

Le cinquième chapitre présente l'étude expérimentale des spectres d'absorption saturée du rubidium sous des champs statiques générés par des cylindres de Halbach. Après la description du montage expérimental, nous présentons nos résultats. Nous avons enregistré les spectres sub-Doppler du rubidium (Figure C.7) et, à l'aide des codes numériques servant à la simulation des spectres, nous avons identifié les transitions atomiques correspondantes à chaque raie. Les deux polarisations possibles des faisceaux laser (parallèle ou orthogonale au champ) ont été utilisées.

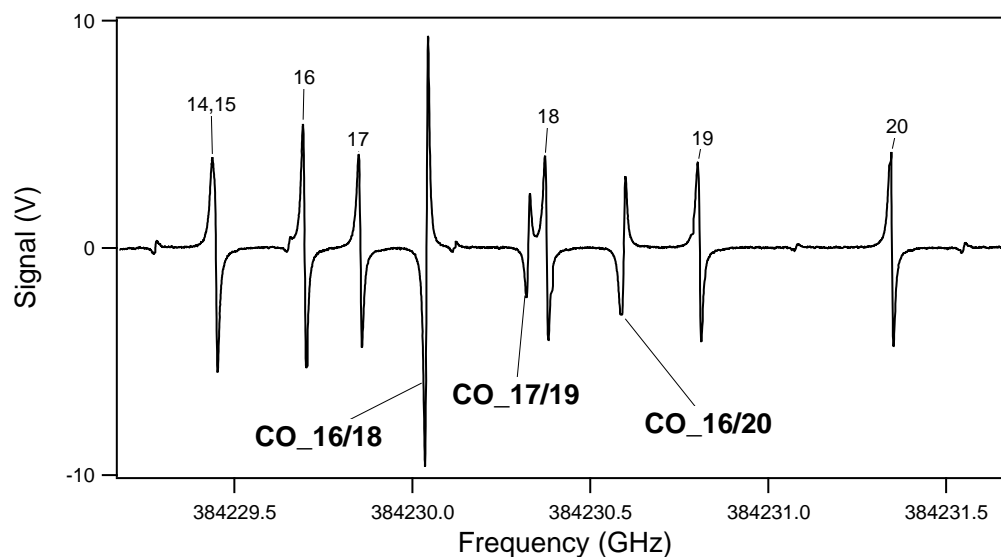


Figure C.7: Portion d'un spectre π en présence d'un champ magnétique de environ 0.126 T. Les transitions à deux niveaux sont numérotées (voir Table A.1 en Appendix A pour la légende). Les résonances de croisement inverties sont indiquées par l'étiquette CO_ n/n' .

La mesure des fréquences des transitions observées nous permet de déterminer la valeur du champs magnétique via la comparaison avec les résultats des nos simulations numériques.

Nous avons analysé l'amplitude relative des signaux observés et nous avons interprété ces dernières dans le cadre du modèle théorique décrit dans le troisième chapitre (Figure C.8).

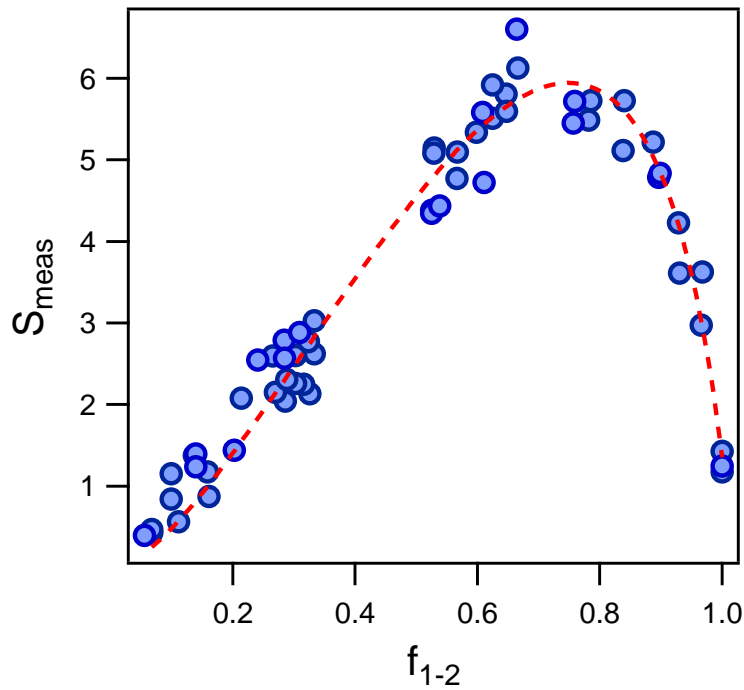


Figure C.8: Comparaison entre les intensités S_{meas} des signaux d'absorption saturée et les valeurs f_{g-e} calculées.

Nous avons aussi étudié les résonances de croisement, en comparant l'amplitude des signaux observés avec les prévisions du modèle théorique présenté dans le deuxième chapitre. La Figure C.8 montre le bon accord entre les valeurs expérimentales des amplitudes des signaux de croisement et les valeurs théoriques.

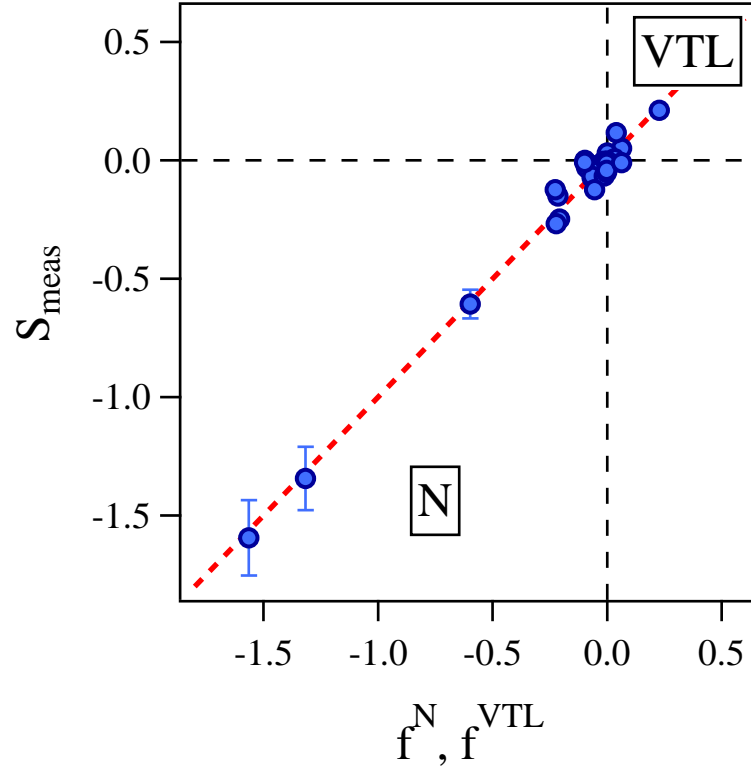


Figure C.9: Intensités mesurées S_{meas} des résonances de croisement à trois et quatre niveaux en fonction des valeurs théoriques f^{VTL} and f^N . Les données ont été obtenues de l'analyse d'un spectre σ à 0.072 T.

C.6 Métrologie des champs magnétiques pulsés utilisant des atomes de rubidium

Le sixième chapitre est consacré à la présentation des mesures de champ magnétique avec le rubidium. Dans le chapitre précédent nous avons montré comment obtenir la valeur du champ magnétique des données spectroscopiques. Les expériences sous champ magnétique intense requièrent la miniaturisation du système expérimental. Pour cela, nous avons réalisé une tête fibrée pour réaliser les mesures de spectroscopie sur le rubidium; le schéma est illustré en Figure C.10. Une fibre optique mono-mode guide la lumière laser vers la cellule de rubidium; la lumière traverse un polariseur avant de rentrer dans la cellule; la lumière émise par fluorescence est recueillie perpendiculairement

à la direction du faisceau laser par une fibre multi-mode. La lumière transmise par le rubidium est également injectée dans une fibre multi-mode. Les composants optiques sont logés dans une structure imprimée en 3D. Du fil électrique est enroulé autour de la structure pour chauffer la cellule de rubidium. Une bobine de *pick-up* est aussi réalisée pour la mesure du profil temporel du champ magnétique.

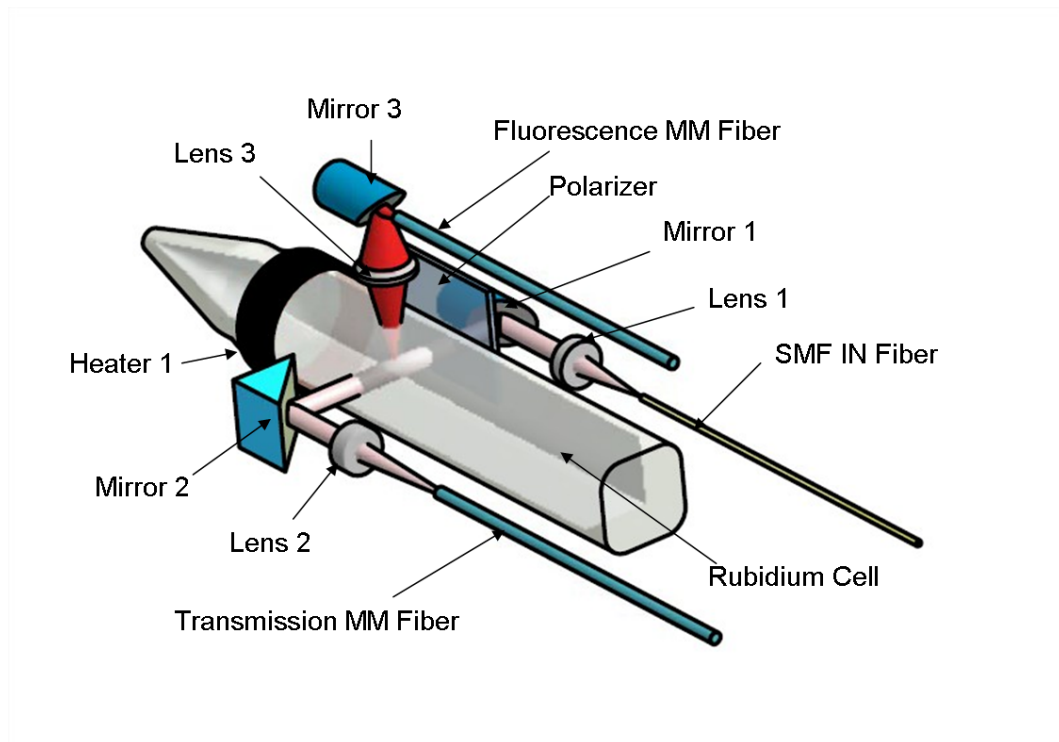


Figure C.10: Schéma optique du capteur.

Pendant un tir de champ magnétique, la fréquence est maintenue fixe. Le champ magnétique varie et des résonances apparaissent pour des valeurs précises de celui-ci. La connaissance de la fréquence du laser nous permet alors d'obtenir la valeur du champ magnétique. Les données représentées en Figure C.11 montrent les résonances de fluorescence observées. Ces données ont été obtenues avec une fréquence du laser de

$$\nu = 385042.737(6) \text{ GHz}$$

ce qui correspond à un champ magnétique de

$$B = 58.20(1)\text{T}$$

Nous avons effectué des tirs à différentes valeurs du champ magnétique et nous avons pu mesurer le rapport entre la valeur du champ donnée par la bobine *pick-up* et la valeur donnée par notre méthode:

$$\frac{B_{PU}}{B_{Rb}} = 0.9898(2)$$

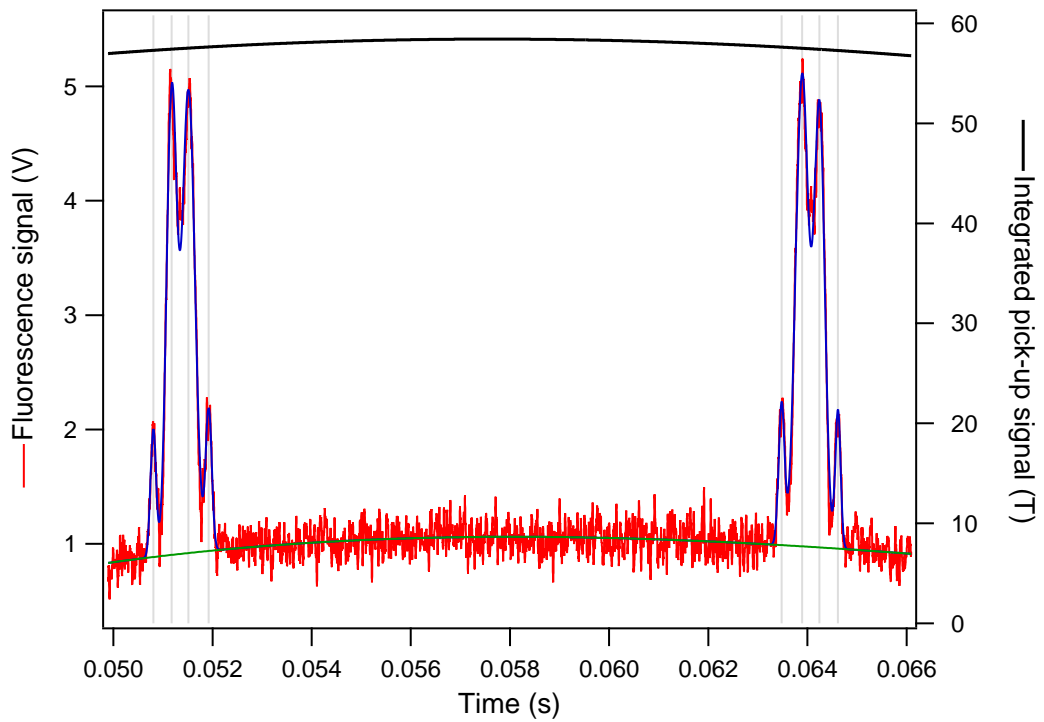


Figure C.11: Détail du spectre de fluorescence présenté en Figure 6.8.

Bibliography

- [1] CADÈNE, AGATHE, BERCEAU, PAUL, FOUCHÉ, MATHILDE, BATTISTI, RÉMY, ET RIZZO, CARLO, “Vacuum magnetic linear birefringence using pulsed fields: status of the BMV experiment”, *Eur. Phys. J. D* **68**, 16 (2014).
- [2] E. ARIMONDO, D. CIAMPINI, ET C. RIZZO, dans *Chapter One - Spectroscopy of Natural and Artificial Atoms in Magnetic Fields*, Vol. 65 de *Advances In Atomic, Molecular, and Optical Physics*, (Academic Press, 2016), pp. 1 – 66.
- [3] L. LABZOWSKY, I. GOIDENKO, ET P. PYYKKÖ, “Estimates of the bound-state {QED} contributions to the g-factor of valence ns electrons in alkali metal atoms”, *Physics Letters A* **258**, 31 (1999).
- [4] *Procès-Verbaux des Séances du CIPM (1946)* 129 .
- [5] J. L. SYMONDS, “Methods of Measuring Strong Magnetic Fields”, *Reports on Progress in Physics* **18**, 83 (1955).
- [6] D. BUDKER ET D. KIMBALL, *Optical Magnetometry* (Cambridge University Press, 2013).
- [7] <http://cas.web.cern.ch/cas/Belgium-2009/Lectures/PDFs/Bottura-1.pdf>.
- [8] A. ABRAGAM, *The Principles of Nuclear Magnetism, International series of monographs on physics* (Clarendon Press, 1961).
- [9] www.metrolab.com.

-
- [10] W. D. PHILLIPS, W. E. COOKE, ET D. KLEPPNER, “Magnetic Moment of the Proton in H₂O in Bohr Magnetons”, *Metrologia* **13**, 179 (1977).
- [11] P. J. MOHR, B. N. TAYLOR, ET D. B. NEWELL, “CODATA Recommended Values of the Fundamental Physical constants: 2014”, .
- [12] L. BOTTURA ET K. N. HENRICHSEN, *in Proceedings of the CAS-CERN Accelerator School: Superconductivity and cryogenics for accelerators and detectors, Erice, Italy, 8-17 May 2002, edited by R. Russenschuck and G. Vandoni, CERN-2004-008* 357 .
- [13] H. STORK, P. BONTEMPS, ET G. RIKKEN, “{NMR} in pulsed high-field magnets and application to high-TC superconductors”, *Journal of Magnetic Resonance* **234**, 30 (2013).
- [14] L. WALCKIERS, *in Proceedings of the CAS-CERN Accelerator School: Magnets, Bruges, Belgium, 16-25 June 2009, edited by D. Brandt, CERN-2010-004* 357 .
- [15] G. GROSSO ET G. PARRAVICINI, *Solid State Physics* (Elsevier Science, 2000).
- [16] <http://www.lakeshore.com/products/Gaussmeters/Pages/Gaussmeter-Models.aspx>.
- [17] S. KNAPPE, V. SHAH, P. D. D. SCHWINDT, L. HOLLBERG, J. KITCHING, L.-A. LIEW, ET J. MORELAND, “A microfabricated atomic clock”, *Applied Physics Letters* **85**, (2004).
- [18] C. FOOT, *Atomic physics, Oxford master series in physics* (Oxford University Press, 2005).
- [19] B. BRANSDEN ET C. JOACHAIN, *Physics of Atoms and Molecules, Pearson Education* (Prentice Hall, 2003).
- [20] K. KONISHI ET G. PAFFUTI, *Quantum Mechanics: A New Introduction* (OUP Oxford, 2009).

-
- [21] S. BIZE, Y. SORTAIS, M. S. SANTOS, C. MANDACHE, A. CLAIRON, ET C. SALOMON, “High-accuracy measurement of the 87 Rb ground-state hyperfine splitting in an atomic fountain”, *EPL (Europhysics Letters)* **45**, 558 (1999).
- [22] A. BANERJEE, D. DAS, ET V. NATARAJAN, “Absolute frequency measurements of the D 1 lines in 39 K, 85 Rb, and 87 Rb with 0.1 ppb uncertainty”, *EPL (Europhysics Letters)* **65**, 172 (2004).
- [23] J. YE, S. SWARTZ, P. JUNGNER, ET J. L. HALL, “Hyperfine structure and absolute frequency of the 87Rb 5P_{3/2} state”, *Opt. Lett.* **21**, 1280 (1996).
- [24] E. ARIMONDO, M. INGUSCIO, ET P. VIOLINO, “Experimental determinations of the hyperfine structure in the alkali atoms”, *Rev. Mod. Phys.* **49**, 31 (1977).
- [25] M. F. F.R.S., “XXVII. On the magnetic affection of light, and on the distinction between the ferromagnetic and diamagnetic conditions of matter”, *Philosophical Magazine Series 3* **29**, 153 (1846).
- [26] D. P. ZEEMAN, “XXXII. On the influence of magnetism on the nature of the light emitted by a substance”, *Philosophical Magazine Series 5* **43**, 226 (1897).
- [27] D. P. ZEEMAN, “VII. Doublets and triplets in the spectrum produced by external magnetic forces”, *Philosophical Magazine Series 5* **44**, 55 (1897).
- [28] A. J. KOX, “The discovery of the electron: II. The Zeeman effect”, *European Journal of Physics* **18**, 139 (1997).
- [29] P. J. MOHR, B. N. TAYLOR, ET D. B. NEWELL, “CODATA recommended values of the fundamental physical constants: 2010*”, *Rev. Mod. Phys.* **84**, 1527 (2012).
- [30] J. S. TIEDEMAN ET H. G. ROBINSON, “Determination of $\frac{g_J(^1H, 1^2S_{\frac{1}{2}})}{g_s(e)}$: Test of Mass-Independent Corrections”, *Phys. Rev. Lett.* **39**, 602 (1977).

- [31] <http://steck.us/alkalidata/rubidium87numbers.pdf>.
- [32] S. SVANBERG ET G. BELIN, “Determination of hyperfine structure and g_j factors in the sequences of $2D$ states in alkali atoms using a tunable dye laser”, *Journal of Physics B: Atomic and Molecular Physics* **7**, L82 (1974).
- [33] L. WELLER, K. S. KLEINBACH, M. A. ZENTILE, S. KNAPPE, C. S. ADAMS, ET I. G. HUGHES, “Absolute absorption and dispersion of a rubidium vapour in the hyperfine Paschen–Back regime”, *Journal of Physics B: Atomic, Molecular and Optical Physics* **45**, 215005 (2012).
- [34] A. SARGSYAN, G. HAKHUMYAN, C. LEROY, Y. PASHAYAN-LEROY, A. PAPOYAN, ET D. SARKISYAN, “Hyperfine Paschen–Back regime realized in Rb nanocell”, *Opt. Lett.* **37**, 1379 (2012).
- [35] H. HORI, M. MIKI, ET M. DATE, “Paschen-Back Effect of D-Lines in Sodium under a High Magnetic Field”, *Journal of the Physical Society of Japan* **51**, 1566 (1982).
- [36] F. A. JENKINS ET E. SEGRÈ, “The Quadratic Zeeman Effect”, *Phys. Rev.* **55**, 52 (1939).
- [37] P. OTTO, M. GAMPERLING, M. HOFACKER, T. MEYER, V. PAGLIARI, A. STIFTER, M. KRAUSS, ET W. HÜTTNER, “Level magnetizabilities of the alkaline metal atoms”, *Chemical Physics* **282**, 289 (2002).
- [38] W. HÜTTNER, P. OTTO, ET M. GAMPERLING, “Second-order Zeeman effect in the $5^2S - 3^2S$ and $4^2D - 3^2S$ two-photon transitions of atomic sodium”, *Phys. Rev. A* **54**, 1318 (1996).
- [39] W. DEMTRÖDER, *Laser Spectroscopy: Basic Concepts and Instrumentation, Advanced Texts in Physics* (Springer Berlin Heidelberg, 2002).
- [40] R. LOUDON, *The Quantum Theory of Light* (OUP Oxford, 2000).

-
- [41] G. GRYNBERG, A. ASPECT, C. FABRE, ET C. COHEN-TANNOUJDI, *Introduction to Quantum Optics: From the Semi-classical Approach to Quantized Light* (Cambridge University Press, 2010).
- [42] P. SIDONS, C. S. ADAMS, ET I. G. HUGHES, “Off-resonance absorption and dispersion in vapours of hot alkali-metal atoms”, *Journal of Physics B: Atomic, Molecular and Optical Physics* **42**, 175004 (2009).
- [43] C. B. ALCOCK, V. P. ITKIN, ET M. K. HARRIGAN, “Vapour Pressure Equations for the Metallic Elements: 298–2500K”, *Canadian Metallurgical Quarterly* **23**, 309 (1984).
- [44] W. NAGOURNEY, *Quantum Electronics for Atomic Physics and Telecommunication, Oxford graduate texts* (Oxford University Press, 2014).
- [45] G. C. BJORKLUND, M. D. LEVENSON, W. LENTH, ET C. ORTIZ, “Frequency modulation (FM) spectroscopy”, *Applied Physics B* **32**, 145 (1983).
- [46] E. JAATINEN, “Theoretical determination of maximum signal levels obtainable with modulation transfer spectroscopy”, *Optics Communications* **120**, 91 (1995).
- [47] J. H. SHIRLEY, “Modulation transfer processes in optical heterodyne saturation spectroscopy”, *Opt. Lett.* **7**, 537 (1982).
- [48] D. J. MCCARRON, S. A. KING, ET S. L. CORNISH, “Modulation transfer spectroscopy in atomic rubidium”, *Measurement Science and Technology* **19**, 105601 (2008).
- [49] S. NAKAYAMA, G. SERIES, ET W. GAWLIK, “Zeeman effect in the polarization spectroscopy of Na”, *Optics Communications* **34**, 382 (1980).
- [50] S. NAKAYAMA, “Optical pumping effects in high resolution laser spectroscopy”, *Physica Scripta* **1997**, 64 (1997).

- [51] P. G. PAPPAS, M. M. BURNS, D. D. HINSHELWOOD, M. S. FELD, ET D. E. MURNICK, “Saturation spectroscopy with laser optical pumping in atomic barium”, *Phys. Rev. A* **21**, 1955 (1980).
- [52] I. SYDORYK, N. N. BEZUGLOV, I. I. BETEROV, K. MICULIS, E. SAKS, A. JANOVŠ, P. SPELS, ET A. EKKERS, “Broadening and intensity redistribution in the Na(3p) hyperfine excitation spectra due to optical pumping in the weak excitation limit”, *Phys. Rev. A* **77**, 042511 (2008).
- [53] S. SCOTTO, D. CIAMPINI, C. RIZZO, ET E. ARIMONDO, “Four-level N-scheme crossover resonances in Rb saturation spectroscopy in magnetic fields”, *Phys. Rev. A* **92**, 063810 (2015).
- [54] J. JACKSON, *Classical electrodynamics* (Wiley, 1975).
- [55] K. HALBACH, “Design of permanent multipole magnets with oriented rare earth cobalt material”, *Nuclear Instruments and Methods* **169**, 1 (1980).
- [56] E. DANIELI, J. PERLO, B. BLÜMICH, ET F. CASANOVA, “Small Magnets for Portable NMR Spectrometers”, *Angewandte Chemie International Edition* **49**, 4133 (2010).
- [57] A. INSINGA, C. BAHL, R. BJØRK, ET A. SMITH, “Performance of Halbach magnet arrays with finite coercivity”, *Journal of Magnetism and Magnetic Materials* **407**, 369 (2016).
- [58] P. CHEINEY, O. CARRAZ, D. BARTOSZEK-BOBER, S. FAURE, F. VERMERSCH, C. M. FABRE, G. L. GATTOBIGIO, T. LAHAYE, D. GUÉRY-ODELIN, ET R. MATHEVET, “A Zeeman slower design with permanent magnets in a Halbach configuration”, *Review of Scientific Instruments* **82**, (2011).
- [59] M. SAGAWA, S. HIROSAWA, H. YAMAMOTO, S. FUJIMURA, ET Y. MATSUURA, “Nd–Fe–B Permanent Magnet Materials”, *Japanese Journal of Applied Physics* **26**, 785 (1987).

- [60] <http://www.duramag.com/neodymium-magnets-ndfeb/available-neodymium-magnet-grades/>.
- [61] M. MISAKIAN, "Equations for the Magnetic Field Produced by One or More Rectangular Loops of Wire in the Same Plane", *J. Res. Natl. Inst. Stand. Technol.* **105**, 557 (2000).
- [62] W. KNAFO, C. FAUGERAS, G. RIKKEN, J.-L. THOLENCE, F. DEBRAY, ET P. FRINGS, "Physics in High Magnetic Fields / Physique en champ magnétique intense State of the art and developments of high field magnets at the "Laboratoire National des Champs Magnétiques Intenses"", *Comptes Rendus Physique* **14**, 2 (2013).
- [63] C. S. HWANG, S. YEH, P. K. TENG, ET T. M. UEN, "A highly automatic measurement system for three orthogonal magnetic moments of a permanent magnet block", *Review of Scientific Instruments* **67**, (1996).
- [64] W. HU, J. XIE, H. W. CHAU, ET B. C. SI, "Evaluation of parameter uncertainties in nonlinear regression using Microsoft Excel Spreadsheet", *Environmental Systems Research* **4**, 1 (2015).
- [65] G. HAKHUMYAN, C. LEROY, R. MIRZOYAN, Y. PASHAYAN-LEROY, ET D. SARKISYAN, "Study of "forbidden" atomic transitions on D2 line using Rb nano-cell placed in external magnetic field", *The European Physical Journal D* **66**, 1 (2012).
- [66] A. SARGSYAN, A. TONROYAN, G. HAKHUMYAN, A. PAPOYAN, E. MARIOTTI, ET D. SARKISYAN, "Giant modification of atomic transition probabilities induced by a magnetic field: forbidden transitions become predominant", *Laser Physics Letters* **11**, 055701 (2014).
- [67] L. V. BOCKSTAL, G. HEREMANS, ET F. HERLACH, "Coils with fibre composite reinforcement for pulsed magnetic fields in the 50-70 T range", *Measurement Science and Technology* **2**, 1159 (1991).
- [68] P. FRINGS, H. WITTE, H. JONES, J. BEARD, ET T. HERMANNSDOERFER, "Rapid Cooling Methods for Pulsed Magnets", *IEEE Transactions on Applied Superconductivity* **18**, 612 (2008).

- [69] R. MIRZOYAN, A. SARGSYAN, D. SARKISYAN, A. WOJCIECHOWSKI, A. STABRAWA, ET W. GAWLIK, “EIT resonance features in strong magnetic fields in rubidium atomic columns with length varying by 4 orders”, *Optics and Spectroscopy* **120**, 864 (2016).
- [70] J. J. MCFERRAN, “An inverted crossover resonance aiding laser cooling of ^{171}Yb ”, *J. Opt. Soc. Am. B* **33**, 1278 (2016).